PHOTOPHYSICS OF FLUORESCENT SILVER NANOCLUSTERS

A Dissertation
Presented to
The Academic Faculty

By

Sandeep A. Patel

In Partial Fulfillment
Of the Requirements for the Degree
Doctor of Philosophy in the
School of Chemistry and Biochemistry

Georgia Institute of Technology

May 2009

PHOTOPHYSICS OF ENCAPSULATED SILVER CLUSTERS

Approved by:

Professor Robert M. Dickson,
Advisor
School of Chemistry and
Biochemistry
Georgia Institute of Technology

Professor Jennifer Curtis
School of Physics
Georgia Institute of Technology

Professor Christine Payne
School of Chemistry and
Biochemistry
Georgia Institute of Technology

Professor Ken Brown
School of Chemistry and
Biochemistry, School of
Computational Science and
Engineering
Georgia Institute of Technology

Professor Joseph W. Perry
School of Chemistry and
Biochemistry
Georgia Institute of Technology

Date Approved: January, 23rd, 2009

ACKNOWLEDGEMENTS

If I have seen a little further it is by standing on the shoulders of Giants

Sir Issac Newton, 1676

This work is a culmination of years of toil, frustration, despair, and heartbreak. Graduate school, however, also had its bad days. In the pursuit of a Ph.D., I learned that the moment of abject failure can be precisely the moment when success blossoms. I have had the pleasure of working with a number of extraordinary individuals who have helped to guide me through the meandering path I have pursued. I would like to thank my advisor, Prof. Robert Dickson, for the great opportunity and freedom he has given me to develop my scientific prowess. Also I would like to thank the past and present members of my research group, Lynn Capadona, Tae-Hee Lee, Jie Zheng, Jose Gonzalez, Tom Vosch, Dulal Senapati, Chris Richards, Rusty Nicovich, Junhua Yu, Jung-Cheng Hsiang, Soonkyo Jung, Sungmoon Choi, and Wonsang Goh, for the competitive environment they helped create, challenging me to be a better scientist.

Additionally, I would like to thank my friends and coworkers, including Chad Hladik, Jake Leech, Megan Houston, Angela Fritz, Susan Odom, Alex Miller, and Michal Malicki, for helping to keep me sane and grounded for all those years. Finally, I want to thank my family, including my aunt Smita, my uncle Mike, and my parents Ajit and Rasila Patel for all the support, understanding, and opportunities they have given me throughout my life and burgeoning career.

TABLE OF CONTENTS

LIST OF TABLES

LIST OF FIGURES

LIST OF SYMBOLS AND ABBREVIATIONS

ADC	amplitude-to-digital converter
APD	avalanche photodiode
β	first hyperpolarizability
c	speed of light ($2.99 \times 10^{8} ms^{-1}$)
D	diffusion constant
DE	dendrimer-encapsulated
ε	molar extinction coefficient
f	oscillator strength
Δf	solvent polarizability
ϕ_{FL}	fluorescence quantum yield
FLIM	fluorescence lifetime imaging
Γ_{rep}	pulse repetition rate
γ	second hyperpolarizability
h	Planck's constant
HOMO	highest-occupied molecular orbital
HRS	hyper-Rayleigh scattering
k_B	Boltzmann constant
LUMO	lowest-unoccupied molecular orbital
μ	micro- (10^{-6})
μ_{mn}	transition dipole moment
n	nano- (10^{-9})
n	refractive index
OD	optical density
OE	oligonucleotide-encapsulated
OPA	one-photon absorption
PMT	photomultiplier tube
PICT	photoinduced charge transfer
R_h	hydrodynamic radius
σ	absorption cross section (cm^2)
σ^{TPA}	TPA cross section ($cm^4 sphoton^{-1}$)
SHG	second harmonic generation
TAC	time-to-amplitude converter
TCSPC	time-correlated single photon counting
TPA (E)	two-photon absorption (excitation)

SUMMARY

The size transition from bulk silver metals to nanoparticles and eventually to single atoms passes through the relatively unexplored, yet intriguing nanocluster size regime. These materials, while retaining many of the discrete energy levels of atoms, possess multiple free electrons, enabling strong, size-dependent optical transitions, including fluorescence, in the visible spectrum.

Stabilization of the clusters in aqueous solutions requires the use of encapsulating agents to both coordinate the silver ions and protect the clusters, after reduction and initial agglomeration, from further uncontrolled aggregation. Single-stranded oligonucleotides and amine dendrimers, have served this function well, and the resulting properties have been previously reported. Here we expand our investigation of these fascinating materials by exploring their notable nonlinear optical properties, including the strong two-photon absorption of oligonucleotide-encapsulated clusters and the two-photon absorption and hyper-Rayleigh scattering of dendrimer-encapsulated clusters.

Radiative lifetimes of several tens of picoseconds observed for the dendrimer-encapsulated clusters have proven useful in time-gated biological imaging. The silver cluster can be discriminated despite high fluorescent background by selectively imaging at times immediately following a given laser pulse.

In addition to the endogenous effects of the cluster, its small size of only a few atoms renders it highly susceptible to surface and environmental effects, which manifests, for example, in the observed photoinduced charge transfer between the

silver cluster and oligonucleotide. Known for its ability to stabilize surplus charges, the oligonucleotide can readily accept donated electrons from silver, resulting in a long-lived charge transfer state. This state has been shown to be highly advantageous in imaging applications, as control of this state enables better control over the time-averaged emission rate of the molecule. The mechanism of charge transfer, and the possible means by which this state can be controlled will be also be investigated in this work.

CHAPTER I
INTRODUCTION

1.1 Motivation

"The 20th century will be known as the age of physics and astronomy…the 21st century will be the century of life sciences in all their ramifications," envisioned Kenneth Shine, president of the Institute of Medicine.[1] The greater part of this past century was devoted to laying the foundations of quantum mechanics and general relativity, the consequences of which have reverberated through the whole of science and technology. The focus has now begun to shift to solving problems less fundamental in nature but substantially more complex. It is appropriate, however, that in this key transitional moment in science, the armaments of physics and chemistry are being redirected to the next frontier in biological and medical sciences.

Physics and chemistry in their infancy dealt with understanding the fundamental building blocks of nature, from subatomic particles to molecules, and in the behavior of those materials we could touch and feel. Only in the last few decades have researchers squarely focused on that forgotten gap, the nanometer scale, impelled by Richard Feynman in 1959 to discover that "there's plenty of room at the bottom."[2] The nanometer scale, the meso-scale of physics, is the size of the most fundamental mechanics of life. Nature has already developed a rich, intricate world of activity on that scale, and we've only begun to understand it, let alone compete on its home field. We're challenged not only

with understanding the complex biological world, but also to adopt that understanding to create a wealth of new materials with new functions. Our ability to do so lies on our capacity to develop precision tools for probing macro-molecular events, leaving behind the clumsy fumblings of giants' fingers that marked the birth of biochemistry and genetics.

The power of nanotechnology can best be demonstrated by perhaps its oldest use. Metal nanoparticles have since the Roman times been used as a robust, color-tunable dye in ceramics and glass. Rich colorful mosaics of purple, red, blue, and green are strewn over Roman goblets, stained glass windows from the Middle Ages, and ceramic artistry of the Egyptians. Not realizing the microscopic structures or the natural laws governing their properties, these ancient artisans could only marvel at their resulting beauty. It was not until 1857 when Michael Faraday noted the beauty of gold due to its "supposed simplicity of character" and his observation that "a mere variation in the size of its particles gave rise to a variety of resultant colors" did the scientific inquiry into the size-dependent properties of metal nanoparticles begin.[3] Half a century later Gustav Mie developed a comprehensive theoretical treatment of the gold nanoparticles,[4] correctly predicting the unusually strong size-dependent plasmon absorption bands that give rise to the beautiful array of colors still found in stained-glass windows. What began as an oft-used ancient dye, developed into the object of curious examination by physicists, has now evolved into an invaluable tool for addressing some of today's most important biological problems. Metal clusters and nanoparticles have been studied for their roles in

biologically-integrated nano-materials,[5-7] photodynamic cancer therapy agents,[8-11] and as multifunctional optical probes.[12, 13]

In this thesis I will present a small example of the evolution of fluorescent silver clusters from a curious physical system to one emerging as a powerful and efficacious imaging tool. I will navigate through the fundamental physics and nonlinear optics of these sub-nanometer clusters to their promise as biologically-compatible fluorescent probes, paralleling the achievements of the physical sciences in ushering in the age of biology.

1.2 Metal Cluster Theory

1.2.1 Electronic Structure of Silver

Silver lies in the second row of the coinage metals, with properties akin to those of copper and gold. Its electronic configuration consists of a filled 4d shell and one electron in its higher energy 5s orbital. The s electron is typically referred to as a "free" electron as a consequence of its highly delocalized nature in bulk metals. The major bulk characteristics of free-electron metals can be rationalized by the Drude model, borrowed directly from the kinetic theory of gases.[14] In this model, first proposed in 1900, the electrons are treated as an ideal gas in the volume defined by the dimensions of the metal.[15] This assumption works well because the free electrons are well-screened from the ionic lattice by the lower-lying d-shell electrons. As a result, the s electrons are heavily delocalized, whose mean free path, as in an ideal gas, is defined by the

rate of scattering collisions with one another and other entities.[16] The behavior of these electrons is crucial in determining the optical and electronic properties of a particular silver metal structure, as we shall see later.

The frequency-dependent dielectric function governs the electronic response of a material to an incident time-dependent electric field such as that found in electromagnetic radiation. It is a complex function consisting of both a real and imaginary term ($\varepsilon(\omega) = \varepsilon_1(\omega) + i\varepsilon_2(\omega)$), which describes polarization and energy dissipation, respectively. Because of the electronic delocalization of s-electrons in silver, optical responses can occur in one of two ways. First are those transitions resulting from the electrons confined to individual atoms. High energies are usually required to drive these transitions (ultraviolet range). The other observed optical responses are due to the collective oscillation of free electrons. The resonance frequency of this transition is known as the Drude bulk plasmon frequency, written as[14, 16]

$$\omega_p = \left(\frac{4\pi ne}{\varepsilon_0 m_e} \right)^{1/2} \tag{1.1}$$

in which n is the electron density, ε_0 is the vacuum permittivity, and m_e is the electron mass. The dielectric function can be expressed in terms of the plasma frequency, giving,[14]

$$\varepsilon(\omega) = 1 - \frac{\omega_p^2}{\omega^2 + i\Gamma\omega} = 1 - \frac{\omega_p^2}{\omega^2 + \Gamma^2} + i\frac{\omega_p^2\Gamma}{\omega(\omega^2 + \Gamma^2)} \tag{1.2}$$

in which Γ is the damping factor (half-width) of the resonance, and the complex dielectric is separated into its real and imaginary components. Assuming that $\omega >> \Gamma$, then this approximates to:

$$\varepsilon_1(\omega) = 1 - \frac{\omega_p^2}{\omega^2} \tag{1.3}$$

$$\varepsilon_2(\omega) = 1 - \frac{\omega_p^2}{\Gamma \omega^3} \tag{1.4}$$

So a resonance occurs when $\omega = \omega_p$, which leaves $\varepsilon_1(\omega) = 0$. Silver would be expected to have a bulk plasmon energy of 9.2 eV if only the s-electrons were taken into account. The total dielectric function, however, is a combination of the dielectric function of intraband (s-electron) and interband (d to sp) transitions. For noble metals in particular, the influence of the interband transition significantly shifts the $\varepsilon_1(\omega) = 0$ condition to 3.8 eV due to the positive d-sp susceptibility. This also illustrates the relative contributions from the s-shell intraband transitions and the interband transitions as a function of energy. At energies greater than 3.8 eV, the interband transitions dominate, while at lower energies transitions occur primarily within the conduction band.

1.2.2 Size-dependence Optical and Electronic Properties

The influence of size in the chemical, optical, and electrical properties of materials can be simply demonstrated by noting the vast difference between a solution of silver atoms and a bulk solid of the same substance. The optical properties of bulk silver are decisively influenced by its unique dielectric function.

For the single atom, however, the bulk dielectric function no longer applies, as each atom is greatly influenced by environmental effects outside the confines of the crystalline lattice. The fundamental way in which light interacts with the material depends on the elemental composition, the arrangement of those components, and surface effects. The size dependence of the dielectric function arises from surface effects, for which wavefunction boundary conditions ultimately determine the energy levels of the material. The size-effect, however, operates only across particular ranges. If one were fortunate enough to possess two bars of silver, one 5 kilograms, the other 50 kilograms, one would not notice an appreciable difference in the observable properties aside from the obvious weight difference. Electrical properties, luster, hardness, etc. would all be virtually indistinguishable. Clearly size-effects are not of great consequence on this size scale. If, on the other hand, a solution containing a suspension of 5 nanometer particles was placed next to one containing 50 nanometer particles, one would be immediately struck by two different colors. In this size regime many of the optical and electronic properties are more highly size-dependent.

From the bulk to the atom, the optical responses of single-element metals experience several size regimes, and the transitions among them are governed by the characteristic length scales of several key parameters. The first is the wavelength of light. Because of the time-dependence of the optical electric field, electrons in bulk metals experience different electric fields when excited with light. When the cluster approaches $2R \approx \lambda$, the free electrons respond coherently, experiencing the same electric field.[14] The second characteristic

length scale is the bulk electron mean free path (l_∞). This is the average distance an electron travels between memory-cancelling collisions. The collisions can occur with other electrons, phonons, or lattice defects and impurities. The value for silver is 52 nm, and when $2R \approx l_\infty$, the mean free path is effectively limited by the size of the particle, and collisions at the surface begin to dominate the optical response. So for particles with a diameter smaller than 52nm, the frequency-dependent dielectric function also becomes size-dependent. The final characteristic length scale is the de Broglie wavelength of electrons at the Fermi energy (E_F), which is the energy the lowest conduction electron possesses. When particles approach this size (for Ag, $\lambda_B = 0.55nm$), all the electronic wavefunctions are overlapped, and the system retains well-defined molecular states.[17] In this size the cluster begins to behave as a molecular system. The continuity of and the size at which the transition from molecular to collective excitations occur has not been resolved in the scientific community, but it is evident that many interesting properties are to be discovered within this size range,[18, 19] including the strongly-absorbing and highly-fluorescent silver clusters discussed in this work.[20-26]

One of the key fundamental questions in metal cluster theory is, as the size of the particle becomes smaller, at what point is the material no longer considered a metal? It is clear that a single silver atom does not have the conduction properties of its bulk counterpart, so at some point along the size axis there must be what's called a size-induced metal insulator transition (SIMIT).[14, 27, 28] Bulk metals are characterized by a continuous density of states (DOS)

through the Fermi energy.[29] The continuous DOS between the energy levels in the valence band and the conduction band allow easy electron transport, and an essentially free "sea of electrons" is formed throughout the material, giving it the character of a metal. In contrast to the band theory of condensed phase materials, in atomic and molecular theory one talks of highest occupied molecular orbital (HOMO) and lowest unoccupied molecular orbital (LUMO) energy differences.[30] The energy difference between these two levels scales as $\delta = E_F / N$. The Kubo criterion describes the energy level spacing of the different size regimes as related to conductivity by the following,[14, 29]

$$\text{Metals}: \quad \delta = E_F / N \leq k_B T \tag{1.5}$$

$$\text{Insulating particles}: \quad \delta = E_F / N > k_B T \tag{1.6}$$

$$\text{Molecules}: \quad \delta = E_F / N >> k_B T \tag{1.7}$$

in which k_B is Boltzmann's constant. Metals are therefore characterized here by the transition that occurs when the energy level spacing at the Fermi energy becomes smaller than $k_B T$, at which point electronic transition into the conduction energy levels can occur with thermal fluctuations. Another perhaps more interesting transition is one between insulating particles and molecules. Whereas insulating particles have a high DOS within the valence and conduction regions, the molecule still retains many discrete states akin to molecular orbital states. Two major consequences relevant to this work occur as a result, (1) energy levels are sufficiently spaced to allow visible energy transitions and (2) non-radiative dissipation pathways between closely-spaced energy levels are mostly eliminated.

Additionally, with surface effects dominating the optical transitions for small clusters, the electron density has been shown to extend significantly beyond the cluster core.[14] This "spill out" effect has two important consequences. First, the additional damping factor due to the surrounding dielectric becomes relevant for determining the plasmon resonance frequency. Second, resonance or near resonance to energy levels of the surrounding medium opens up new channels for electron density to remain in an extended state for longer periods of time.

1.2.3 Noble-gas-encapsulated Silver Clusters

Silver clusters approaching the size of its de Broglie wavelength, as discussed earlier, have optical properties more akin to molecules than to bulk crystals. Indeed clusters consisting of fewer than 8 atoms are found to have discrete, size-dependent absorption bands. Naked silver clusters have been prepared and studied in a variety of environments, including gas-phase and in aqueous solutions.[31-34] The clusters, typically singly-charged and ranging from 2-9 atoms in size, absorbed light throughout the visible and UV wavelengths, and in most cases led to photodissociation through atom or dimer loss.[34] It was not until clusters were prepared in rare-gas matrices that radiative relaxation was observed. Photodissociation was eliminated by the "cage-effect," in which an external matrix encapsulates and holds together a particular cluster. Solid argon, krypton and neon matrices were used to encapsulate size-selected silver clusters, which were then irradiated with light to induce emission. The discrete

absorption and fluorescence was observed at wavelengths spanning the visible and near-IR wavelengths, due primarily to s-p transitions from the free electrons. In a single atom, emission bands range from 300-320 nm, with an additional band around 370 nm.[35] For the dimer, the major peaks are pushed into the visible, ranging from 440-540 nm.[18, 36] In the trimer, the emission energies are further lowered into the red and near-IR regions.[19] In addition to rare-gas encapsulation, fluorescent silver clusters have been prepared in zeolites.[37, 38] For all the species, the absorption and emission shift significantly as a function of the matrix. For such small clusters the dielectric function is strongly influenced by environmental factors, and matrix encapsulation is therefore expected to play a significant role in determining the resonance energies of particular transitions.[39, 40] There are a variety of ways in which this influence can be manifested, including chemical bonds, matrix polarizability, and excited-state charge transfer.

1.3 Molecular Nonlinear Optics

1.3.1 Derivation and History

Non-linear optics derives its name from the fact that the processes respond nonlinearly to an optical field. Most of the effects, however, are negligible for low optical excitation intensities. The consequences of this underline the fundamental utility of non-linear optical processes, that their probability of occurrence is more sensitive to the excitation intensity. For

example, one of the major advantages of two-photon absorption in microscopy is that only species in the focus are excited, resulting in the near-elimination of background fluorescence that typically plagues one-photon imaging systems.[41-43]

The interactions of matter with optical fields can best be described by its time-dependent polarization, which is a linear function of the electric field.[44]

$$P(t) = \alpha E(t) \tag{1.8}$$

Most common optical phenomena, such as absorption and fluorescence, are governed by this relationship, where the coefficient α is called the linear susceptibility. Using the harmonic oscillator model, the oscillator can be driven linearly by a small applied force. When the applied force is increased, however, nonlinear motions can be induced which at low forces have negligible effects on the oscillator, but at high forces become an increasingly important effect. This can be seen by the power series of the polarization, described as[45]

$$P(t) = \sum_{n=1}^{n} \chi^{(n)} E^n(t) \quad = \alpha E(t) + \beta E^2(t) + \gamma E^3(t) + \ldots \tag{1.9}$$

The coefficients β and γ are known as the first and second hyperpolarizabilities, respectively. These coefficients are actually tensors of rank n+1, and are often anisotropic, resulting in anisotropic polarization in response to an applied field. The strength of the coefficients typically decrease by several orders of magnitude further down the series, so the first hyperpolarizability is negligible compared to the linear polarizability. With the advent of the ruby laser in 1960,[46] however, high excitation intensities could be easily generated and therefore made the observation of nonlinear effects attainable by laser excitation. It was not until the development of picosecond and femtosecond pulsed lasers,

for which peak intensities are orders of magnitude higher than continuous-wave lasers, did their practical use become feasible. The first major application was for second harmonic generation by nonlinear crystals, which is a second order effect that doubles the frequency of light passed through it.[47, 48] This found an immediate application in laser technology, where pulsed infrared lasers (e.g. Nd:YAG and Ti-sapphire) could be used to excite materials in the UV and visible regions.

In spite of the low polarizabilities in the higher order polarization terms, the power series makes each subsequent term a higher order function of the applied electric field, and therefore allow these phenomena to become sufficiently strong at high field strengths. For example, second harmonic generation, negligible for continuous-wave lasers, can become highly efficient in generating second harmonics for focused pulsed laser. The effects are even more pronounced when resonance conditions are met.

The empirical Miller's Rule has been found from compilation of experimental data that suggests a link between the strengths of the different polarizabilities.[49] It is given by[45, 50]

$$\Delta = \frac{\chi^{(2)}(\omega_3)}{\chi^{(1)}(\omega_3)\chi^{(1)}(\omega_1)\chi^{(1)}(\omega_2)} \tag{1.10}$$

and is almost always a constant for a wide range of materials, suggesting that materials with high linear polarizabilities have proportionately high hyperpolarizabilities. The value has been estimated roughly to be 100-120, indicating that the first hyperpolarizability is roughly two orders of magnitude smaller than the linear polarizability. This rule, though empirically derived, has

not been proven theoretically, however, it can be used to roughly predict nonlinear optical strengths based on already known linear optical strengths of materials. This approximation does not take into account specific symmetry and selection rules which may affect the final transition strengths.

1.3.2 Dipole Approximation

In the electric dipole approximation (EDA), all induced polarizations are approximated as dipoles.[51] This approximation is based on the key assumption that the electric field is constant over the charge polarization range.[52] That is, that the electric field felt by a polarizable charge is constant at any given time. This is typically valid for most polarizable materials, but begins to break down for highly-extended charge distributions, in which local-field effects begin to spatially perturb the local electric fields and cause significant multipolar distributions.

For purely centrosymmetric materials that possess inversion symmetry, all of the tensor components of the first hyperpolarizability and the other even-ordered term are zero. When the EDA is no longer valid, multipole polarizations must then be taken into account. Quadrupoles have a non-zero first hyperpolarizability for centrosymmetric materials, and hence can give rise to second-order effects despite symmetry restrictions.

1.3.3 Local Field Effects

When discussing nonlinear optical effects of materials, especially for materials smaller than the wavelength of light, the electric field that the material

experiences does not necessarily correspond with the field that is applied. Because the macroscopic field induces a polarization in every atom/molecule in the system, the overall local field is a combination of the macroscopic field and the fields induced by individual polarized elements. Molecules in solvents may experience local fields due to the induced polarization of the solvent, and depending on its local structure, have significant effects on the overall field experienced by individual molecules.

1.3.4 Two-photon Absorption

One-photon absorption (OPA) is characterized as the absorption of a single photon, and scales linearly with the excitation intensity. The excited molecule can either dissipate non-radiatively back to the ground state or by emitting a lower energy photon, the energy difference called the Stokes shift. The shift in energy is attributed to vibrational relaxation in the excited and ground-states before reaching the vibronic ground state. Emission can also occur by nonlinear excitation of the molecule, most commonly by two-photon absorption (TPA).[45] In this case, two photons are absorbed, either simultaneously or in succession, to excite the molecule, and absorption probability depends on the square of the excitation intensity. When the two photons are of the same energy and are absorbed simultaneously, it is referred to as degenerate TPA. For a molecule to be populated to a real excited state, the excitation must occur on resonance, increasing the TPA cross sections at the resonance frequencies. Resonance may also occur at the intermediate energy

level, although it is not necessary. Though the electronic and vibrational selection rules are different for one-photon and two-photon absorption, excitation often occurs to the same electronic state for both processes. According to Kasha's Rule, emission will almost always occur by relaxation from the lowest excited electronic state, because Franck-Condon overlap is greatest for electronic levels close in energy. Therefore, one-photon and two-photon excitation will typically yield identical emission spectra with identical relaxation times. The TPA cross section, in which the transition occurs from the ground state (g) to the final state (n) via the intermediate state (m), can be expressed by the following expression: [45]

$$\sigma_{ng}^{(2)}(\omega) = \frac{8(\pi\omega)^2}{(nc)^2}\left|\sum_m \frac{\mu_{nm}\mu_{mg}}{\hbar(\omega_{mg}-\omega)}\right|^2 \frac{\Gamma/2}{(\omega_{ng}-\omega_{ng})^2+(\Gamma/2)^2} \qquad (1.11)$$

In the expression, n is the refractive index, c is the speed of light, μ is the transition dipole moment between the respective states with frequency ω. It is assumed here that the final state n has a Lorentzian lineshape, and Γ is the decay rate of the final state. The transition dipole moment between both transitions contribute to the overall cross section, therefore for cases in which a double resonance occurs the cross section may show an even larger value than for the singly resonant case. The cross section is often reported in the Goppert-Mayer unit (GM), which is equal to $10^{-50} cm^4 sphoton^{-1} molecule^{-1}$.

Many standard commercial dyes such as the rhodamine and cyanine dyes have significant TPA cross sections.[53, 54] But because nonlinear absorption cross sections are inherently smaller than linear ones, many dyes have been

specifically designed for high cross sections, including large push-pull organic molecules,[55-59] conjugated polymers,[60-63] and semiconductor quantum dots.[64-67]

1.3.5 Hyper-Rayleigh Scattering

While SHG is a coherent, phase-matched second order nonlinear effect, hyper-Rayleigh scattering (HRS) is an incoherent scattering process, and may be thought of more as the second order Rayleigh scattering. HRS can occur for individual molecules in solution, and lacks the phase-matching requirement necessary for bulk crystals.[68-72] HRS, like SHG, is a second-order process that depends on both the first hyperpolarizability tensor and the square of the excitation intensity. Incident photons are scattered, and a resulting photon at twice the energy is simultaneously scattered by the molecule. HRS has long been a standard method by which to measure the hyperpolarizability of a molecule due to the simple relationship between scattering strength and hyperpolarizability.[73] But because it's a tensor value (rank 3), there are 27 elements to evaluate. Due to symmetry conditions of the tensor, there are only 10 independent values, and this can be further reduced depending on the particular symmetry of the scatterer. For instance, many organic molecules designed for HRS are long, π-conjuated systems, for which the primary component of the hyperpolarizability tensor is the $\chi^{(2)}_{zzz}$ element, because polarization occurs primarily along one direction of the molecule.

1.3 .6 Non-linear Optics of Silver Nanoparticles

Noble metal nanoparticles have been demonstrated to have a particularly high second-order scattering cross section, consistent with the high linear polarizability of its collective electrons. The HRS of silver nanoparticles between 10 and 40 nm in diameter were studied by Hupp and coworkers, and they reported resonant hyperpolarizabilities as high as 1400 $x10^{-30}$ esu /atom at 820nm.[74-77] For comparison, organic chromophores were reported to have values of about 50-100 $x10^{-30}$ esu /atom.[77] The resonance is correlated with the plasmon resonance for these particles, occurring at around 420nm.

To explain the enormous scattering cross sections of these particles, which approximately are spherical and therefore nearly centrosymmetric, the validity of the dipole approximation for the metallic particles has been called into question by Heinz and coworkers. In their theoretical treatment of second-order scattering by metal nanoparticles, they established that there are multiple mechanisms by which scattering can occur even for ideally spherical particles.[51, 78] Firstly, because the dipole approximation is no longer valid due to the presence of both volume and surface plasmon resonances, scattering can occur by induction of a quadrupole polarization. Quadrupole polarizations, according to symmetry rules, can be induced by both a resonance due to a dipole interaction and a quadrupole interaction between incident photons and the polarizable metal electrons.[51, 78, 79] Therefore it is predicted that two resonances, closely spaced, will occur, due to the different resonance conditions of the processes. Each resonance will produce a different scattering pattern, formed by considering the

scattering probabilities as a function of spatial angle relative to the molecular axis. Additionally, the use of circularly polarized excitation will produce a purely quadrupolar scattering pattern by selection rules, while linearly polarized light can excite both modes.[51]

This has been experimentally verified by both Hupp and coworkers and Brevet and coworkers, who have both reported excitation spectra of HRS from silver nanoparticles to contain two peaks, at 780 and 820nm, resulting from dipolar and quadrupolar contributions, respectively.[74, 80] In addition to the wavelength dependence, a size-dependence was reported for the relative strength of these two transitions. It was found that for larger particles (80nm diameter), the scattering signal was contributed almost purely by the quadrupolar transition.[81] As the particle size became smaller, down to 10nm, the relative contribution of the dipole transition became significantly larger. HRS intensity as a function of incident beam polarization angle was used to determine the scattering pattern of these particles, and demonstrated a clearly 4-lobed polar plot, indicative of quadrupolar contributions for the 80nm particles.

Though the overall scattering strength decreases with particle size in the several to tens of nanometer size range, quantum size effects were predicted by Lue and coworkers to take place out of resonance for particles smaller or equal to a few nanometers, wherein the total enhancement of the HRS increases for these small particles.[82] Resonance conditions, however, of the plasmon-sustaining nanoparticles, result in the much stronger observed signal for large particles.

1.4 Nucleotide Charges

1.4.1 Charge transport in DNA

Single-stranded oligonucleotides were used to encapsulate many of the fluorescent silver clusters discussed in this work.[22, 83, 84] DNA molecules provide the water-soluble, bio-compatible, and strongly agrophillic functionality ideally suited for use as bio-labels. Strong matrix effects on the overall optical properties of protected silver clusters in solution necessitate the investigation of how that effect may be manifested.

DNA has evolved to perform a variety of functions in organisms. First and foremost it is a self-replicating molecule carrying the genetic information governing the majority of known biological functions. The information is stored in the particular order of four nucleotide bases, cytosine, thymine, guanine, and adenine, which are covalently attached along a phosphodiester backbone. As stored in the body, it exists in a duplex, with each strand bound to one other by hydrogen bonds formed specifically in Watson-Crick basepairing (adenine-thymine; guanine-cytosine).[85] The fidelity of the stored genetic information is crucial for optimally performance and genetic heredity, both in cell and life reproduction. Therefore there are a number of unique properties of DNA that are believed to play critical roles in safeguarding the polynucleotide structure.

Among them are the abilities of duplex DNA to accept and transport charge along its chain, which is believed to be an integral part of the DNA repair

mechanism for radiation damage and mismatched base-pairs.[86, 87] Charge transport is believed to occur by a hopping mechanism along the nucleotide bases. Therefore the individual bases are biologically designed to stabilize surplus charges, and this discovery has prompted the spectroscopic investigation of anionic nucleotides.

1.4.2 Anionic Nucleotides

Photoelectron spectroscopy (PES) is a spectroscopic technique in which a typically gas-phase anion is irradiated with a pulsed laser with energy $\hbar\omega$, causing the photoejection of an electron, whose kinetic energy (E_k) is then measured. The electron affinity (E_a) is then calculated by Einstein's relation, where $E_a = \hbar\omega - E_k$.

The electron affinities of individual nucleotides have been extensively studied, but we shall focus particularly on cytosine here, because (1) as it shall be later shown, it is believed that silver selectively interacts with cytosine and (2) the photoelectron spectra of the relevant bases (thymine, cytosine, and adenine) are very similar.

In the gas phase, Bowen and coworkers[88, 89] reported a broad absorption spectrum peaking at 0.87 eV for deoxycytidine, while theoretical values reported by Schaefer and coworkers predict a 0.72 eV VDE. Depending on Franck-Condon vibrational overlap between the neutral and anionic states, this value may or may not exactly correspond to the electron affinity. Schlag and coworkers,[90] on the other hand, reported the PES of cytosine, which lacks the

deoxy-sugar found in DNA, to feature sharp peaks at low binding energies of 85 meV and 230 meV. The discrepancy between the two results is attributed to different anion binding modes.[91, 92] The broad peak at higher binding energies corresponds to a valence-bound anion, in which the surplus electron resides in the π* LUMO state of the nucleoside. The sharp peak of the nucleotide, however, is due to a dipole-bound state. The surplus electron in this case resides only loosely in the nucleotide, acting more as a spectator than a charge interacting with the molecular core. The electron therefore requires little energy to be photodetached, resulting in the low energy PES peak. Upon the addition of several water molecules to the nucleotide, however, the spectrum broadens significantly and peaks between 0.9 and 1.1 eV, blue-shifting with the addition of more water molecules. Surrounded by polar water molecules, the nucleotide is better able to stabilize the anion, and is therefore bound more strongly than without the water. This is evident by both the higher binding energy and the broader spectra, indicative of a valence-bound anion state.

1.4.3 Photoinduced Charge Injection

Whereas the gas-phase studies of bare nucleotides injected charge by collisions with electron beams in vacuum, more practical applications require photochemical charge injection. To this end a series of studies were published in which photosensitive charge donors were covalently attached to nucleotide bases or to oligonucleotides and studied in solution. Pyrene-based dyes were

the most commonly-used donors, because its absorption in the UV created a sufficiently high driving force for electron transfer upon excitation.[93]

Pump-probe transient absorption spectra were measured for these synthetically-prepared adducts, in hopes to measure the absorption spectra of a transiently-occurring nucleotide anion. Fiebig and coworkers did a study with uracil as the acceptor nucleotide, and found a broad absorption band between 600 and 670 nm, assigned to the uracil anion. Charge injection occurred within 35 ps of excitation, but the back electron transfer occurred on too long a time scale to be reported (>100 ps). The charge-transfer was highly solvent dependent, with no observable transfer occurring in an acetonitrile solvent (due to the absence of hydrogen-bonding, which was proposed to be a key element in the charge-transfer mechanism), and a shift in the transient absorption spectra occurs in the presence of methanol. Polynucleotides labeled with electron donors can also facilitate charge transfer. Fox and coworkers reported a study of an end-labeled polyadenosine sequence, in which they found a length-dependent back electron transfer decay time, suggesting that longer strands are capable of delocalizing and further stabilizing the anion state. Additionally, strands containing a guanine base (a known quencher) on the other end have a faster decay time, showing that charge is delocalized across the length of the strand.

1.4.4 Interactions between DNA Bases and Silver Ions

Nucleic acids, in monomeric or polymeric forms, as well as single-stranded and double-stranded, can coordinate many types of metal cations.

DNA nucleotides contain two major sites for metal coordination. The negatively-charged phosphate groups that make up the backbone provide an electrostatically favorable site for divalent metal coordination, and Mg^{2+} has been shown to be critical for stabilizing tRNA tertiary structure, coordinating DNA-enzyme interactions, and stabilizing helical DNA structure. The bases also contain several coordinating sites for metals, especially the hydrogen-bonding sites in Watson-Crick base pairing. It has been shown that the hard metals (Mg, Na, Sm) interact almost exclusively with the phosphate groups, while softer metals (Pt, Hg, Co, Mn) interact primarily with the bases.[94] Silver, classified as a "soft" metal, has been shown to preferentially bind nucleotide bases over the phosphate group. Investigations into the silver binding of duplex nucleic acids have shown that silver ions disrupt guanosine-cytidine hydrogen bonding, and can be used to separate strands of sufficient G-C content. Other studies have revealed that silver competes with guanosine to bind to the N3 and O2 sites of cytosine.[95] A structural investigation into the specific binding interactions between silver nitrate and 1-methylcytosine by Kistenmacher and coworkers[95, 96] demonstrated that polymeric stacks are formed, in which two silver ions each coordinate with the O2 of one base while binding to the N3 of another. Each of these then are bound to the O2 of another base along the polymeric stack. The dimerization of cytosine in the presence of silver will be important in considering the interactions of silver ions with 12mer ssDNA.

1.5 Multiphoton Microscopy for Biological Imaging

From staining fixed cells and tissues to single-molecule labeling of proteins and DNA *in vitro*, fluorescence imaging has realized a range of functions in biophysical studies. The opacity of tissues to visible radiation hinders many of the deep-tissue imaging applications being currently explored, while cell auto-fluorescence significantly increases the background in sensitive cell imaging studies. Tissues are considered most transparent in the window between 700 and 1100nm, but because bio-compatible dyes absorbing in that region are scarce and emission from OPE occurs at lower energies anyway, dyes having large TPA cross sections in the optically transparent window are highly desirable to serve in many of these applications. Background fluorescence is limited because strong two-photon absorbers in the near-IR are scarce among biological molecules, and the quadratic intensity dependence virtually eliminates out-focus background from either the probe dye or other species present.

TPE intrinsically achieves greater three-dimensional resolution than OPE, without the use of the emission pinhole that standard confocal microscopy requires. The collection efficiency of confocal setups is limited due to the pinhole, which, along with rejecting out-of-focus emission, also rejects scattered light originating from the focus. The diffraction limit for TPE, however, is larger due to the longer wavelength excitation used, but the small decrease in x-y resolution is outweighed by the increased axial resolution.

The high intensities required to significantly excite the two-photon dyes, however, can be problematic. There are essentially two issues at play with photoexcitation. The first is photo-damage to cells and tissue. OPE in the UV and visible regions is known to interfere with many biological processes such as cell reproduction, due to the high density of intrinsic absorbers in that region. Many mechanisms including biomolecule cleavage, radical production, and reactive triplet states have been linked to cell damage. TPE avoids many of these issues because cells have significantly higher damage thresholds in the near-IR region. The second issue is direct photodamage of the chromophores. While in OPE photobleaching of dyes can occur both in and out of focus, TPE largely eliminates out of focus photobleaching. In the focus, however, it's been shown that photobleaching is in fact accelerated. Photobleaching quantum yields are often much larger for high-intensity pulsed excitation. This is in part due to greater access to higher energy states by two or three photon excitation, which can lead to more irreversible photodegradation pathways. It is therefore necessary to design photostable dyes possessing large two-photon absorption cross sections. The large cross sections would allow the use of lower peak intensities which might otherwise damage the biological environment.

There are numerous concerns about the potential toxicity of silver compounds, particularly salts and free ions. Silver nitrate has long been used as a medical antibacterial in newborns, and has been associated with lethal ion uptake inhibition in rainbow trout.[97, 98] Its known toxic effects, however, have been primarily limited to bacteria, fungi, and algae, with limited effect in larger

animals.[99] It is not considered a cumulative toxin in humans as mercury is, and is expunged through excretory systems. Silver nitrate is already used in many medical applications including burn wound therapy,[100, 101] so although its effect on bacteria may be potentially problematic for *in vivo* testing, clinical imaging in mammals and humans would not appear to cause long-term damage.[102]

Single molecule fluorescence spectroscopy is also an increasingly useful technique for studying photophysical dynamics of fluorophores, as well as using the probes to study the many complex biological processes drowned out in bulk systems. To meet the needs for stable, highly-fluorescent probes, new dyes and techniques designed to exploit the necessities of single molecule imaging are being continually developed. Though single molecule detection is easily achieved for a number of commercially-available fluorophores, useful studies have thus far been limited to linear excitation. Multiphoton absorption requires large peak intensity values such as those from mode-locked femtosecond pulses, and the use of them significantly increases the probability for higher order excitation. Many irreversible photodegradation pathways are accessible from these excited states, resulting in a higher photobleaching quantum yield and thus an impractically short survival time for organic dyes. Additionally, the use of pulsed excitation introduces a duty cycle, creating a photon emission upper limit, opposed to linear excitation where CW excitation may be used to increase count rates.

1.6 Core Questions Addressed

Among the many intriguing questions invoked by metal clusters properties and their complex interactions with particular environments, none is perhaps more fundamental than its size-dependence. It is because of its size that silver clusters posses the strong, yet tunable, fluorescent electronic transitions observed in past reports and in this work. Yet size determination has been the most elusive of all the measurements attempted to better understand this class of materials. So instead, I will discuss how the specific size regime of the encapsulated silver clusters affects their optical properties. Throughout this work the distinction between silver nanoparticles and clusters will be repeatedly made, as its importance is paramount for what optical properties it features and its eventual bio-labeling efficacy. I will attempt to extend the arguments made for the origin of the linear optical properties to help explain the existence of their strong *nonlinear* optical properties. Strong two-photon absorption relies on many of the same parameters as strong one-photon absorption, for instance. Hyper-Rayleigh scattering strengths can then be partially explained by the resonances resulting in strong two-photon absorption.

Size can also play a key role in the excited-state dynamics of silver clusters. The charge-transfer state in silver cluster/DNA complexes relies heavily on the small size of these clusters, which enable the strong coupling of the two systems as well as substantial wavefunction overlap. We will explore the dynamics of these systems, facilitated in part by the strong absorption cross sections of the system.

Finally, there are a number of important issues related to their utility as biologically useful fluorescent-labels. Absorption, fluorescent quantum yield, emission energies, photostability, chemical stability, multiphoton absorption, and fluorescent lifetime are all properties highly characterized in fluorophores (bulk and single molecule), as they have direct relevance in their performance. These properties will be addressed as they relate to bio-labeling.

CHAPTER II
EXPERIMENTAL SCHEMES AND SYNTHESIS

2.1 Synthesis

2.1.1 Oligonucleotide-encapsulated Silver Clusters

Oligonucleotide-encapsulated silver cluster solutions were synthesized, using silver nitrate (Sigma-Aldrich, 99.9999%) and sodium borohydride (Aldrich, 98%) without further purification, into various oligonucleotide matrices (Integrated DNA Technologies, desalted by the manufacturer). Cluster emission wavelengths were controlled by using specific DNA oligonucleotide sequences identified by microarray studies.[22] Oligonucleotides, received as a solid, were dissolved in deionized water. For the synthesis, a 50 μM oligonucleotide solution was allowed to mix at room temperature with $AgNO_3$ in a 1 Ag per 2 bases ratio (in total volumes ranging from 1 mL to 15 mL). After 10 minutes, the solution was reduced with aqueous $NaBH_4$ and briefly agitated for 1 minute. The solution at this point became colored (yellow, red, or green, depending on the species being synthesized), indicating the formation of silver clusters. After several hours the solution stabilized and fluorescence at the desired wavelengths became observable. All reactions were performed in deionized water. The species discussed in this work and their corresponding oligonucleotide sequences are shown in Table 2.1.

For bulk multiphoton and transient absorption experiments, more concentrated samples of the solutions described above were necessary. The synthesis of clusters using a DNA concentration above 50μM (using the same

***Table 2.1*. DNA Sequences used for Silver Cluster Synthesis**

λ_{abs}(nm)	λ_{em}(nm)	Ag:BH4:Base	Scaffold Sequence
575	615		5' CGC GCC CCC CCC CCC CCG CG 3'
540	620	6:6:1	5' CCT CCT TCC TCC 3'
575	635		5' ATA TCC CCC CCC ATA T 3'
560	640	6:6:1	5' CCC CCC CCC CCC 3'
594	660	6:6:1	5' CCC ATA TTC CCC 3'
620	680	6:6:1	5' CCC TAT AAC CCC 3'
633	710	6:3:1	5' CCC TAA CTC CCC 3'

615 and 635 emitters synthesized by Sungmoon Choi
620, 640, 660, and 680 emitters synthesized by Chris Richards
710 emitter synthesized by Junhua Yu

ratios of the other reagents) significantly dropped off in creation efficiency. Therefore the concentration of fluorescent clusters was done after initial formation, by vacuum-pumping (DNA Speedvac DNA110) to reduce the solution volume, then adding 1:10 of the original concentration of $NaBH_4$ to again reduce the emissive species which had oxidized during the concentration process. The resulting concentration was tuned by controlling the volume reduction during the vacuum step.

In the concentration procedure, there are a few observations of note to discuss. Firstly, it is clear that the number of fluorescent and absorbing silver clusters does not remain constant during volume reduction. That is, if the solution is concentrated by a factor of 10, neither the absorption peak nor the fluorescence rate goes up by that factor. In fact, the fluorescence typically *decreases* during the process. It is therefore reasonable to conclude that during the process a significant fraction of the species are oxidized. Adding the reducing agent $NaBH_4$, however, allows not only the recovery of the absorption/fluorescence but a further increase in both quantities. The second reduction step then is actually increasing the creation efficiency of cluster formation, defined as the ratio of fluorescent species to the number of oligonucleotide molecules. Previously efficiencies on the order of 0.5-2% were measured; with the second reduction that number increases to approximately 3-6%. The increased concentration is shown in the absorption spectrum in Figure 2.1. The absorption features corresponding to the fluorescence excitation spectrum (e.g. the peak at 633 nm for the Ag710 species) appear to be

independent of the multiple absorption features between 400 and 500 nm. The ratio of those peaks are almost never constant, and only the absorption at 633 nm is correlated in intensity with the fluorescence intensity of the solution. Additionally, the features at 400-500 nm do not disappear with centrifugation, at forces exceeding those used to spin-out 5-10 nm particles. It is therefore unlikely that they are a result of a nanoparticle plasmon absorption band. It is suspected that they are the absorption bands of distinct, non-fluorescent silver clusters that are in a similar size range as the fluorescent species.

Additionally, as there are a number of different species that can be made, all with varying absorption and emission energies, is it pertinent to discuss the issue of chemical and spectral purity of synthesis. Using C_{12} as the encapsulating strand, a mix of species is formed in the same solution. For more optimized sequences, however, the selective synthesis can be controlled to produce predominately a specifically emitting species, on the order of 10:1 spectral purity, as measured by an emission scan covering excitation from

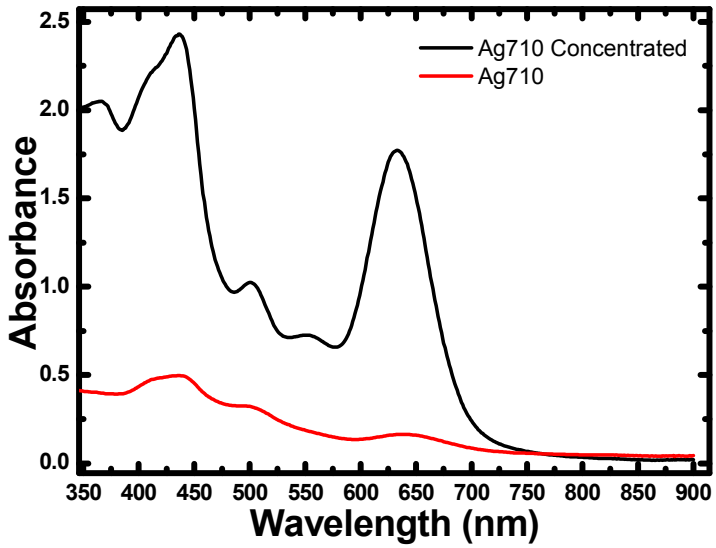

Figure 2.1 Absorption spectrum of Ag710 species as originally made (red) and upon concentration (black). The concentrated sample is shown after adding 1:10 BH_4:Ag, at which the point the creation efficiency increased from 0.72% to 2.7%, in reference to the concentration of oligonucleotides in solution. This behavior is typical of many of the AgDNA species upon concentration.

300nm to 700nm. Upon concentration and second reduction, however, not only does the creation efficiency increase but the spectral purity has been shown to increase to approximately 50:1 for the Ag660, Ag680, and Ag710 species.

In order to properly understand the synthetic procedures used, the issue of kinetic trapping versus thermodynamic stability should be discussed. An aqueous solution of silver cations is relatively stable in a hydrated state and will stay in solution. Once the ions are reduced to their neutral states, however, the crystalline solid becomes the most thermodynamically-stable state. The crystal, however, is not immediately formed. In fact the kinetics of formation are dramatically affected by the particular environment of the solution. The theory and synthesis of colloidal particle solutions have extensively explored this process for the nucleation and condensation of growing particles. The introduction of an encapsulating agent in the solution, particularly ones that can bind to silver cations, provides the kinetic trap necessary to prevent further aggregation. Though the system would most favorably evolve towards larger particles, the encapsulating agent introduces a large energetic barrier to that path, ideally resulting in stable clusters of small size. It is critical, therefore, that the encapsulating agent have sufficient interaction with both silver cations and neutral clusters to both facilitate the formation and stabilize the species after reduction. The structure of the cytidine monophosphate monomer is shown in Figure 2.2a.

2.1.2 Dendrimer-encapsulated Silver Clusters

The synthesis of dendrimer-encapsulated silver clusters loosely resembles that of oligonucleotide-encapsulated clusters. In both cases the cluster is reduced from a pre-formed unreduced species to either a partially or fully reduced fluorescent cluster, but chemical methods have thus far not worked well for the dendrimer systems, most probably due to a looser encapsulation and proclivity to aggregate into larger particles. So, for dendrimer systems a photoreduction method, wherein the clusters have been deposited onto a glass surface (coverslip) provided more control over the level of reduction/aggregation necessary to form small, fluorescent clusters. As a result, these species can only be created on a surface in low yields, thus rendering the system unavailable for bulk experiments. They are, however, extremely bright, with some unusual optical properties, warranting their study and understanding. It is therefore both feasible and necessary for single molecule detection methods to be employed in their characterization.

Dendrimer-encapsulated silver clusters were prepared by mixing equal volumes (30-100μl) of a 10^{-4} M $AgNO_3$ solution and a $2x10^{-5}$ aqueous dendrimer solution onto a clean coverslip. The solution was let dry for several hours in the absence of light, and covered to prevent impurities from collecting on the glass surface. The dry-cast sample was then irradiated with blue light (either blue bandpass Hg-lamp excitation or 476nm argon ion laser excitation), with moderate intensities ranging from 10 W/cm^2 to 40 W/cm^2 for approximately 20 seconds.

A variety of dendrimers were found to effectively encapsulate the fluorescent clusters. Although structurally different, every dendrimer used

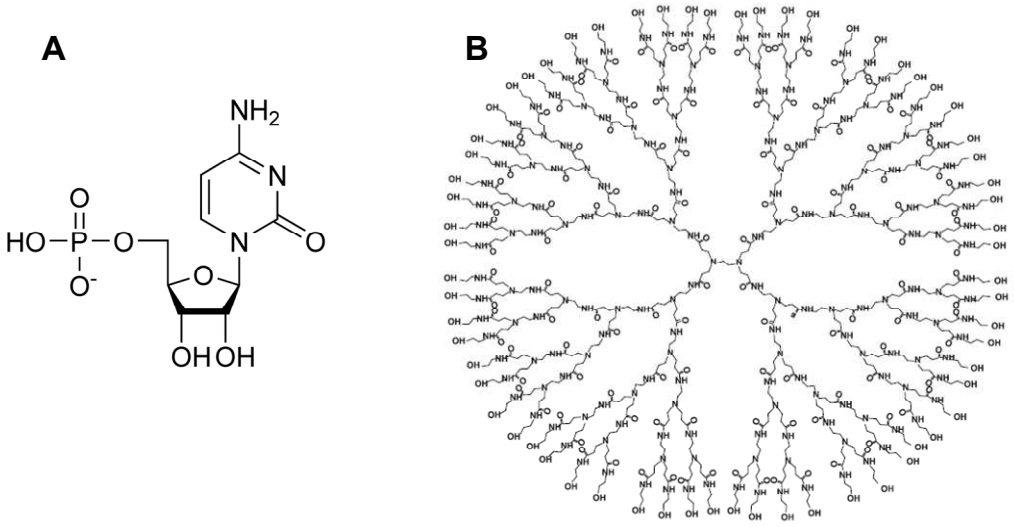

Figure 2.2 (A) Structure of cytidine monophosphate, the primary monomer component of the ss-DNA strand used to encapsulate silver clusters. Other bases (adenine, thymine) were used in specific sequences of 12-20mer strands. (B) Structure of polyaminoamine-OH (generation 4), also used as an encapsulating agent.

resulted in indistinguishable fluorescence properties upon photoactivation. The majority of the reported experiments used the generation 4 polyamidoamine (PAMAM) with OH termination dendrimers, whose structure is shown in Figure 2.2b.

2.2 Bulk Optical Characterization

Absorption scans in the UV-visible-NIR region were performed using a Shimadzu UV-2401 PC spectrophotometer, while for fluorescence measurements a Photon Technologies International fluorometer was used. Cuvette-based fluorescence lifetime measurements were performed by an Edinburgh Instruments Lifespec-ps system, using a Hamamatsu multi-channel plate PMT, cooled to -30°C. Pulsed excitation was provided by a Picoquant interchangeable diode laser system controlled by the PDL 800-B unit. The temporal pulse width of the diode laser was measured at 65ps, as measured by the Rayleigh scattering response of the laser with an MCP-PMT.

2.3 Fluorescence Microscopy

Fluorescence microscopy is a general term inclusive of a variety of photophysical techniques and imaging tools, and can greatly vary in both the experimental setup and scientific objective. It includes the many methods by which images of synthetic materials and biological systems can be obtained, but

also the methods by which photophysical parameters such as absorption cross sections, emission/excitation spectra, and molecular dynamics are measured.

All experiments performed using the fluorescence microscope (Olympus; either IX-70 or IX-71) follow the same general setup, with excitation source, dichroic mirror, objective, and photon detection system all interchanged among various experiments. In all experiments the same objective was used both to excite the sample and collect the resulting emission.

All samples used in microscope experiments were prepared on 22.5x22.5 mm glass cover slips with a 0.15 ±0.02 mm thickness (Fisher, Fisherfinest). Before use they were cleaned by placing them in a cover slip holder and immersed in 0.1M NaOH for 3 hrs, followed by sonication for 30 minutes. The cover slips were then washed with deionized water 3 times and immersed in the water while sonicating for 30 minutes. After washing with acetone 3 times, they were sonicated briefly in acetone, and then immediately dried with argon gas. Finally, they were placed in a vacuum oven (30 in. Hg, no heat) for at least 12 hours. The schematic for two-photon microscopy is shown in Figure 2.3.

2.4 Dark-field Microscopy

To image the Rayleigh scattering of particles, a technique known as dark field microscopy was used. It relies on using a high NA condenser (Olympus, oil-immersion 1.4 NA) to direct light at high angles to the sample. A dark field patch stop is contained within the condenser to block out any direct light, so that only

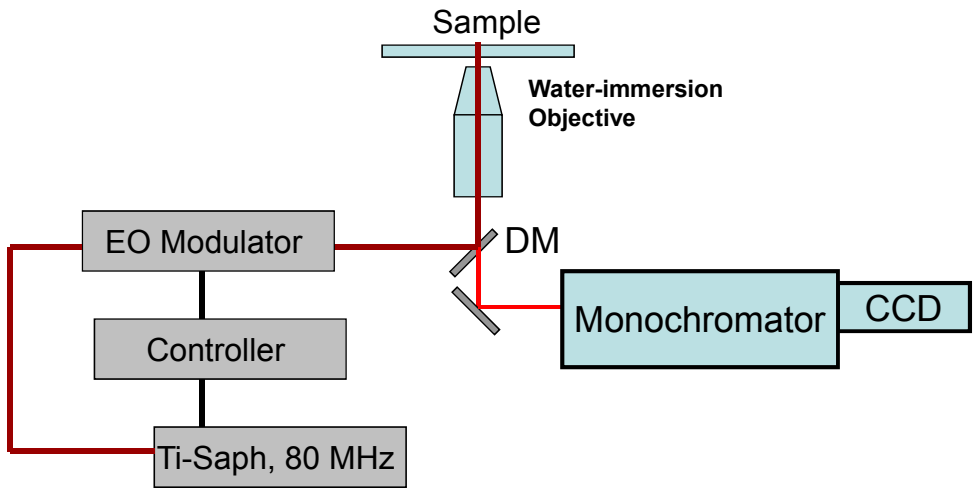

Figure 2.3 Schematic experimental setup for two-photon excited fluorescence experiments. The EO modulator (ConOptics) was used to frequency-divide the optical pulse train of the Ti-sapphire (Mira, Coherent). The laser was reflected by a short-pass dichroic filter into the water-immersion objective (1.2 NA, 40x Uplan Apo, Olympus) and the emission filtered through a short-pass emission filter before being spectrally dispersed through the monochromator and onto the CCD device (Andor, iXon).

the high angle components pass through. If the sample does not scatter the light, then it will simply pass through the sample and out of the opposite collection objective (Olympus, oil-immersion 1.35 NA with iris). If however, there are scatterers within the sample then that light will be scattered into the objective and imaged with a CCD camera (Andor, iXon). The schematic is shown in Figure 2.4.

2.5 Time-correlated Single Photon Counting

Time-correlated single photon counting (TCSPC) is a photon counting method used in many of the time-dependent and correlation measurements described here. The basic principle underlying it is the time-stamping of the arrival times of photons to a given photon detector. The detector converts the photon signal into an electrical signal, which is then counted by a single photon counting board (Picoquant; Time Harp 100, or Becker & Hickl; SPC-630), shown in Figure 2.6. For fluorescent lifetime measurements a few nanoseconds or faster, a PMT with faster time resolution (Hamamatsu; H7422P-40(50), or Hamamatsu MCP-PMT) was used, while for longer time-scale correlations the more sensitive APD proved more prudent (Perkin Elmer, or EG&G). The counting boards have two inputs, one for signaling the beginning of an excitation cycle (labeled “sync” or “stop”) and one for the signal photon (labeled “cfd” or “start”). For all electrical pulses to be properly received by the board, they must have negative polarity and fall within a certain peak voltage range (between 20-

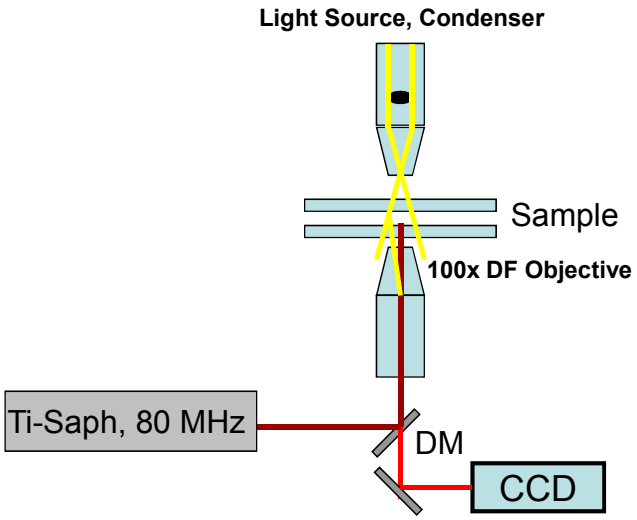

Figure 2.4 Schematic experimental setup for dark-field microscopy. Light originating from the oil-immersion condenser is focused through the sample and scattered into the oil-immersion objective (1.35 NA, 100x, Olympus) only when scatterers are present in the sample. The laser was used simultaneously to correlate scatterers with emissive particles.

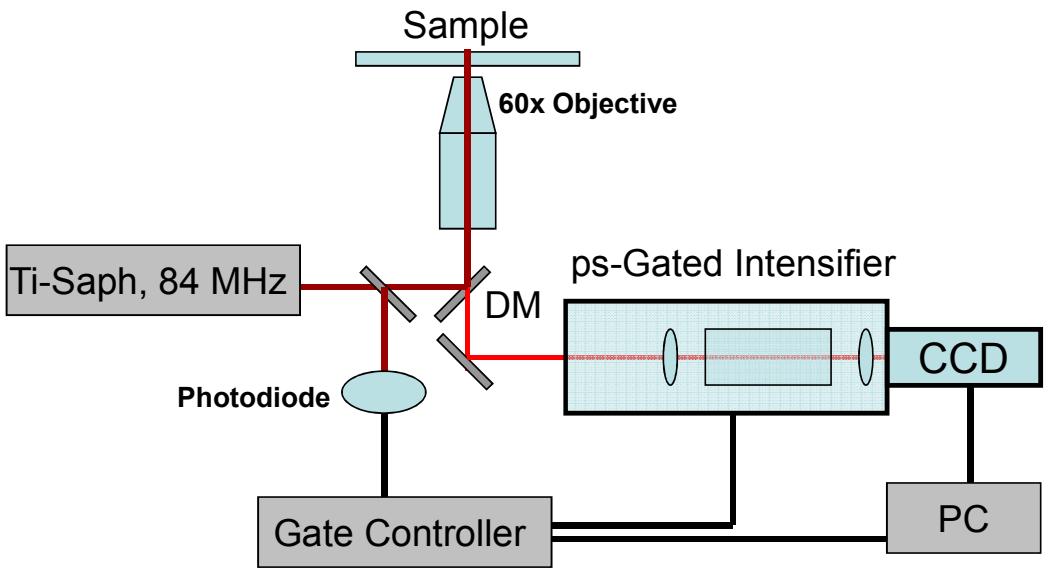

Figure 2.5 Schematic experimental setup for time-gated fluorescence lifetime imaging. A pulsed laser (typically a 84 MHz Titanium-sapphire laser) was used to excite the sample and trigger the power supply for the picosecond-gated (220 ps) intensifier, operating a multiplate channel photomultiplier tube (MCP-PMT). The MCP-PMT collected the emission photons from the sample, producing electrons which was then imaged by a phosphor screen, which was then imaged by a CCD camera. The camera and intensifier were both triggered by the excitation laser sync.

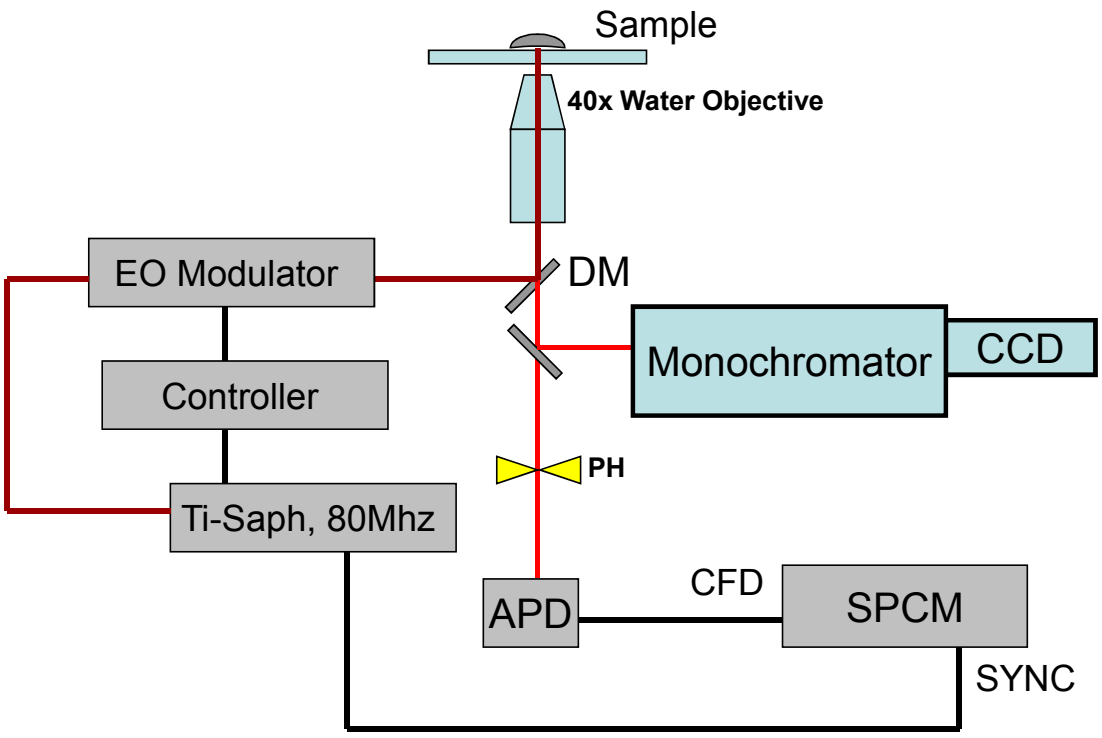

Figure 2.6 Schematic experimental setup for time-correlated single photon counting. The emission is collected and focused onto an avalanche photodiode (APD) and sent via a constant fraction discriminator (CFD) input towards the SPC module.

200mV). Therefore, as the APD produces TTL pulses, these must be inverted and attenuated before arriving at the board. The signal is then processed within the board through the constant fraction discriminator (CFD), time-to-amplitude converter (TAC), and finally the analog-to-digital converter (ADC). For all experiments unless otherwise stated, the “start” pulse, indicating the arrival of the photon, is used to begin the counting procedure, and the “stop” pulse, representing the arrival of the next excitation cycle, was used as the counter. This is referred to as “reverse” counting mode and its use is less taxing on the counting module than the chronological order. Multiple detectors may also be used simultaneously for the Becker & Hickl board, all processed through a routing channel, and this setup was required for photon antibunching and cross-correlation experiments.

There are two time scales which are tagged by the board, a higher resolution time scale referred to as the micro time and a longer time scale known as the macro time. The micro time gives dynamic information from the ps to the ns time scale, while the macro time gives μs to longer time scale information.

2.6 Fluorescence Correlation Spectroscopy

Fluorescence correlation spectroscopy is a type of single molecule experiment wherein the photophysical parameters, as well as hydrodynamic radii, can be measured for single emitters in solution. The technique was pioneered in the 1970’s, and has recently found many new uses, most notably in

the study of dye-labeled biological systems. A laser beam is focused in a dilute solution containing the fluorophore of interest, and as the probe passes through the laser beam, its emitted photons are collected and recorded. The system is setup so only emission from a measurable, fixed volume is observed, typically achieved by a placing a pinhole at a focal plane to reject out of focus light. FCS is fundamentally a time correlation experiment, therefore all of the useful information extracted from it is derived from the autocorrelation of the photon emission stream recorded from a passing molecule. Time dynamics falling within the time range of the experiment (the diffusion time on the long end, time resolution of the experiment on the fast end) are measured, including diffusion time, triplet dynamics, and radiative lifetime. FCS experiments employed the inverted fluorescence microscope setup discussed earlier. The excitation source was focused by a water-immersion objective (Olympus, 60x, 1.2 NA) into the sample solution. The resulting emission was then focused onto an optical fiber routed to an APD and tagged by the photon counting board.

2.7 Photon Antibunching

The behavior of single molecule emission can be identified in several ways, including the observation of fluorescence intermittency, dipole emission patterns, and photon antibunching. The last of these properties provides the most compelling evidence. Photon antibunching behavior arises from the definitive description of a single photon emitter, that the system can only emit

one photon at a time. By taking the autocorrelation of the photon emission stream from a molecule, one can see that the correlation at t = 0, ideally falls to 0, indicating that no photons are “bunched” together. The autocorrelation can be done by using a single detector and correlating the signal with itself, but a more practically useful setup necessitates the use of two detectors, each receiving a split photon stream from a 50/50 beam splitter. Quantum mechanics allows light to be modeled as particles, for which case the beamsplitter would send, with a 50% probability, the photon to one of the two detectors. No detector will measure a photon event at the same time if the photons are truly antibunched.

2.8 Ti-Sapphire Oscillator

To access significant nonlinearities in the electronic excitation of most dyes, a pulsed laser system is necessary to attain the high peak powers (and therefore photon density) required for simultaneous absorptions of multiple photons. It is for this reason that mode-locked femtosecond Ti-sapphire lasers are the most commonly used multiphoton laser. The femtosecond pulses allow peak powers to be about 5 orders of magnitude higher than corresponding continuous wave sources. For the majority of the results presented here, two different Ti-sapphire oscillators (Coherent; 10W Verdi-pumped Mira 900, KMLabs; Model TS) served as the excitation source. The Mira 900 offers a widely tunable range (690-1070nm) while also allowing the use of both femtosecond and picosecond pulses.

The high repetition rate of the lasers (80Mhz Mira; 83.9Mhz KMLabs) is useful for obtaining high emission rates necessary for many of the bulk and single molecule experiments described in this work. For some experiments, however, such as lifetime and absorption cross section experiments, it was necessary that the repetition rate be lowered to allow the molecules to return to the electronic ground state before arrival of the next pulse. An electro-optic modulator (ConOptics, Model 25D) was used to frequency-divide the pulse train by use of a polarization-rotating non-linear crystal.

2.9 Optical Pump-probe Spectroscopy

Nanosecond transient absorption measurements were performed as pump-probe experiments, as shown in Figure 2.7. A white light source (Newport, 250W tungsten lamp, 300W radiometric power supply model 69931) served as the probe while the pump is a tunable nanosecond laser (Newport- Spectra-Physics PRO-250-10, 8ns pulse, pumping an OPO). The energy is varied by using two beam splitter cubes each one preceded by a half wave plate. Waveplate orientation is controlled by Newport motion controller ESP-300. In order to work with a flat top beam and easily calculate the fluence, the laser beam is expanded by a telescope by a factor 4 and the central part is selected by using a 1 cm iris. The energy of the pulse is measured by a PE25BB pyroelectric head connected to a NOVA II OPHIR power meter and it is constantly checked during the measurement by a fast amplified silicon PIN detector (Newport 818-

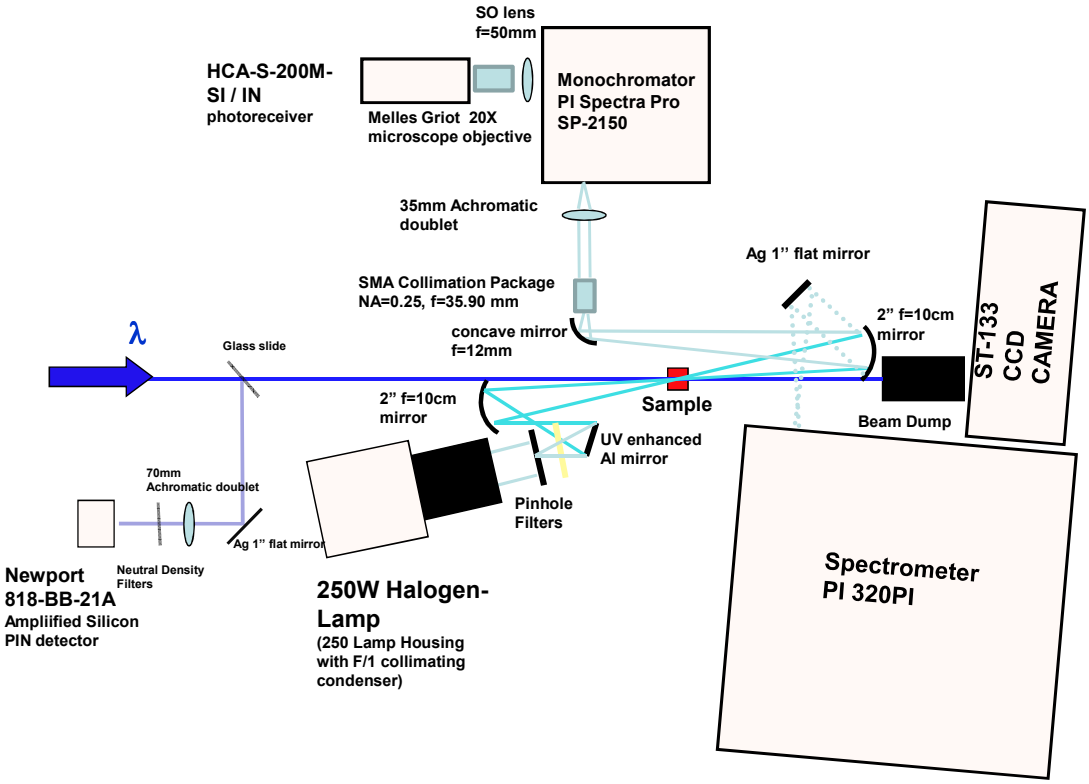

Figure 2.7 Schematic for the nanosecond pump transient absorption spectroscopy (Lab of J. W. Perry). Figure constructed by M. Cozzuol.

BB-21A). A glass slide is positioned along the beam path to redirect 4% of the pumping light towards to detector. The signal collected is sent to a SRS gated integrator that converts it in a DC output signal between 0 and 10 Volts. A National Instruments BNC-2110 and a DAQ interface are used to record the data onto a PC. The angle between pump and probe light is kept as small as possible. Single wavelength transient absorption time response could be recorded using a PI SP150 monochromator and a HCA-S-200M-SI (Si PIN) photo-receiver for the visible and a HCA-S-200M-IN (InGaAs PIN) photo-receiver for the near-IR part of the spectrum. Signal from the photoreceiver is detected trough a TDS 3034b Tektronix oscilloscope and recorded into the PC memory via GPIB interface. Gated transient spectra between 300nm to 900nm could be taken by using a PI320PI spectrometer and a ST133 CCD camera. A delay generator BNC model 575 is used to control the initial delay from the Q-switch laser trigger and the moment when the acquisition system starts. The hardware controlling the camera allows the tuning of the detecting gate and delay time, the signal gain and sequential spectra at increasing time delays. The ST-133 camera is triggered by a delay generator (BNC model 575) connected to the laser Q-switched ADV SYNC connector. Gate width and time delay are controlled by Winspec. Dedicated Labview software has been created in order to manage the files and create delta OD values at the end of each single measurement.

Femtosecond transient absorption spectra were acquired using a commercially available pump-probe spectroscopy system (Newport, Helios). The pump wavelength was tunable from 465 – 2900 nm and the pulses (~120 fs,

FWHM) were generated from an optical parametric amplifier (Newport, TOPAS) which, in turn, was pumped by a Ti:Sapphire regenerative amplifier (Newport, Spitfire) operating at a repetition rate of 1 kHz. The probe pulse was obtained by using approximately 5% of the fundamental 800 nm pump (Spitfire) to generate white-light continuum (420 – 800 nm) in a sapphire plate. The temporal step resolution of the system was 7 fs and the maximum extent of the temporal delay was 3200 picoseconds. The instrument response function was determined to be ~200 fs. At each temporal delay, data were averaged for 1.5 seconds. The pump beam was chopped at 500 Hz to sequentially obtain both pumped (signal) and non-pumped (reference) absorption spectra of the sample. A correction factor to account for the chirp of the white-light continuum probe was generated using the ultrafast response of $CHCl_3$ and was applied to all data sets. The data were stored as 3-D wavelength-time-absorbance matrices that were exported for use with the fitting software. The solutions were studied in 2 mm path-length cuvettes, and were stirred continuously throughout the data acquisition.

CHAPTER III
TWO-PHOTON ABSORPTION

3.1 Introduction

Silver cations are widely known to coordinate to the heterocylic bases of nucleotides, but most notably the hydrogen-bond positions of cytosine, which include the electron pairs of the N1 and O2 atoms.[23] Monomeric cytosine, in the presence of silver ions, forms polymeric complexes through bidentate ligand coordination, bringing together multiple silver atoms to within 3.3 angstroms, as measured in its crystal structure.[95, 96] For comparison, the calculated bond distance in the silver dimer is 2.5 angstroms.[103] Single-stranded oligonucleotides containing multiple cytosines, therefore, have the capability to bind multiple silvers and facilitate the stabilization of several atom clusters. Additionally, the bio-compatibility of polynucleotides and their versatile, commercially-available biomolecule coupling methods provide multiple options for introduction into biological environments.[104-106] Many useful dyes, however, are readily attached to proteins and nucleotides using simple and commercially available protocols.[107-109] So what advantage do silver clusters offer? From an imaging perspective, future applications continually demand brighter, more photostable dyes and higher-resolution imaging techniques.[110, 111] The utility of new fluorescent dyes can be justified if it can improve upon these critical parameters. Multiphoton imaging has already been proposed and implemented for high

signal-to-background imaging, as most cellular autofluorescence is eliminated through near-IR excitation, providing greater imaging penetration, especially beneficial in tissue imaging.[41-43] Commerical organic dyes are plagued by low TPA cross sections, however. Some of the best commercially-available water-soluble dyes, such as rhodamine 6G and Cy5, have TPA cross sections of 210 GM and 500 GM, respectively.[53, 54] Although significantly larger than most other dyes, which have cross sections on the order of 1-10 GM, they pale in comparison to semiconductor quantum dots, whose highest reported value in water is 68,000 GM, for CdSe/ZnS core-shell dots.[67] Their potential toxicity and large post-surface modification sizes, however, gives pause to their ultimate efficacy. [112, 113] Toxicity and biodegradation are salient issues for any *in vivo* and clinical applications. Large sizes can make cell uptake difficult and significantly perturb functionality, especially important for single molecule bio-labeling experiments.[105, 111, 114] Combining the large TPA cross sections and photostability of quantum dots and the small size and chemical versatility of organic dyes, oligonucleotide-encapsulated silver clusters are a potentially key element to an innovative, emerging tool for high resolution and higher sensitivity fluorescent imaging.

3.2 Basic Photophysical Properties

Silver clusters are characterized by their high emission rates, resulting from high quantum yields and strong absorption cross-sections, as well as their

remarkable photostability.[22, 24, 84] Clusters of 2-8 atoms strike a delicate balance between the strong plasmon absorption of large nanoparticles and the narrow transitions of single atoms. Clusters can be made to emit at a variety of wavelengths ranging from the blue to the near-IR. Size-selected, noble-gas encapsulated silver clusters have tunable absorption and emission wavelengths as a function of cluster size and structure.[115] Additionally the nature of the encapsulating matrix can significantly affect transition energies, as shown by the variation of cluster absorption and emission in argon, krypton, and neon matrices.[35, 39] The multiplicity of the many variables determining cluster emission result in a system that can emit at almost any desired wavelength. Precluding an intimate understanding of these complex factors, however, it becomes nearly impossible to *a priori* design and successfully synthesize monodispersed clusters of a desired structure. Monodispersity is rarely achieved reproducibly even in larger, several-nanometer particles. Fortunately, oligonucleotide encapsulation provides a way around this problem. Because multiple silver ions can have specific interactions with multiple bases within one strand, the sequence of the bases can ultimately facilitate the formation of well-defined clusters upon reduction. Whereas polycytosine sequences yield a wide distribution of emitters,[84] sequences incorporating adenine, thymine, and cytosine in specific arrangements have been shown to produce clusters of high emissive purity.[22] The precise arrangements of these bases have been determined by microarray analysis, as reported elsewhere.[22] DNA enables tunability of cluster properties without needing to exhaustively grasp the complexity of this condensed-phase

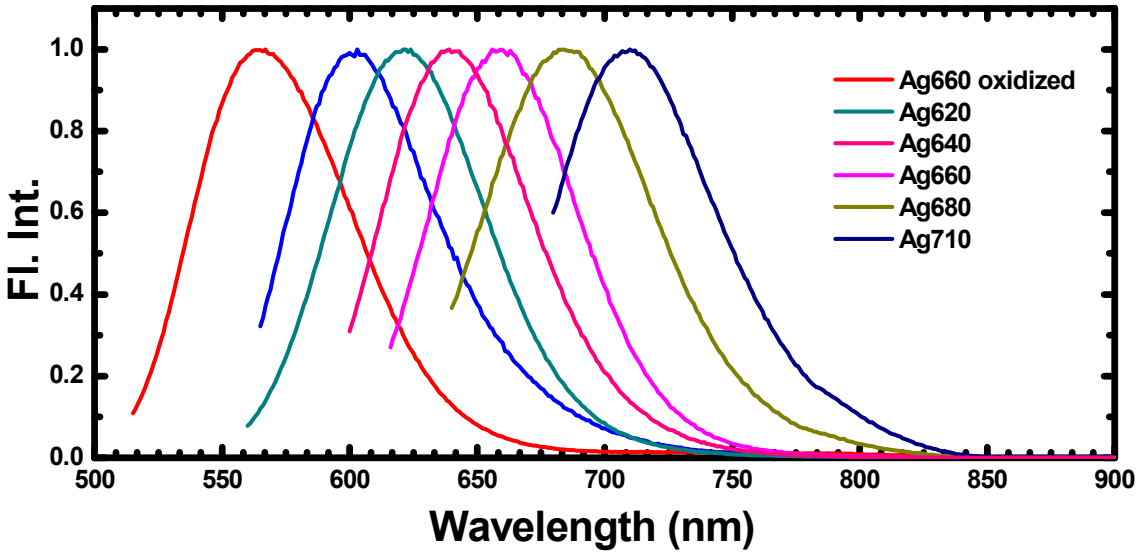

Figure 3.1 Emission spectra of the oligonucleotide-encapsulated silver nanoclusters discussed in this thesis. The clusters are labeled by their primary emission peak. All species shown here are the result of reduction of the silver ions in the presence the oligonucleotide, except for the 560 nm emitting species, which is the result of subsequent oxidation of the Ag660 sample, occurring over periods of several days to weeks at room temperature. The strand sequences used to synthesize individual emitters is discussed in the text.

system. The extinction coefficients of a few representative red and near-IR emitting silver clusters have been measured to be $1.2\times10^5 M^{-1}cm^{-1}$ for the Ag620 emitter and $3.5\times10^5 M^{-1}cm^{-1}$ for the Ag660, Ag680, and Ag710 emitters.[116] These are up to approximately 3 times larger than rhodamine 6G ($1.2\times10^5 M^{-1}cm^{-1}$),[117] begging the question of how the clusters can possess such large transition strengths. Though consisting of only a few atoms, each atom can contribute one free electron, and the overall transition may reflect the transition strengths of multiple electrons. The oscillator strength is a quantitative measure of the transition strength and is classically defined as,[30]

$$f = \frac{8\pi m_e \nu}{3he^2}\mu_{mn}^2 \tag{3.1}$$

in which μ_{mn} is the transition dipole moment between states n and m, m_e is the effective electron mass, and ν is the transition energy in cm^{-1}. For a one electron system whose response to an electric field is perfect, the oscillator strength is unity. Theoretically this upper limit cannot be breached unless multiple electrons participate in the transition, as is the case for band-gap materials and free-electron metals. The oscillator strength can be experimentally measured by the integrated area of the extinction coefficient of absorption (ε) as a function of energy (in cm^{-1}) by the following,[30]

$$f \equiv 4.3\times10^{-9}\int \varepsilon(\nu)d\nu \tag{3.2}$$

Oscillator strengths for many of the fluorescent silver clusters were calculated based on their absorption spectra and measured extinction coefficients, and were found to be 1.36 for Ag620, 3.78 for Ag660, 5.09 for

Ag680, and 2.86 for Ag710. For comparison the oscillator strength of a strongly-absorbing, one-electron system such as rhodamine 6G was measured to be 1.01. All of these values exceeded that expected for a one-electron transition, confirming that the total absorption strength for each of the clusters not only draws on multiple electrons, but for each one it appears that different numbers of electrons may be participating. Although no conclusions can be drawn on the number of atoms in each cluster based solely on its oscillator strength, it does imply that the number is equal to or larger than the value, assuming that each atom contributes one s-electron. The possible contribution of d-electrons, although unlikely at such low energies,[14] complicates the interpretation.

The high oscillator strengths indicate that there is a large transition dipole moment between the ground and first electronic states. One would therefore expect the excited-state electronic distribution to significantly shift from that of the ground-state. Using equation 3.1, μ_{mn} is calculated to be 12.6 Debye for the Ag620, 22.0 Debye for Ag660, 24.8 Debye for Ag680, and 22.6 Debye for the Ag710 emitter. A Debye is defined as the dipole moment of one unit of electric charge separated by 1 Å.

Changes in the solvent dielectric function and its effect on the absorption and emission energies can also provide experimental information on the relative dipole moments of the ground and excited states. Different solutions of the Ag660 emitter were made in varying solvent conditions and the resulting spectral energies were recorded. Because all synthesis thus far could only be successfully carried out in aqueous conditions, concentrated solutions were

initially prepared and subsequently diluted in an appropriate solvent. The number of solvents available was limited, because solvents were required to both dissolve DNA and be miscible with water. Ethanol, methanol, tetrahydrofuran (THF), dimethyl sulfoxide (DMSO), acetone, acetonitrile, dimethylformamide (DMF), ethylene glycol, and isopropanol were used. Following preparation, the solutions were stored at 4° C for 2 hours to allow equilibration. Absorption spectra, plotted in Figure 3.2, show that the absorption peak position shifts in varying solvent conditions. Plotted in terms of the dielectric constant, which is the square of the solvent refractive index (n^2),[118] there is a clear shift towards higher energies with decreasing n^2. Emission spectra similarly shift towards higher energies. In all of the emission spectra, the excitation wavelength was kept at the maximum observed in water (595 nm for the Ag660 emitter) despite the shifting absorption maxima. This was done primarily to avoid exciting other potential emissive species and thereby artificially shifting the peak emission wavelength. In water this is not typically a problem as spectrally pure species can be synthesized. Upon dilution into other solvents, however, more broadly distributed species are formed, and the excitation of multiple species is likely. Therefore the shift in emission wavelength that is observed is attributed to purely solvatochromic effects.

The quantum yield and radiative lifetimes were also measured for each solution, as quenching effects due to solvent damping of the excited state are known to occur. The radiative lifetime and quantum yield of the Ag660 emitter in water has been measured to be 3.0 ns and 18%, respectively. For each of these

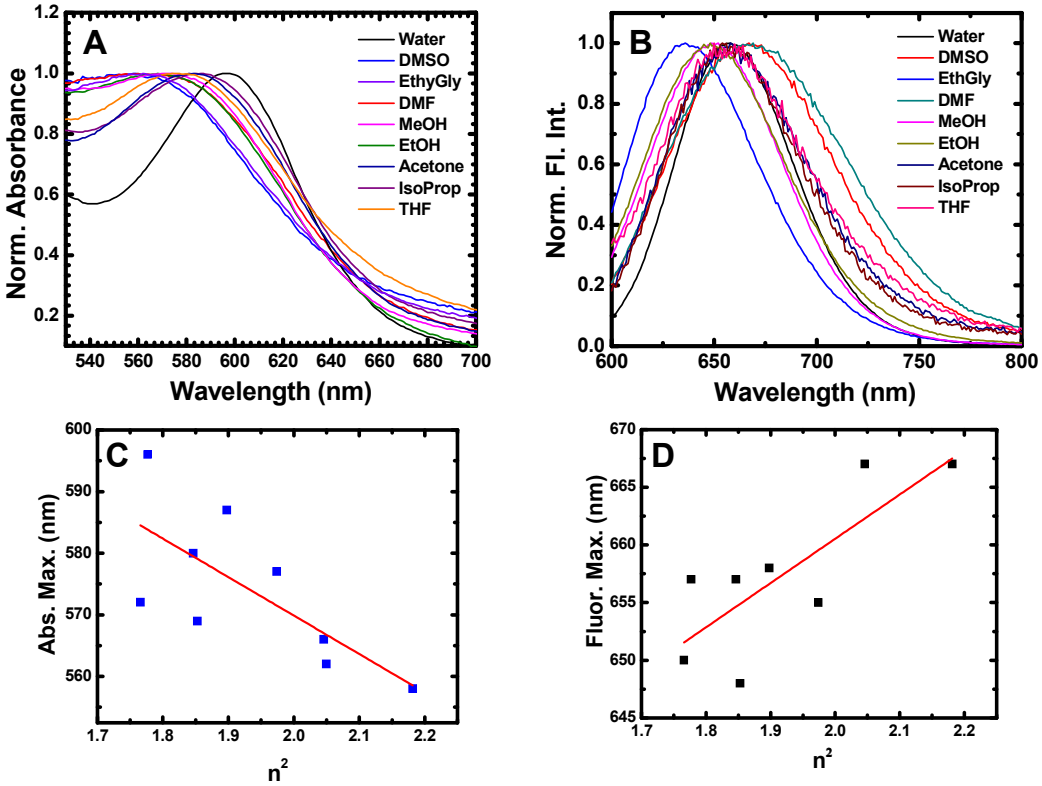

Figure 3.2 (A) Normalized absorption spectra of the Ag660 emitter dissolved in various water-miscible solvents. Solution preparation is described in the text. (B) Normalized fluorescence spectra of the same solutions, all excited at 595 nm. (C) The peak absorption wavelengths were plotted as a function of the frequency-dependent dielectric function (n^2) and linearly fitted with an R^2 value of 0.45. (D) Fluorescence maximum plots, fitted with an R^2 value of 0.56.

solutions, the lifetime was measured by exciting at 372 nm with a picosecond diode laser. Though this is significantly shifted from the primary excitation peak (595 nm), other minor peaks appear in this UV range, resulting in the same emission peak at 660 nm. The lack of an adequate excitation source at 595 nm prevented the use of this preferred wavelength. The results are shown in Figure 3.3 Lifetime fits were made for most of the samples using a single exponential fitting routine, although in several cases (methanol, ethanol, DMSO, DMF) the fit was made using a bi-exponential decay, as two components (one ~200 ps and the other at ~2.5 to 3 ns) appeared. For these cases the weighted average was calculated and plotted as a function of the solvent polarizability (Figure 3.3b) given by,[119]

$$\Delta f = \left(\frac{\varepsilon - 1}{2\varepsilon + 1} - \frac{n^2 - 1}{2n^2 + 1} \right) \tag{3.3}$$

in which the first term depends on the static dielectric, while the latter term is frequency-dependent. The parameter Δf is the difference in static and orientational polarizabilities. A slight trend seems to appear in which the lifetime decreases as a function of polarizability. Quantum yield measurements (Figure 3.3c) confirm this behavior as the emission appears to be quenched for more non-polar solvents. Although by no means definitive, specific solvent interactions with either the DNA or the silver cluster can potentially alter a trend based purely on dielectric function.

A more accurate account of this can be found by measuring the Stokes shift (the energetic difference in absorption and emission maxima) of the primary

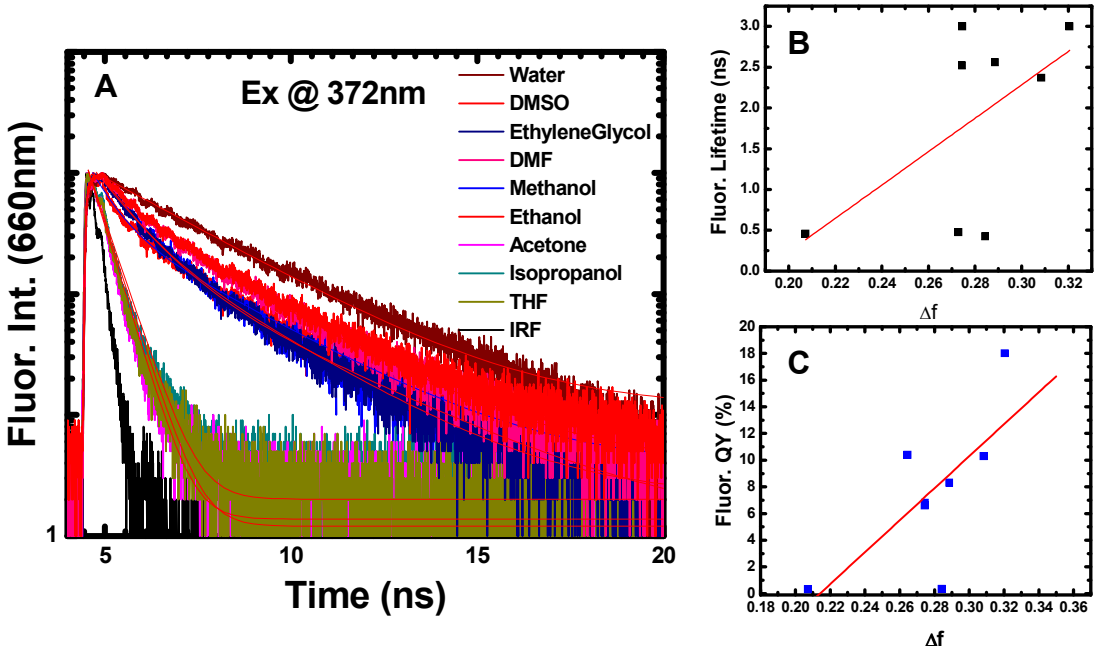

Figure 3.3 (A) Fluorescence lifetime curves of the Ag660 emitter in the indicated solvents. The samples were irradiated by 372 nm, ~80 ps, 10 MHz diode laser pulses (Picoquant). The emission was detected by a cooled MCP-PMT and recorded in a time-correlated single photon counting mode. (B) The decay curves were fit either mono- or bi-exponentially and the weighted average was used as the data point as a function of Δf, as indicated in the text. (C) The fluorescence quantum yield of the same solutions were then measured by comparing the maximum absorbance to that of the known water sample (= 0.18). The original concentration of emitters in each sample were identical, although subsequent redistribution of different emitters upon dilution was not taken into account.

emissive transition. This experiment can yield the dipole moment change. Upon excitation, the solvent reactively realigns its dipoles to the most energetically favorable state. The reorganization can occur on various time scales, which depends on either the static dielectric constant ε (slow) or the frequency-dependent dielectric function n^2 (fast). The former determines the static polarizability, while the latter determines the orientational polarizability. The Lippert-Mataga equation describes the relationship among solvent polarizability, the Stokes shift, and the dipole moment change, written as,[119]

$$\nu_A - \nu_B = \frac{2(\mu_E - \mu_G)^2}{hca^3}\Delta f \qquad (3.4)$$

in which a is the Onsager radius, and μ is the dipole moment of the ground and excited states. To measure the dipole change value, the Stokes shift, for the Ag660 emitter, was plotted as a function of Δf for a variety of water-miscible solvents (Figure 3.2). A linear fit was then used to extract the dipole change from the slope, where an Onsager radius of 1 nm was chosen. It can be seen in the plot that a significant trend is observable, with the Stokes shift decreasing with increasing Δf. The change in dipole moment ($\Delta\mu$) was found to be 43.0 ± 24.0 Debye for the series of solvents, while for a pure ethanol-water series the dipole change was 63.4 ± 4.0 D.

The change in absorption/emission maxima upon solvent change can be complicated to interpret, especially if there are significant chemical interactions between the species and the solvent. The two solvent series plots show that

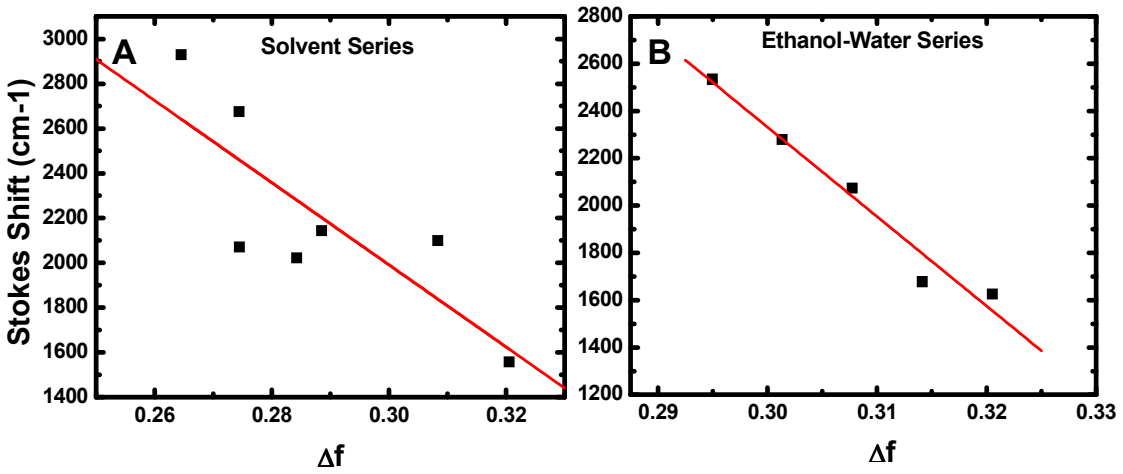

Figure 3.4 Lippert-Mataga plot of the 660nm emitting species. The solvent dielectric function was changed by (A) transferring the species to a variety of water-miscible solvents, and (B) by the variation of the ethanol-water ratio. The absorption and emission spectra were measured in each solvent and the slope of the fitted line was used to calculate the dipole change from the ground state to the excited state, according to the Lippert-Mataga equation. The change was calculated to be $\Delta\mu$ = 43.0 ± 24.0 D (A) and 63.4 ± 4.0 D (B).

while the ethanol-water series fits well to a linear trend ($R = 0.955$), the series using a variety of solvents, from aprotic to extensively hydrogen-bonding, fit less uniformly ($R = 0.589$) to the trend. Because the DNA phosphate backbone is highly charged, a significant hydrogen-bonding network is formed around the oligonucleotide in order to stabilize its structure.[85] Changes in solvent may disrupt this stability and in turn shift the transition energy levels to a more complex degree than expected from its polarizability. In the ethanol series, the hydrogen-bonding capability of ethanol might provide a more accurate effect due to solvent polarizability. Additionally, since the clusters were originally made in an aqueous environment and subsequently transferred to another solvent, 5% water by volume remained in the solution. This small amount may still play a significant role in solvation of the highly hydrophilic DNA. This may account for some of the discrepancy between the transition dipole moment calculated from the absorption spectra and the dipole moment change in the solvent experiments. More accurate Stark spectroscopy studies are underway to measure this value directly.

Despite the difficulties in interpretation, it is clear that there is a significant movement in electronic distribution upon optical excitation, resulting in strongly-allowed transitions with high rates of emission. Because the highly mobile valence electrons of silver result in highly desirable one-photon excited optical properties, it is also expected that these same intrinsic features of the silver cluster will make possible strong two-photon absorption (TPA), which will be discussed in the next section.

3.3 Two-photon Excitation Spectra and Absorption Cross Sections

3.3.1 Two-photon Absorption

The TPA spectra of a variety of emissive species were recorded, and many fell within the central Ti-sapphire range (750-900nm), allowing easy access by any Ti-sapphire oscillator. The emission spectra and radiative lifetimes (excited at double the TPA excitation energy) were indistinguishable for OPE versus TPE, indicating that both excitation processes lead to the same emissive state, with relaxation to that state occurring much faster than the fluorescence lifetime. Interestingly, however, the excitation spectra for OPE versus TPE do not overlap, with a blue-shift in the TPE spectra (when doubled in energy) greater than expected from vibrational shifts expected from selection rule differences. The shift (1-2 eV) is on the order of electronic transitions, indicating that TPE leads to excitation to a new electronic state. This is discussed in more detail in the following section (3.2.2).

The fluorescence rate from two-photon absorption is a function of TPA cross section, collection efficiency, concentration, excitation intensity, and the excitation spatial and temporal profiles. Absolute cross section measurements, therefore, can be complicated and somewhat irreproducible. The expression for the total detected fluorescence output is given by the following,[54]

$$\langle F(t)\rangle = \frac{1}{2}\phi_{FL}\phi_{CE}C\sigma^{TPA}\frac{g_p 8n\langle P(t)\rangle^2}{\Gamma_{rep}\tau\pi\lambda} \qquad (3.5)$$

in which Γ_{rep} is the pulse repetition rate, τ is the FWHM of the pulse temporal profile, n is the refractive index, C is the dye concentration, λ is the excitation wavelength, ϕ_{CE} is the total instrument collection efficiency, and $g_p/\Gamma_{rep}\tau$ is defined as the degree of second-order temporal coherence of the laser. The need to evaluate most of these parameters, however, can be eliminated by employing a ratiometric method, in which the sample emission could be compared to that of a reference dye under the same excitation and collection conditions. Two-photon quantum yields are difficult to measure directly, and it is often assumed that they are equivalent to one-photon quantum yields, given that both processes lead to the indistinguishable emission spectra and radiative lifetimes. Therefore in all the following analyses it was assumed that $\phi_{FL}(OPE) = \phi_{FL}(TPE)$, and for dyes whose quantum yields are not known, the action cross section ($\phi_{FL}\sigma^{TPA}$) was reported instead.

Therefore by comparing the emission rates of two dyes, one of which has a known TPA cross section, all but a few variables are eliminated. The relative concentration and quantum yield are all what is needed to determine the unknown cross section. Quadratic excitation intensity dependent regions were identified for each Ag nanocluster and reference dyes. Accounting for concentration and quantum yield differences, the ratios of emission intensities in quadratically-dependent excitation intensity regions enabled the calculation of cross sections. Each nanocluster cross section measurement was referenced to two separate reference dyes (rhodamine B,[54] rhodamine 6G,[120] fluorescein (pH=11),[120] or Cy5,[53] Figure 3.5) to provide a cross-reference for accuracy. All

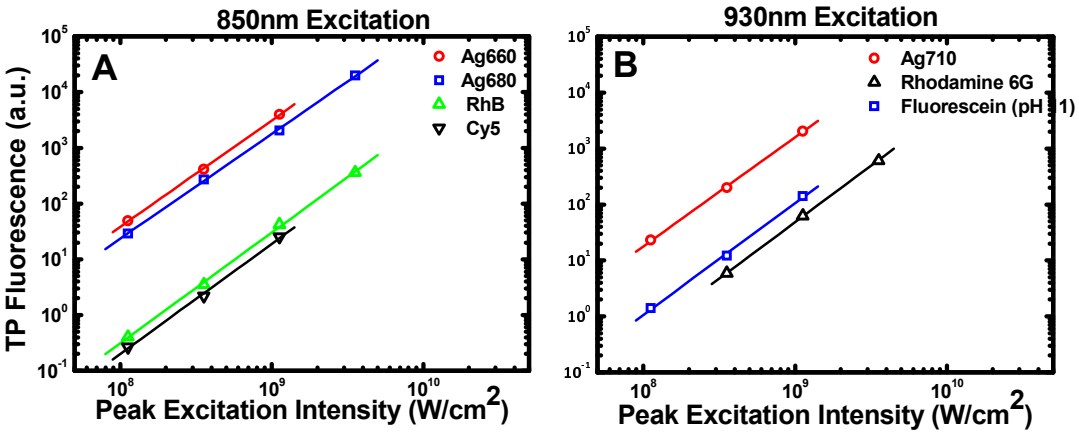

Figure 3.5 Excitation intensity dependence (log-log plot) of the near-IR silver emitters as compared with reference dyes rhodamine B, rhodamine 6G, Cy5, and fluorescein. The common quadratic region of the intensity curve was found for the dyes, and the relative fluorescence, corrected for concentration, is shown here at two excitation wavelengths. The ratio of the fluorescence, which was then corrected for quantum yield differences, was used to determine the two-photon absorption cross section. All the measurements were done with a femtosecond Ti-sapphire laser frequency-divided to 8 kHz, ensuring all molecules returned to the ground state before the arrival of the next excitation pulse, as evidence of transitions to microsecond states has been observed.

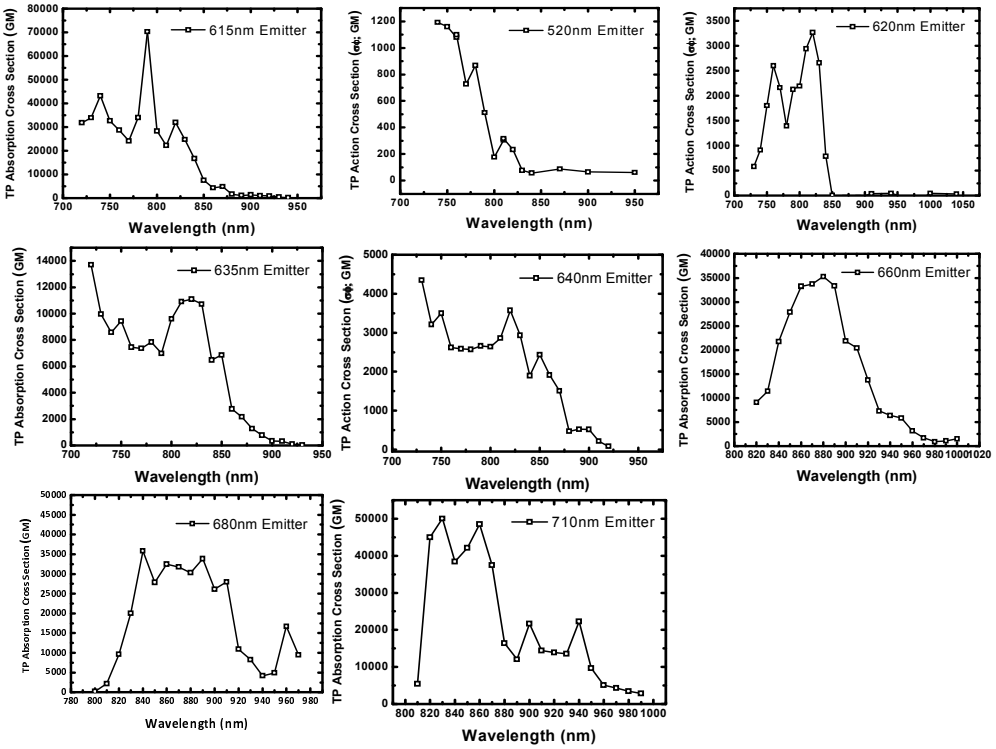

Figure 3.6 Two-photon excitation spectra of a variety of oligonucleotide-encapsulated silver clusters. The spectra are calibrated to either the action cross section (Ag520, Ag620, Ag640) or to the absorption cross section (Ag615, Ag635, Ag660, Ag680, Ag710) for those species whose quantum yields are known (shown in Table 3.1). All of the curves were generated by recording the emission as a function of excitation wavelength by a 8kHz femtosecond Ti-sapphire laser. The cross sections were measured by ratiometric comparison to dye standards with known cross sections at the excitation wavelengths used.

cross section measurements were performed at an 8 kHz excitation rate, ensuring that all molecules returned to the ground state before the arrival of the next excitation pulse.

The absorption cross sections of all the near-IR emitters were measured as a function of excitation wavelength. As shown in Figure 3.4, the cross section for the 660nm emitter peaks at 35,000 Goppert-Mayer (GM) units (10^{-50}cm^{4}photon/s), while the 680nm emitter peaks at 34,000 GM, and the 710nm emitter reaches 50,000 GM.[20] These cross sections are close to the value of water-soluble quantum dots (66,000 GM)[67], with brightnesses far exceeding that observed for the best water-soluble two-photon dyes.

3.3.2 Symmetry and Selection Rules

The relative transition strengths for OPE and TPE are highly symmetry-dependent. How allowed a particular transition is provides insight into how faithfully the conventional parity rules (g-u for OPE, g-g for TPE) apply and therefore the chromophore symmetry. For instance, a distinction is observed between more symmetric organic dyes, such as rhodamine B, DiI, and Fluorescein, with those having no center of symmetry, such as Cascade Blue, coumarin 307, and Indo-1.[54] The latter group shows TPE spectra nearly identical with OPE spectra, suggesting that the parity rules are relaxed. For the centrosymmetric group, however, the TPE spectra are significantly blue-shifted relative to the OPE spectra, indicating that the first excited state is not accessible by TPE, and the transition occurs to a state that is accessible by TPE.

***Table 3.1*. OPE and TPE Photophysical values of Ag Nanoclusters**

	OPE ex. (nm)	TPE ex. (nm)	σ (GM)	Φ	τ_{OPE} (ns)	τ_{TPE}(ns)
Ag615	575	790	70,000	0.42	2.5	
Ag620	540	820	3,300[a]		2.2	
Ag635	575	820	11,100	0.26	2.7	
Ag640	560	820	3,600[a]			
Ag660	595	880	35,300	0.18	3.0 ± 0.02	3.1± 0.02
Ag680	620	890	33,900	0.37	3.0± 0.02	3.0± 0.02
Ag705	633	930	13,600	0.31	3.5± 0.02	3.4± 0.02
RhB	595	840	210	0.31		
Cy5	635	785	400	0.27		

[a] These values are action cross sections as quantum yields were not known

The excitation spectra of oligonucleotide-encapsulated clusters are blue-shifted with respect to the OPE peak, indicating that TPE accesses a higher excited electronic state than does OPE (Figure 3.5). The OPE excitation spectra of the Ag620 and Ag680 species show, in addition to the primary electronic transitions beyond 500nm, much less efficient excitation at higher energy overlapped with the doubled TPE transition energy. Though the Ti-sapphire range does not permit direct excitation at half the transition energy of the primary OPE transition for the near-IR emitters (i.e. $\geq$1150nm excitation), the 620nm species was used to probe the TPA excitation spectra over an overlapping range. No pre-resonance by TPE, however, was observed upon approaching the OPE resonance at 1080nm. So the OPE and TPE transitions leading to fluorescence are orthogonal. Since the parity rules appear to be relevant, it suggests that they possess inversion symmetry. This is no surprise if one considers the fluorophore as a globular, several-atom silver cluster.

3.3.3 Fundamental Limits of the TPA Cross Section

In order to properly put into context the large TPA cross sections measured, the values were compared with the maximum theoretical values for a two-photon absorption transition. The TPA cross section is a function of the second hyperpolarizability, shown by the equation:[121]

$$\sigma^{TPA}(\omega) = \frac{4\pi^2\hbar\omega^2}{n^2c^2}\left\langle \gamma(\mathrm{Im}) \right\rangle \qquad (3.6)$$

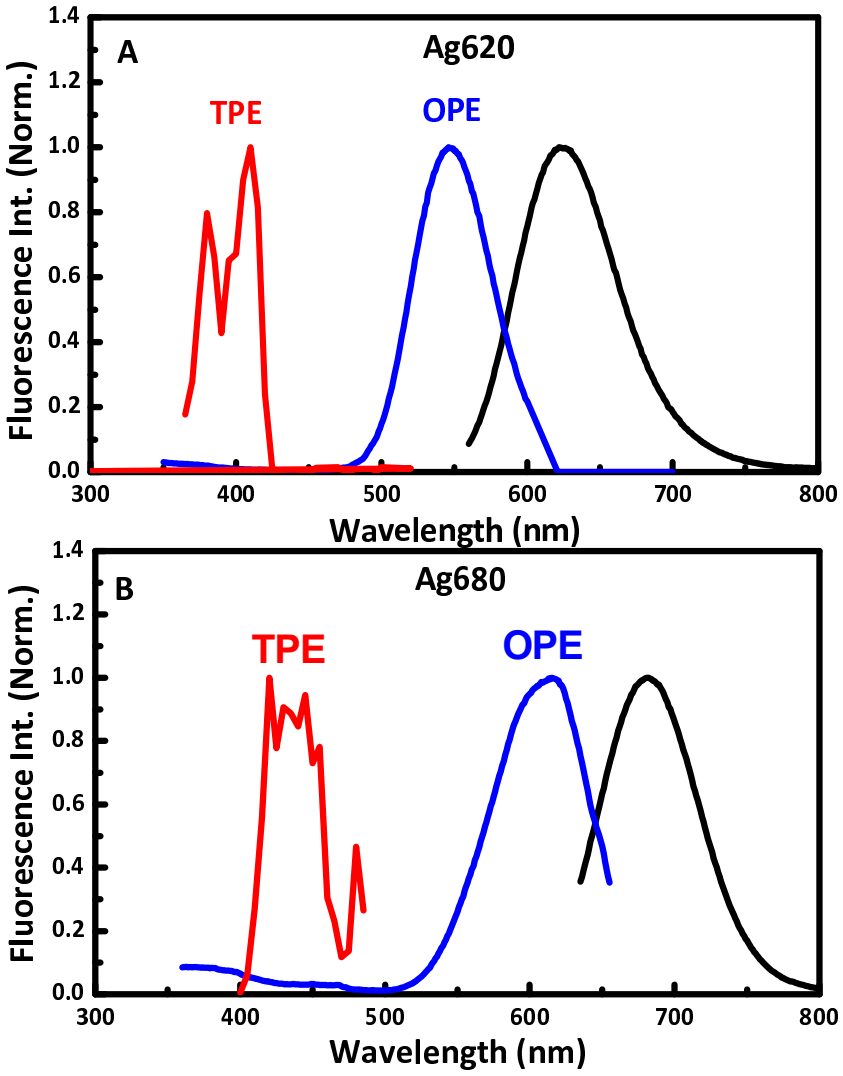

Figure 3.7 OPE and TPE (doubled in energy) spectra are shown along with the emission spectrum (black) for (A) 620 nm emitter and the (B) 680 nm emitter. Only a small portion of the OPE overlaps with the TPE spectrum (out as far as1040 nm), but no overlap with the principal OPE peak at 540 nm is observed. In (B) there is overlap of the TPE peak to the weak OPE at around 430nm. The OPE and TPE curves are separately normalized to unity based on the emission output.

in which n is the refractive index, c is the speed of light, and $\langle\gamma(\mathrm{Im})\rangle$ is the orientationally-averaged, imaginary term of the second hyperpolarizability. The hyperpolarizability can be expressed as a sum-over-states expression of the two dominant electronic transitions of two-photon absorption, the one-photon transition and the combined two-photon transition,[122, 123]

$$\gamma = \frac{4\mu_{01}^2\mu_{02}^2}{(E_{10} - \hbar\omega - i\Gamma_{10})(E_{20} - 2\hbar\omega - i\Gamma_{20})} \tag{3.7}$$

in which μ_{mn} is the transition dipole moments of each transition, E_{mn} is the energy difference, and Γ_{mn} is the damping factor. In this expression resonance can occur at either transition, but in this case only the two-photon resonance will be considered. The orientational average is estimated based on the estimated molecular shape and electron transition direction. For a one-dimensional system, as is the case for most organic dyes, $\langle\gamma\rangle = \gamma/5$, but for spherical systems $\langle\gamma\rangle = \gamma$. We will assume a spherical geometry for the silver clusters, the maximum will be five times larger than for a one-dimensional molecule.

The fundamental limit of the resonant TPA cross section can then be estimated by employing sum rules to the imaginary portion of the hyperpolarizability, simplifying the sum of the states in the transition matrix and maximizing the value. The hyperpolarizability is then plugged back into the cross section equation, which results in[121]

$$\sigma_{res}^{\max} \approx \left[317.5 \left\{ \frac{1}{n^2} \left(\frac{n^2+1}{3} \right)^4 \right\} \left(\frac{E_{20}}{2E_{10} - E_{20}} \right)^2 \left(\frac{E_{20}}{\Gamma_{20}} \right) \left(\frac{N^2}{E_{10}^3} \right) \right] \tag{3.8}$$

in which N is the number of participating electrons. The limit scales quadratically with the number of participating electrons, making it highly sensitive to molecular size. Organic systems designed for large TPA cross sections are typically large conjugated molecules with strong electron donating and accepting groups. Their overall efficiency, however, drops significantly as a function of size, as evidenced by $\sigma^{TPE}/\sigma^{TPE}_{max}$ ratios less than 0.01 for the most strongly absorbing systems, down from 0.25 for smaller chromophores.

For silver clusters, a value of ~210,000 GM for a 5 electron system is calcluated, with n=1.5 (considering the higher index of the surrounding DNA[124]), assuming a spherical cluster shape. Though the number of participating electrons is not precisely known, previously reported results suggest that N≤5,[23, 83] which would lead to $\sigma^{TPA}/\sigma^{TPA}_{max} \geq 0.24$. The maximum theoretical value calculated according to the equation 3.8 presents a fundamental limit, and as such does not account for the extra limits to this value imposed by the nature and structure of the chromophore. Therefore any meaningful interpretation of this ratio must take into consideration these general constraints. Dipole transition strengths are proportional to both the sum of the polarizability of all the electrons and the intensity of the incident electric field. Conjugated organic dyes can have large numbers of electrons participating in the transition, but it is not possible for all of the electrons to move along the entirety of the molecule. The electrons are typically associated to pi-bonds, and though significant charge separation does occur, it usually does so with only a few charges, resulting in the lower cross section value. In noble metal clusters, however, the Drude model states that the

outer electronic shell contributes “free” electrons, and is responsible for the strong plasmon absorption bands seen in larger systems.[14, 125, 126] Though smaller clusters possess discrete absorption and emission bands, it is evident that the free electron behavior still applies, accounting for the large $\sigma^{TPA}/\sigma^{TPA}_{max}$ ratios.

3.4 Single Molecule Studies

3.4.1 Two-photon Fluorescence Correlation Spectroscopy

The count rates for two-photon fluorescence correlation spectroscopy were significantly lower than for OPE, which is a result of both pulsed excitation which limits the excitation duty cycle and a smaller effective excitation volume due to the superlinear intensity dependence. FCS experiments can also be used to determine the hydrodynamic radii of fluorophores. The diffusion of molecules through the focal volume of the laser generates a decay in the autocorrelation curve corresponding to the characteristic diffusion time. The autocorrelation of a time function $F(t)$ is written as,[127]

$$G(\tau) = \frac{\langle \delta F(t) \cdot \delta F(t+\tau) \rangle}{\langle F(t) \rangle^2} \tag{3.9}$$

in which $\delta F(t)$ is the deviation from the temporal average, expressed as $\delta F(t) = F(t) - \langle F(t) \rangle$. For a fluorescent molecule diffusing through a 3-dimensional Gaussian-shaped laser beam, the autocorrelation takes on the form,[127, 128]

$$G_{Diff}(\tau) = \left(\frac{1}{1+\tau/\tau_{Diff}}\right)\left(\frac{1}{1+(\omega_0/\omega_z)^2(\tau/\tau_{Diff})}\right)^{1/2} \quad (3.10)$$

in which ω_0 is the distance the excitation beam has decayed to $1/e^2$ in the x,y directions, ω_z is the distance in the z direction, and τ_{Diff} is the diffusion time. Using the fitted diffusion time of a reference dye (rhodamine 6G) whose diffusion constant in water (D) is known,[129] ω_0 can then be determined by the relationship $\tau_{Diff} = \omega_0^2/4D$.[128] The fitted diffusion times through the focal volume for the Ag cluster samples can then be used to determine the diffusion constants. The Einstein-Stokes equation ($D = k_B T/6\pi\eta R_h$)[130] relates the diffusion constant of a solute to its hydrodynamic radius (R_h). Ratiometric methods were used here to determine the radii of the DNA-encapsulated clusters. The aqueous diffusion constant of rhodamine 6G has been reported to be $3.0 \pm 0.8 \times 10^{-6} cm^2 s^{-1}$, which corresponds to an R_h of 7.1 Å.[131] The diffusion times were then measured for rhodamine 6G, Cy5-labeled C_{12}-DNA, and the Ag660, Ag680, and Ag710 emitters. The excitation wavelength (830nm) and intensities were kept constant for all samples, ensuring their reliable comparison. The diffusion time for the control, rhodamine 6G, was found to be 77 μs, the Cy5-DNA control was 210 μs, and the Ag710 emitter was 177 μs. These values were extracted directly from the autocorrelation of the FCS time trace using equation 3.10. From this, the hydrodynamic radii were calculated by taking the ratio of diffusion times and applying that ratio to the hydrodynamic radius of rhodamine B. Ag660, Ag680,

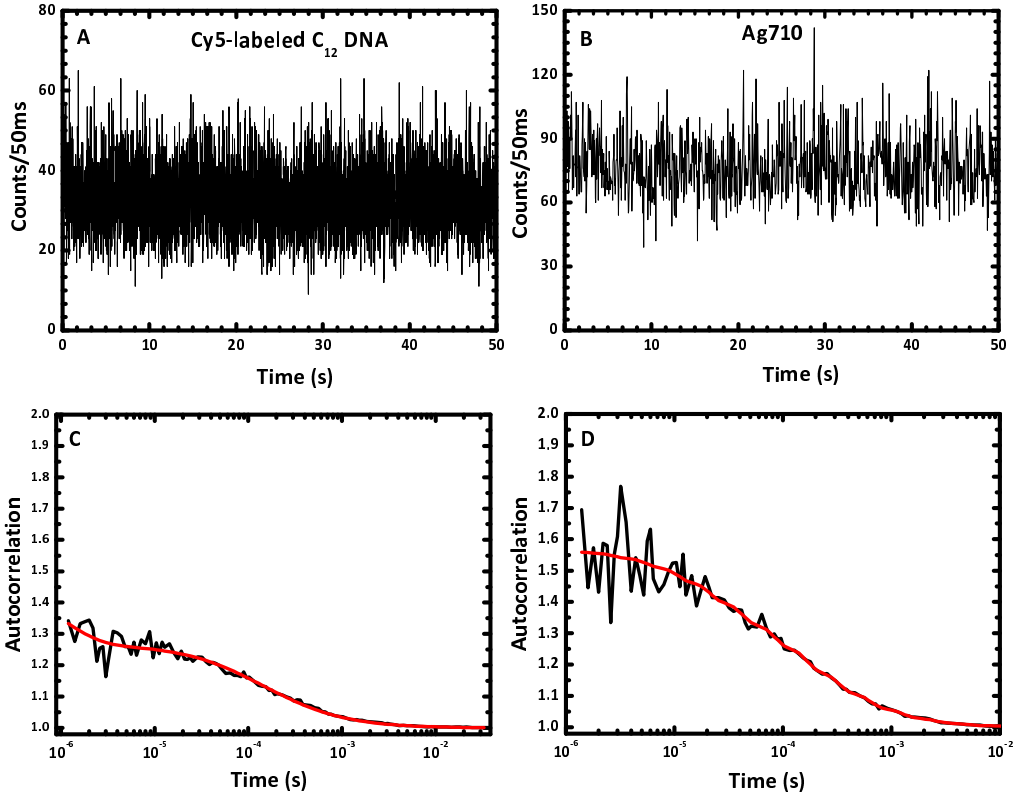

Figure 3.8 Fluorescence correlation spectroscopy comparison between Ag710 and a Cy5-labeled C_{12} standard using two-photon excitation (830nm, 80Mhz, 100fs pulses). The time traces (A and B) in 50ms bins shows the individual bursts in and out of the focal volume. The autocorrelation (C and D) was used to determine the diffusion times, from which the hydrodynamic radii were calculated by comparing to a Rhodamine 6G standard (not shown). The hydrodynamic radii for the C_{12} without and with the silver cluster were 2.7nm and 2.3nm, respectively.

and Ag710 (all ~2.3nm) are found to be smaller than Cy5-labeled 12-mer DNA (2.7nm). This result is consistent with previous results suggesting that the fluorophore is comprised of 2-8 silver atoms. The comparison made here, however, is not the fairest comparison, because Cy5 is expected to contribute to the overall radius of DNA. A better comparison (which has not been directly made) would be to measure the relative radii of a silver cluster species also containing Cy5 (or another molecule of comparable size). Additionally, dynamic light scattering can be used to directly measure the hydrodynamic radii of the DNA before and after addition of silver and synthesis of its clusters. Neither of these experiments was performed, but it will be of use for future studies to obtain accurate values.

3.4.2 PVA Polymer Film

Considering the high photostability of Ag clusters in OPE single molecule studies,[22, 24] it is believed that single TPE will be similarly stable compared with commercial organic dyes. Ensuring one is observing single molecules when embedded in host polymers or on surfaces can be tricky, but there are several ways to confirm single molecule behavior. Intermittent on/off fluorescence and sudden photobleaching is one such way, as the probability for several emitters to simultaneously blink off is substantially lower than for just one molecule. Additionally, the observation of dipole emission patterns, anisotropic “wings” in the emission several hundred nanometers away from the focal plane, can often confirm a single molecule.[132, 133] Though both of these methods are not bullet-

proof, they both do provide strongly suggestive evidence of a single photon emitter.

Single molecule behavior can be easily demonstrated by one-photon excitation in spin-coated PVA films, by the two methods mentioned above as well as the more definitive antibunched photon emission.[134] In TPE, dipole emission patterns and discrete photobleaching also occur, as shown in Figure 3.9. The detected counts rates from TPE are significantly lower (~1000 counts/s) than for the same molecule excited by OPE using cw excitation, as shown for the Ag710 emitter excited by a 633nm helium-neon laser as well as a pulsed 850nm Ti-sapphire laser (Figure 3.9c). Its photostability, however, is still markedly better than the best commercially available dyes such as Cy5, with emission lasting up to 2 orders of magnitude longer when excited at the same intensity (Figure 3.9d). TPE single molecule spectroscopy is not a heavily utilized imaging technique, because the excitation intensities required to obtain detectable counts rates cause organic molecules to bleach at a cripplingly rapid rate. The Ag clusters, however, are more akin to quantum dots in their remarkable photostability and high absorption strength, allowing them to be photostable at intensities for which they can be observed down to the single molecule level.

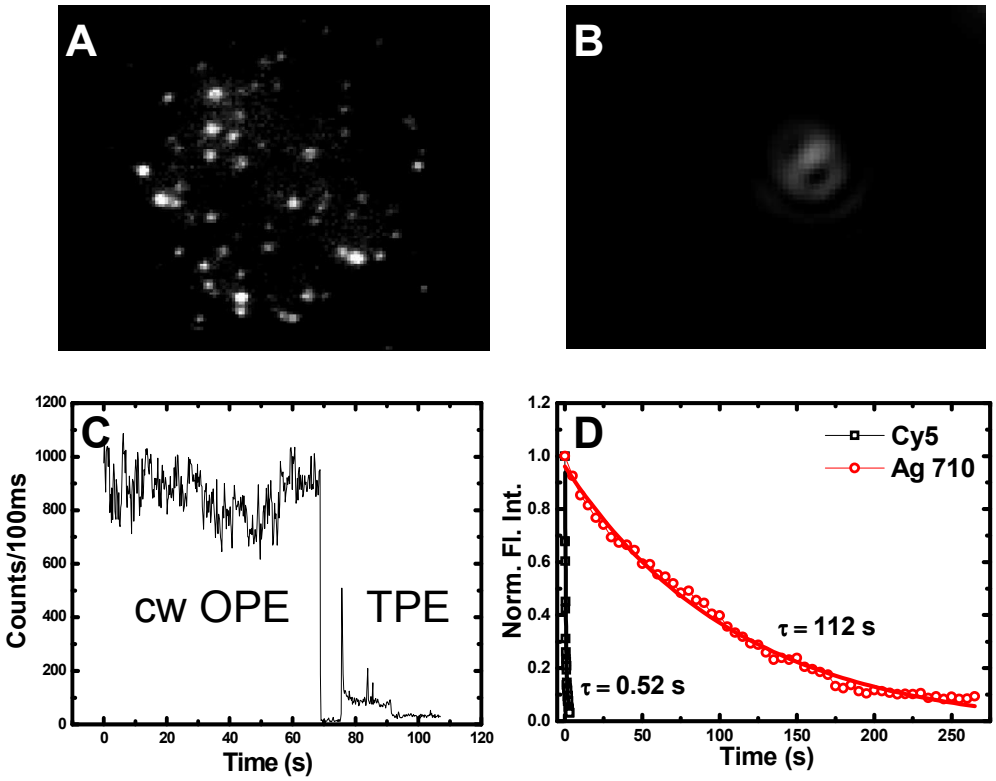

Figure 3.9 (A) CCD image of single molecules of the Ag710 embedded in a spin-coated PVA polymer film, excited by TPE at 850nm. (B) Dipole emission pattern of a single molecule, defocused onto a CCD camera. (C) Time trace of a molecule first excited by a 633nm HeNe laser, then switched to 850nm Ti-sapphire excitation. The molecule photobleached at t=94s. (D) A time trace of a collection of many molecules of Cy5 and Ag710 in PVA, excited by TPE at an average intensity of 170kW/cm^2, with 100fs, 80 Mhz pulses at 820 nm, below saturation levels for both emitters.

3.5 Conclusions

The constraints imposed by high sensitivity cellular and medical imaging, especially through tissue, has fueled efforts in developing red and near-infrared (NIR) fluorophores. Ideal for excitation and emission within the optical window from 630-1100nm, two-photon excited fluorescence offers high spatial resolution owing to its inherent quadratic intensity dependence, while also providing spectral selectivity and improved sensitivity resulting from decreased NIR absorption, scattering, and fluorescence in tissue. These Ag nanoclusters exhibit TPE cross sections in buffer far surpassing all known water-soluble fluorophores and are comparable to much larger quantum dot cross sections. With some of the largest water-soluble TPE action cross sections known, the single point of attachment, small size, and excellent one- and two-photon brightness, metal clusters hold great promise as high sensitivity biolabels.

CHAPTER IV
PHOTOINDUCED CHARGE TRANSFER

4.1 Introduction

In bulk metals, the work function (W) determines the energy necessary for photoejection of electrons residing at the Fermi energy ($W = -E_F + h\nu$).[16] As the particle size decreases to few-atom clusters, the work function also decreases due to increased surface area[135] and electronic spill out.[14] Additionally, the lack of a continuous DOS in the conduction band limits the pathways available for the electron's dissipation back to the Fermi level.[135] From the excited discrete states the electron can more easily tunnel out of potential due to the positive nuclear core of the cluster. This has been demonstrated in a series of reports by Linnert and coworkers for small silver clusters in aqueous solution.[31, 135-137] In their experiments, they successfully created distributions of small (3-7 atom) silver clusters (either neutral or partially oxidized) in an anionic polyacrylate solution. The clusters, after exposure to 308nm light, ejected an electron into the aqueous solvent, confirmed by broad absorption at 700nm, which appeared to decay on the microsecond timescale. A photoejection quantum yield of approximately 10% was observed for particles of this size, while for larger particles (n=10), the yield dropped to 2%. For even larger, metallic particles of 4nm diameter, no evidence of hydrated electrons could be found. The presence of the hydrated electron was further verified by the addition of 0.1 M acetone, for which there is a known

quenching effect. Indeed, exposure to acetone resulted in no observable excited-state absorption at 700nm. Mathies and coworkers measured the hydrated electron peak absorption cross sections, finding it to be approximately $7.1\times10^{-17}cm^2$.[138] Small silver clusters, therefore, have relatively small effective work functions, and can be made to photoeject their valence electron with UV radiation. Further, the quantum efficiency of the process seems to be heavily size-dependent, occurring in observable yields only for clusters of 10 atoms or less and peaking for the smallest clusters at about 10%. It is also believed that photoinduced charge ejection in their systems lead to further agglomeration of silver, catalyzing the reduction of free silver ions to drive its attachment to already existing clusters.[136]

4.2 Single-molecule Blinking

Typically all single-molecule fluorophores exhibit intermittent fluorescence ("blinking") due to the presence of dark states. These dark states are often disadvantageous, as precious photon information is lost during the off-states. Additionally intermittent blinking on time scales similar to the ones under investigation, such as biological binding events, or protein kinetics complicate the data interpretation. One advantage, however, arises when this dark state is photo-accessible, as this allows the photoswitching of states, enabling modulatable emission at controlled frequencies and greater signal discrepancy in high-background imaging. This technique relies on Fourier analysis of the image

series, which can discriminate signals at fixed frequencies from broadband noise and background. Intersystem crossing,[63] isomerization,[139] or even long-lived charge transfer processes[140] have been proposed to give rise to such states, yet only photoswitches exhibiting thermally-stable isomerization-based dark states have been advantageously employed.[141, 142] Ag nanodots have also shown the existence of dark-states with μs characteristic decay times,[24] but the origin of the silver cluster blinking dynamics has thus far been uncharacterized. As the photo-accessibility of these dark states has been demonstrated by repopulation of the emissive state by irradiation with a secondary laser, transient absorption studies were undertaken to spectrally and kinetically probe these states.

4.3 Transient Absorption

4.3.1 Transient Absorption Spectra

The fate and dynamics of excited-state species can best be studied by pump-probe transient absorption spectroscopy. Only about 15-30% of the excited population can be accounted for by radiative decay, and the single molecule blinking dynamics have shown the existence of microsecond dark-states, for which little can be deduced by fluorescence studies alone. Additionally, as the ground-state multiplicity of the silver clusters is unknown, no clear assignment of triplet-state population can be made as is done with most organic dyes. Therefore pump-probe absorption spectroscopy was employed to directly access these excited states in order to better understand the

photophysical mechanisms of excited-state species. Using 8 ns pulses at 10 Hz to pump the ground state, the absorption spectrum was then recorded at various time delays using a tungsten lamp passing through the sample (1 cm cuvette, quartz) overlapped with the pump and also through an unpumped region for a baseline. The curves for the Ag660 emitter are shown in Figure 4.1a, which was taken at various probe time delays. Two decaying peaks are observed, with the excited-state absorption broad and overlapped with the ground-state absorption bleach. Figure 4.1b shows only the short time spectra for all of the species studied, normalized and offset for clarity. The transient peaks are strikingly similar. The apparent shift in the absorption spectra for each species is attributed to the shifting ground-state absorption. Because the two absorption spectra overlap, each had to be fitted using the known ground-state absorption parameters to subtract its contribution from the overall spectrum. The fitting routine consisted of two Gaussian curves for each of the absorption states. The peak position and spectral width parameters were kept fixed for the ground-state absorption, and the parameters for the other curve were optimized to fit the total absorption spectrum. Figure 4.2 shows the resulting fit for the Ag660 emitter, taken at a 20 ns delay. The ground-state absorption peaks at 595 nm. After fitting, the transient absorption spectra for each species were almost indistinguishable, peaking at approximately 650 nm.

Having established that the majority of the emitters, despite their varying ground-state absorption, have essentially the same transient absorption spectrum of similarly-decaying dark-states, two questions drove subsequent

analysis. First, we wanted to pinpoint the nature of the common dark-state, and in doing so explain its lifetime and relation to the photophysical properties of silver clusters. Second, controlled repopulation of the emissive state is highly desirable for both higher emission rates in general and modulatable, frequency-domain fluorescence imaging more specifically. Therefore specific attention was paid to the efficiency of the transient absorption with respect to the molecular emission rate. Throughout the study bulk transient measurements were complimented by single molecule fluorescence studies, as insight gained by one source was used to better understand the results of the other.

As has been shown earlier, the encapsulating matrix plays a large role in the resulting photophysics of silver clusters, and its effect intensifies as the cluster size is decreased. Considering silver clusters are known to photoeject electrons with reasonable quantum yields at this size, and that cytosine plays a key role in the stabilization of the clusters, the transient absorption spectrum is proposed to be from anionic cytosine resulting from the photoinduced charge transfer (PICT) of the embedded silver clusters. The absorption spectrum closely overlaps with both the electron affinity measurements of gas-phase anionic cytosine and the absorption of the charge-transfer state of pyrene-uracil coupled-pairs. In the gas-phase studies, the addition of water clusters to the nucleotide broadened and red-shifted the electron affinity, eventually leading to its peak

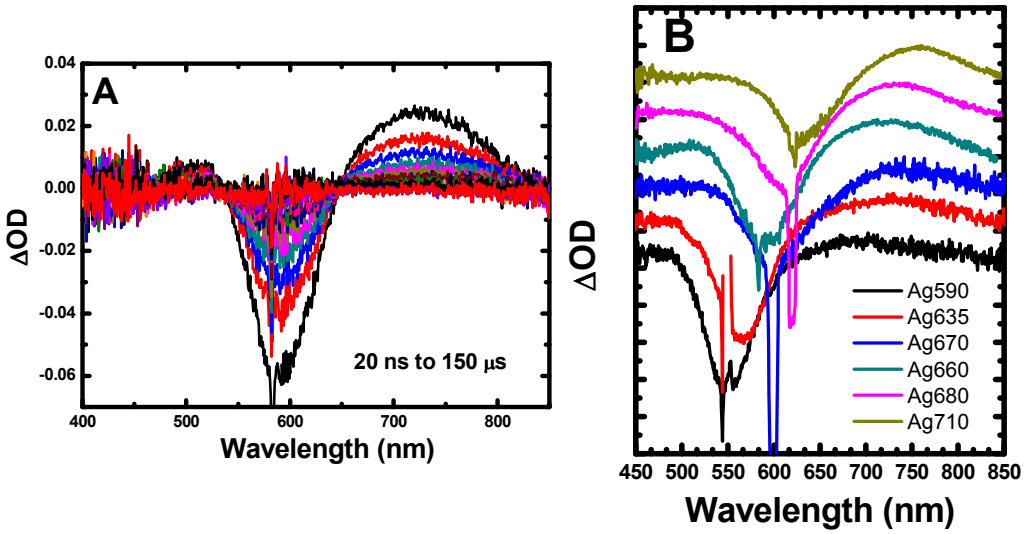

Figure 4.1. (A) The nanosecond transient absorption spectra of the Ag660 species (pump at 595 nm) taken af various time delays. The initial curve is at a 20 ns delay, while each decaying spectrum is in 10 μs intervals up to 150 μs. (B) Nanosecond transient absorption spectra of a series of silver clusters, labeled by the maximum emission wavelength. The curves are offset for clarity.

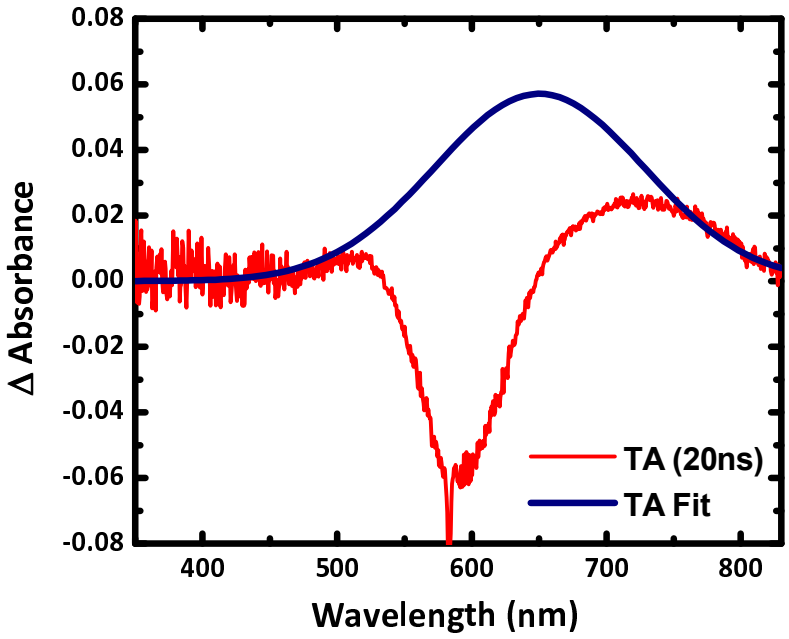

Figure 4.2 The transient absorption and spectral fit of the Ag660 emitter, which was fitted to the 20ns delay absorption curve, revealing a broad peak centered at 650nm. The fit was performed by fitting two Gaussian peaks, one of which was constrained by the known ground-state absorption width (84 nm FWHM) and peak position (595nm). The resulting fit of the transient peak is shown here.

around 700 nm.[90] Additionally, the nucleotides cytosine, thymine, uracil, and adenine produced spectra closely resembling one another, and they all peaked to within 20nm of one another. The transient absorption of PICT of pyrene-uracil produces a similar peak at 640nm, appearing as a result of anionic uracil population and excited-state pyrene decay.[93] The difference in energy between the two results can best be explained by the different solvent environments and the covalently-coupled pyrene chromophore. Although not directly conjugated to the nucleotide, the system is partially coupled and therefore a shift in absorption energies for the ground and excited states is expected. Additionally, Koopman's theorem is employed in the calculation of the electron affinities, which states that the energy required to eject an electron from an anionic molecule is equal to the negative of the LUMO energy level. In that theorem is the implicit assumption that the total electronic wavefunction of the molecule is the same for the neutral and anionic species.[143] Whether this assumption is valid for these systems is not clear, and may perturb those values slightly. The silver-oligonucleotide PICT peak, however, falls in between the reported values for the two systems, and as such the mechanism is considered to be consistent with the experimental data.

4.3.2 Absorption Cross Sections

The absorption data can also be used to determine the excited-state absorption cross section for each of these species. Using the ground-state depletion to normalize for excited-state population, the absorbance difference measured by transient absorption can be used to measure is strength. The

absorption cross section was measured by the singlet depletion method, given by the following relations:[144]

$$\Delta OD_{GS} = -\varepsilon_{GS}[CT]l \quad (4.1)$$

$$\Delta OD_{CT} = \varepsilon_{CT}[CT]l \quad (4.2)$$

in which ε's are the molar absorptivities of the ground and CT states, [CT] is the population of the CT state, and *l* is the cell path length. It is assumed that all molecules excited into the first excited-state either return to the ground state or populate the CT state at t = 60ns, which is the time slice that was used. Additionally, because the ground-state and transient absorption spectra overlap, the isosbestic point was used to add the constraint $\varepsilon_{CT}(\lambda_c) = \varepsilon_{GS}(\lambda_c)$, in which λ_c is the isosbestic point in the transient spectrum. Thus the molar absorptivity of the CT state can be calculated by the ratio of the ΔOD from the ground-state depletion and CT population. For the Ag660 emitter, the isosbestic point occurs at 648 nm, at which the ground-state extinction coefficient has the value $1.5\times10^{5} M^{-1}cm^{-1}$,[84] equal to the CT extinction coefficient at the same wavelength. The peak CT extinction coefficient was then determined to be $1.5\times10^{5} M^{-1}cm^{-1}$ (absorption cross section of $5.8\times10^{-16} cm^{2}$) at 650nm, based on the transient absorption curve fitting. Similarly, the isosbestic points of the transient spectra from other species were used to measure their cross sections.

Further evidence suggestive of excited-state CT can be found by examining the transient absorption spectra of the Ag660 species in the oxidized form. Oxidation of the species can occur by exposing a fully reduced sample to air for several weeks, resulting in a blue-shifted absorption emission curve. The

oxidized emission of the Ag660 species peaks at 540 nm, and this can be converted back to the fully reduced species by the further addition of $NaBH_4$. Two samples of the Ag660 species were compared, one in the fully reduced state and one which has been oxidized over time. The oxidized sample is expected to have significantly less charge transfer because (1) the positive cluster has significantly lower electron spill-out and (2) decreased electron density increases the oxidation potential, making it more energetically costly for transfer to occur. Indeed comparing the transient absorption spectra of the two samples it can be seen that while both the ground-state depletion and transient population occur with the fully reduced sample, the oxidized sample shows an insignificant occurrence of either process. The sample shows strong ground-state absorption and emission on the order of that observed for the fully reduced species, indicating that there is significant absorption at the wavelength used to pump it (OD = 1.8 at 500nm). The lack of ground-state depletion, therefore, is likely due to the inability of the oxidized cluster species to transfer charge to the oligonucleotide.

4.3.3 Lifetimes

The decay of the Ag660 transient absorption spectra was probed by time-dependent transient absorption measurements. It was fitted bi-exponentially to 10 μs (35%) and 40 μs (65%) components (Figure 4.3), measured at 800 nm. The ground-state bleach rise time at 590 nm roughly corresponds to the decay values, confirming that the charge transfer state is populated by the ground-state

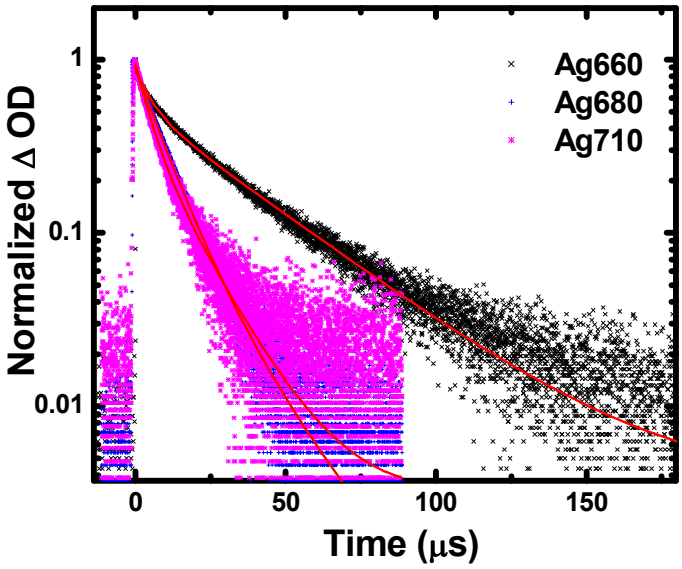

Figure 4.3. Transient absorption change as a function of time delay after pump pulse for the near-IR species, plotted in a semi-log scale. The decay were recorded at 800nm using a photodiode response recorded by an oscilloscope, whose instrument response time was 10 ns. The decay was fitted bi-exponentially for each emitter, and whose results are shown in Table 4.1

depletion. The bi-exponential behavior is ubiquitous among all the species showing transient absorption, although the numbers themselves vary slightly. As indicated previously, the broad, red-shifted electron detachment spectra of anionic cytosine is suggestive of a dipole-bound anion, wherein the anion is only loosely associated with the molecule. Because the system discussed here is a 12mer ss-DNA strand, further charge delocalization along the strand is expected, possibly accounting for the long microsecond decay times. Additionally, delocalization across such a complex system may take on several configurations, accounting for the multiple exponentials. These configurations may be a result of the spatial flexibility of the DNA strand, which is expected to significantly affect the coupling among nucleotides and hence the stability of a surplus charge. Multiple decay time components due to conformational flexibility, however, would suggest that a continuous distribution of decay time and therefore a stretched exponential fitting would be more appropriate. The data presented here was not specifically fitted in this manner, although it is advisable for future studies to be mindful of the assumptions in this kinetic model.

Classical methods of confirming intramolecular PICT include measuring the recombination decay lifetimes in a variety of solvents, as dielectric stabilization of the solvent is expected to shift the energy level of the charge-separated state in reference to the neutral ground-state. These experiments are potentially more difficult to interpret for the DNA-containing systems, as the solubility of DNA is limited and its confirmation may be drastically affected by the solvent environment. Initial tests using methanol and acetonitrile as solvents

(95% by volume, 5% water), however, showed no observable difference in decay lifetime, suggesting that the introduction of new solvents had little to no effect on the recombination rate. Further studies are needed, however, to make more reasonable conclusions based on this data.

Small amounts of acetone are known to quench the photoinduced hydrated electron states of silver clusters in solution. The spectral detection of these hydrated electrons has been reported to disappear in the presence of small portions (50 mM) of acetone in aqueous environments. A similar test was carried out for the present system, with 500 mM acetone added, resulting in no effect of the lifetime on its presence (Figure 4.4). Additionally, the triplet states of most organic dyes can be quenched with small amounts of molecular oxygen in the solution. Triplet-states in the microsecond time range are easily quenched with molecular oxygen, so the study of these states usually requires thorough degassing. Molecular oxygen has a triplet ground-state configuration, allowing it to exchange spins with the triplet state of organic dyes. Again, aeration levels of the silver nanocluster solutions had no discernable effect on the decay lifetimes (Figure 4.4). These results are consistent with a charge-separated state contained within the silver-DNA system, well-protected from environmental influence.

The rise-time dynamics of charge separation were instrument-response limited (~10 ns) in the nanosecond transient absorption experiments, indicating a significantly faster charge separation process. Femtosecond transient absorption was therefore employed to probe dynamics at faster time scales. These

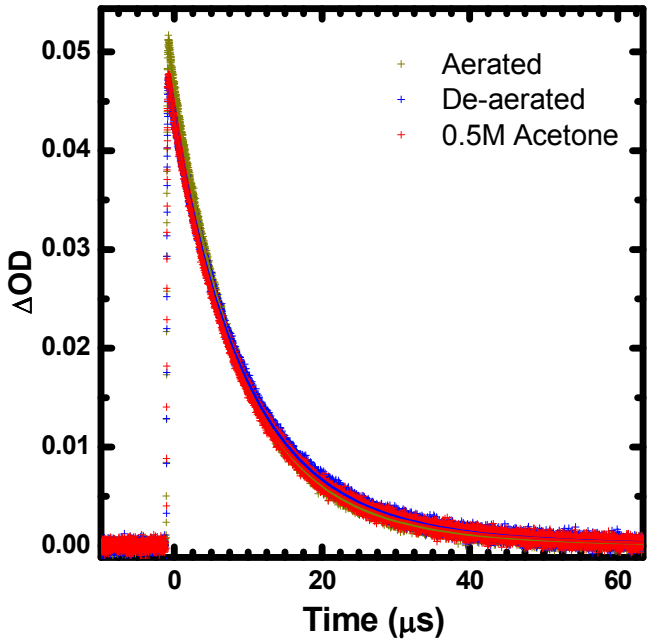

Figure 4.4 Transient absorption change as a function of time delay after pump pulse for the Ag660 species in various aqueous environments. The original solution (aerated) was degassed by N_2 for 20 minutes before taking the (de-aerated) decay. The solution, after exposure to air, was then mixed with 0.5 M acetone and the measurement was repeated. The decay was recorded at 800nm using a photodiode response, whose instrument response time was 10 ns, and the curves were fitted bi-exponentially.

experiments, much in the same way as the nanosecond transient experiments, recorded the absorption spectra using a broadband probe signal at varying times after the initial excitation (~100 fs pulse). The data produced a two-dimensional matrix of spectral and temporal information, from which specific slices in either axis could be extracted and analyzed. The instrument ranged temporally from the pulse width of the laser to approximately 3 nanoseconds. Additionally, several corrections had to be performed on the data before any analysis was done. Laser scatter from the sample produced anomalous peaks at the laser wavelength, and these peaks were subtracted out from the entire data set based on the average spectrum at times before laser excitation. Laser chirp correction was also needed for the short time scale (several hundred femtoseconds) of the data to compensate for the chirp of the laser. This was achieved by generating a reference file from the instantaneous scatter of chloroform. The data was then deconvoluted by this reference file, resulting in the final corrected data set. Both of these operations were performed by the instrument data collection software.

Three species, the Ag660, Ag680, and Ag710 emitters were analyzed. The spectrum at various time delays is shown in Figure 4.5, along with the long-time spectra from the nanosecond absorption. All of the spectra are remarkably similar, at all the time scales indicated. They have been scaled and normalized at the low energy side of the transient peak. Although they are remarkably similar, the faster time spectra are somewhat blue-shifted with respect to the 20 ns spectrum. This may suggest a relaxation process, as higher energy absorption would be required upon energetic relaxation to another state. The

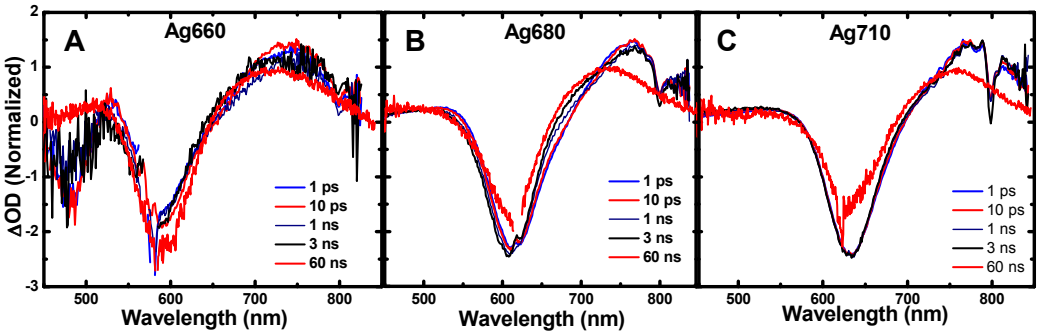

Figure 4.5 (A-C) Femtosecond and nanosecond transient absorption spectra (normalized) of a series of silver clusters, labeled by the maximum emission wavelength. All of the species were excited by 100 fs pulsed excitation, except for the long delay time curve, which was generated from excitation by a 7ns pulsed laser. The dip in the spectrum around 800 nm is an instrumental artifact resulting from the white-light generation used as the probe. (D) The transient absorption and spectral fit of the Ag660 emitter, which was fitted to the 20ns delay absorption curve, revealing a broad peak centered at 650nm.

fastest time point shown in the figure is at a 1 ps delay, which is approximately the point at which the excited-state population has peaked and is beginning to decay to the ground-state. The kinetics, taken at the ground and excited states, respectively, are shown in Figure 4.6. Because the ground-state and excited-state absorption bands are overlapped, the extraction of individual kinetics is difficult to make, especially for the bleach band as that is contained entirely within the excited-state positive band. To account for this, the kinetics at the two ends of the transient spectrum were compared with another and found to be virtually identical. Then it was assumed that the kinetic contribution of the excited-state at the ground-state bleach wavelengths can be subtracted out, because the kinetics at the end of the spectrum is known. It is assumed that the kinetics of the excited-state is constant throughout the peak. Before subtraction, however, the magnitude of the absorbance change is calibrated to what is expected at the ground-state wavelength, based on the spectral transient fit of Figure 4.2.

The absorption kinetics reveal multiple pathways of ground-state repopulation, as intimated by the various decay time scales. After the instrument-response limited depopulation (130 fs), the ground-state bleach recovers at 500 fs (k_{30} = 2x10^{12} s^{-1}), ~2 ns (k_{20} = 5x10^{8} s^{-1}), and at 10-40 μs (k_{40} = 5x10^{4} s^{-1}). Each result from decay from a different excited-state following excitation. The amplitude of the decay can be measured by the ratio of the ΔOD at the peak and the base, indicating that the initial repopulation accounts for approximately ~25% of the excited-state, which non-radiatively decays back to the ground state. The kinetics of the transient absorption show a rise time of 330 fs, indicating that

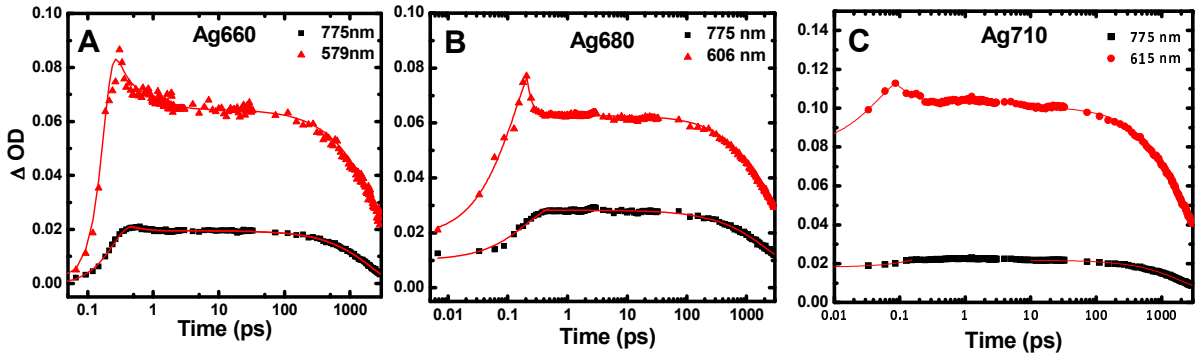

Figure 4.6 Femtosecond transient absorption kinetic traces plotted in a semi-log plot. The wavelengths shown for each emitter reflect the transient absorption (black) and the ground-state depletion (red). The depletion shown appears at negative ΔOD, but is plotted in its absolute value. It has been corrected for spectral overlap by subtracting out the contribution from the transient absorption, which is based on the kinetics at 775 nm calibrated to the expected value based on the peak curve fittings. The data was collected by exciting with a 100 fs Ti-sapphire laser at 1 kHz, then probing with a white-light continuum generated from the same laser. The excitation wavelength was tuned to the peak of the ground-state absorption for each emitter.

charge transfer takes place with k_{10} = 2.9x10^{12} s^{-1}, before vibrational relaxation can occur. Additionally, a decay process is observed on the 1 to 3 ns range, suggesting relaxation from the radiative state. This occurs with the majority of the excited-state amplitude. Since non-radiative decay occurs at approximately 2x10^{12} s^{-1}, direct competition cannot be occurring between radiative and non-radiative relaxation as otherwise no emission at 3 ns would be observable. It is therefore proposed that non-radiative relaxation occurs through a charge-transfer state (with ~25% yield) accessed by the initial excited-state, which also decays into the radiative state (with ~75% yield). In this model (Figure 4.7) no direct competition occurs between these two decay processes, allowing both fast transition into the charge-transfer state and high quantum yield emission. The radiative state, therefore, is expected to be of similar energy as the CT state, explaining the indistinguishable transient absorption spectra. Accidental degeneracy could account for this, and many reports have been made in which singlet and triplet states occupying similar energy levels produce indistinguishable absorption spectra. The growth of the transient band at 350 fs is therefore independent of the non-radiative decay of the bleach at 500 fs, as the transient band may be a result of absorption from the radiative state as well as the charge-transfer state. Nanosecond transient spectra indicate that another much longer-lived charge-transfer state is populated, presumably through a transition mediated by the initial fast charge transfer. The time constants extracted from the kinetic curve fits are shown in Table 2. A more likely model

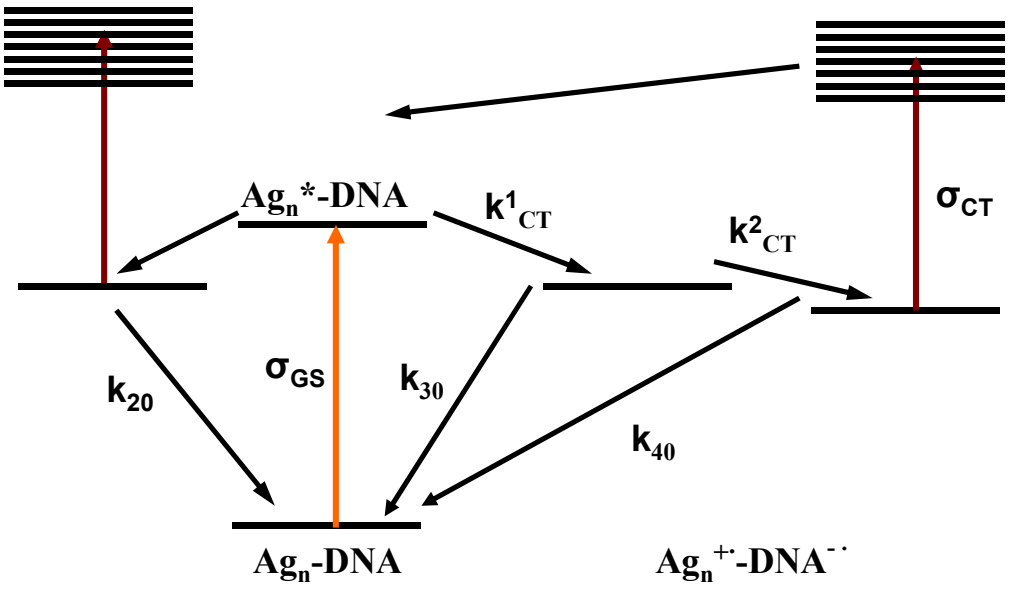

Figure 4.7 Energy diagram of the photoinduced charge transfer scheme. Energy values listed for the transitions were taken from ground-state and transient absorption spectra. The Ag_n-DNA complex is initially excited to the excited state of the silver cluster, from which either a decay to the radiative state or the transition to the charge-transfer (CT) state occurs. The CT state can then either relax non-radiatively back to the ground state or transition into a longer-lived CT state, from which photo-assisted reverse charge transfer can occur.

***Table 4.1*. Excited-state Photophysical Properties**

	Abs(nm)	σ^{RCT} ($10^{-16}cm^2$)[a]	τ_1^{CT} (μs)	τ_2^{CT} (μs)	τ_{wt}^{CT} (μs)[b]	τ^{CT} (μs)[c]	ϕ_{CT} (TA)[d]	ϕ_{CT} (FCS)[e]
Ag660	595	5.8	10 (35%)	40 (65%)	19.5	31.1	0.746	0.008
Ag680	620	7.3	8.4 (84%)	20 (16%)	9.3	13.1	0.810	0.012
Ag710	633	4.2	4.7 (13%)	10 (87%)	8.7	16.3	0.86	0.004

[a]Absorption cross sections were measured by nanosecond transient absorption, described in ref. 22.
[b]The average decays from the transient absorption were calculated by taking the weighted inverse average of the two components $\frac{1}{\tau_{wt}} = \left(\frac{A_1}{A_1 + A_2}\right)\left(\frac{1}{\tau_1}\right) + \left(\frac{A_2}{A_1 + A_2}\right)\left(\frac{1}{\tau_2}\right)$

[c]The decay as measured by single-molecule correlation spectroscopy. The value was corrected for excited-state depopulation due to the excitation laser by extrapolating the intensity-dependent value to zero excitation intensity.
[d]Determined by femtosecond transient absorption measurements
[e]Measured by single-molecule correlation spectroscopy, in which k_{CT}

as reflected in the transient kinetics is that charge separation competes with relaxation to the emissive state rather that emission itself.

4.4 Saturation from Dark-state Population

Single molecule photon counting experiments have revealed the existence of a long-lived dark state from which no emission is observed. All species believed to be fully reduced exhibit similar dark-state dynamics. The “off” times fall within the 5 to 30 microsecond time range, significantly longer than the 2-4 ns radiative lifetime of the first excited state. Additionally, the single molecule experiments have shown that the quantum yield for populating this state from the first excited state is approximately 1%, determined by fitting the relative on and off times of a single molecule time trace. The long lifetime of this state introduces an effective trap for the normal 2-state excitation cycle, resulting in lower emission rates and premature excitation saturation, akin to the triplet states of organic chromophores. Although dark-state population is seen and can be characterized for cw-OPE, pulsed TPE can also populate this state and provides the additional flexibility of pulse frequency control. Once the molecule enters the dark state, it is rendered non-emissive until relaxation back to the ground state. Operating at 80 MHz (12.5 ns between pulses), a 10 μs lifetime would leave the next 1000 pulses that arrive transparent to the molecule. At 8 kHz (125 μs between pulses), however, the vast majority of the molecules have returned to the ground state before the arrival of the next pulse. It is for this reason that the TPA cross section was measured using 8 kHz pulses.

Pulse repetition rates are therefore crucial for the observed saturation of particular transitions and are dependent on the lifetimes of those states. This is not the same saturation that occurs when, at high excitation intensities, nearly all the molecules are excited at every pulse. That saturation is a function of the absorption cross section, while the repetition rate saturation is strictly a function of lifetime. The saturation of the dark state can be seen by plotting the fluorescence intensity as a function of peak excitation intensity for a series of different repetition rates, shown in Figure 4.8a for the Ag710 emitter. At 8 kHz the purely quadratic behavior expected for TPA is observed. As the repetition rate is increased up to 40 MHz, the curves become sub-quadratic and saturation arises at 800 kHz (corresponding to 1.25 μs). At low repetition rates, deviation from quadratic behavior is seen at high peak excitation intensities, corresponding to the emerging saturation of the 2-4ns emissive state.

An interesting effect, however, was noted when taking the TPE spectra of the near-IR emitters at various repetition rates. As noted before, TPA cross sections and excitation spectra were recorded at 8 kHz to ensure ground-state repopulation. At higher repetition rates, however, the excitation spectra shifted, as can be seen in Figure 4.8b-d. The dependence of emission intensity on the excitation wavelength for high repetition rate excitation reflects both initial TPA but also excited-state absorption. Excitation spectra, unlike absorption, measures emitted photons as a result of absorption. A change in the excitation spectra suggests that by increasing the repetition rate beyond the excited-state decay rate, emission at the same wavelength also occurs by a path other than

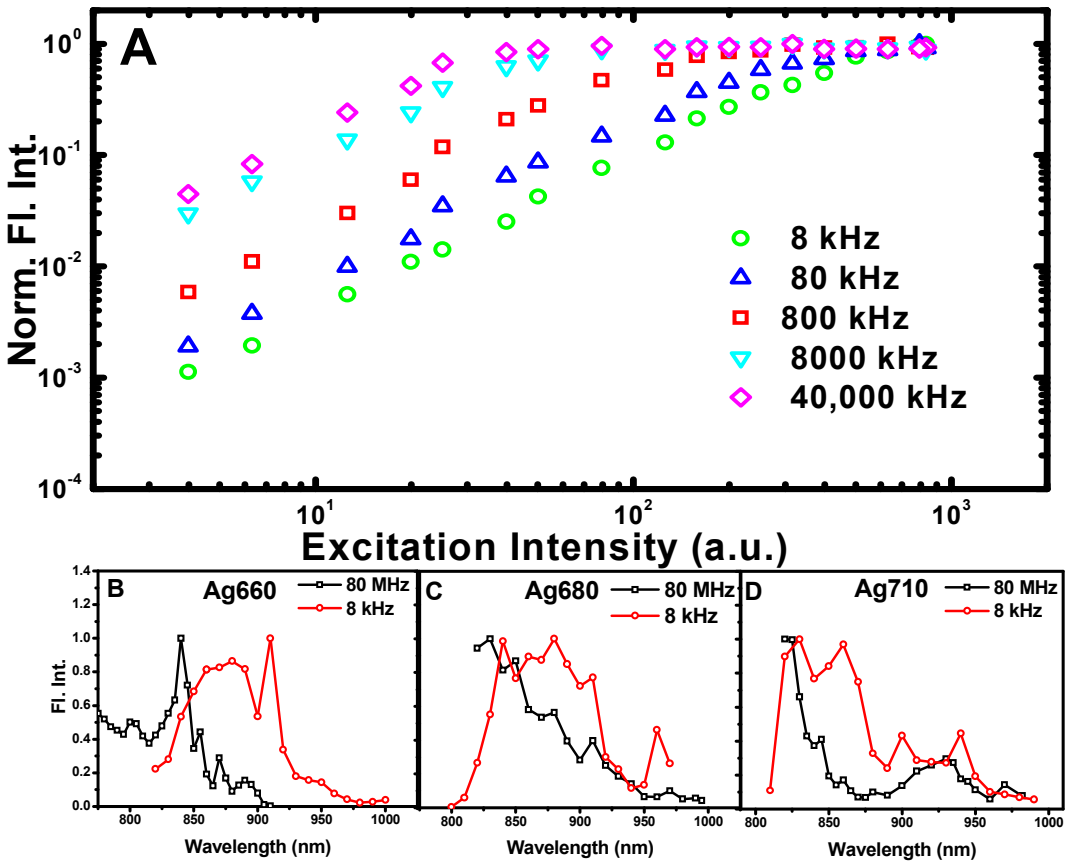

Figure 4.8 (A) The peak excitation intensity dependence of the Ag660 emitter when excited at 850nm, taken at a series of excitation repetition rates. At 8kHz no saturation, with purely quadratic behavior, is observed, while for higher rates there is premature saturation of the fluorescence signal. (B-D) TPE spectra of the near-IR species excited at two excitation rates, 80Mhz and 8kHz. Emission was collected at the same wavelength range and peak excitation intensity was constant for both spectra. Each curve was normalized to its maximum value.

directly from the emissive state. More specifically, it suggests that excitation from the dark state repopulates the emissive state faster than it would by its natural decay. The high repetition rate spectra, however, peak outside the range of this experiment, which is limited by spectral filters necessary to separate out the emission bands from the laser frequency. It is evident, though, that the peak occurs at energies lower than the TPA excitation spectra.

4.5 Single-molecule Analysis

In addition to bulk transient absorption measurements, single molecule blinking dynamics can be used to calculate the charge-transfer kinetic rate constants, absorption cross sections, and quantum yields. As discussed in chapter 3, fluorescence correlation spectroscopy (FCS) is a powerful single molecule tool which can yield many useful values without having to specifically isolate single molecules. Previously, however, only the diffusion of molecules in and out of the focal volume was considered. Here analyses on fast time scales corresponding to observed dynamics on the microsecond time scale were performed. According to the transient absorption results, these times scales correlate to the long-lived charge-transfer state, from which the molecule eventually returns to the ground-state. As the molecule diffuses through the detection volume, which is slower (~100 μs to ~1 ms) than the targeted charge-transfer lifetime, the molecules are allowed to decay and re-excite multiple times.

This results in an exponential decay of the autocorrelation function at the expected time region, described by,[127, 128, 145]

$$G(\tau) = 1 + \frac{F_{DS}}{1 - F_{DS}} \exp(-\tau / \tau_{ac}) \tag{4.3}$$

in which F_{DS} is the steady-state dark-state fraction,[128] and τ_{ac} is the autocorrelation time decay constant. The correlation time and dark-state fraction are both functions of the "on" and "off" times of the molecule, expressed by the relations,[63, 128]

$$1/\tau_{AC} = 1/\tau_{on} + 1/\tau_{\text{off}} \tag{4.4}$$

$$\tau_{on}/\tau_{\text{off}} = (1 - F_{DS})/F_{DS} \tag{4.5}$$

The "on" time refers to the mean time a molecule remains in an emissive state (either the ground state or the emissive excited state), while the "off" time is the mean time it resides in a dark state, yielding no emission. In this case, the off-times refer to the charge-transfer lifetime (τ_{CT}), which was extracted using the exponentially-fitted autocorrelation times and F_{DS} by the following relation,[128]

$$k_D = \frac{1}{\tau_{AC}}(1 - F_{DS}) \tag{4.6}$$

in which k_D is the observed decay rate constant of the CT state. Because the CT state absorption overlaps with the ground-state absorption for the majority of the emitters studied, the observed decay rate is a combination of the natural decay rate ($k_D^{'}$) and the depopulation due to excited-state absorption, showing in the following equation,[128]

$$k_D = k_D^{'} + \sigma_{CT}\gamma_{ex}I_{ex} \tag{4.7}$$

in which σ_{CT} is the charge-transfer state absorption cross section, γ_{ex} is the reciprocal excitation photon energy, and I_{ex} is the excitation irradiance. Time traces at several excitation intensities were measured, shown in Figure 4.9, and the autocorrelation curves were fitted to extract the time constant in each case.[146] The natural decay rate constant was determined by extrapolation of the linear-fit to zero intensity (Figure 4.10). The slope of the fit was used to extract the excited-state absorption cross sections. Both the decay rate constant and absorption cross section were compared with the values obtained using bulk transient absorption, which is taken as the natural decay rate constant as no observable pump energy dependence is found. As single molecule intensity correlation analysis inversely convolutes all closely-spaced "off" times and models them as a single component, a weighted average of the bi-exponential decay components of transient absorption was used to compare the two values, using the following weighting equation,

$$\frac{1}{\tau_{wt}} = \left(\frac{A_1}{A_1 + A_2}\right)\left(\frac{1}{\tau_1}\right) + \left(\frac{A_2}{A_1 + A_2}\right)\left(\frac{1}{\tau_2}\right) \tag{4.8}$$

in which the amplitudes and time constants are given by the bi-exponential fitting equation, $F(t) = A_1 e^{(-t/\tau_1)} + A_2 e^{(-t/\tau_2)}$. For the Ag660 species, the natural decay time constant from FCS (31.1 μs) was found to be slightly larger than that obtained from transient absorption (19.5 μs). Collisional quenching in the high concentration samples used for transient absorption may account for the slightly shorter lifetimes, compared with the highly dilute single molecule studies. Longer

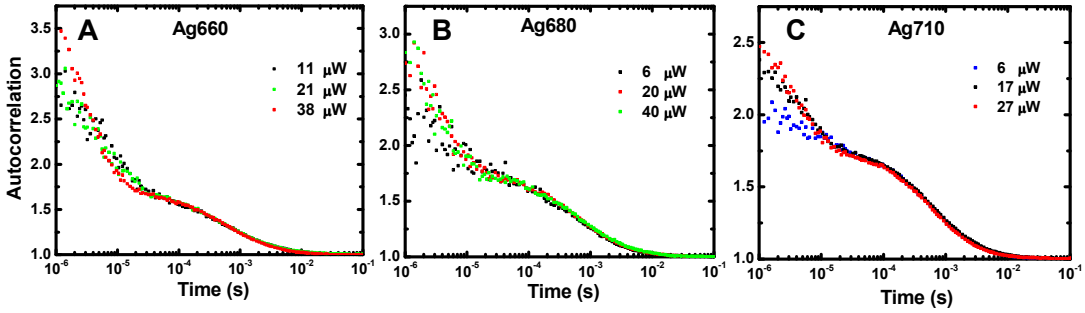

Figure 4.9. (A-C) Fluorescence correlation spectroscopy time trace autocorrelations for the three Ag nanodots. The species were excited (594nm, 633nm HeNe) by a focused laser (40x water objective, 1.2 NA) at the specified powers, and time traces were collected by an avalanche photodiode through a 50μm optical fiber. Two decay components were fitted, the longer time scale corresponding to diffusion through the laser focus, while the shorter time decay was attributed to the charge separated dark state.

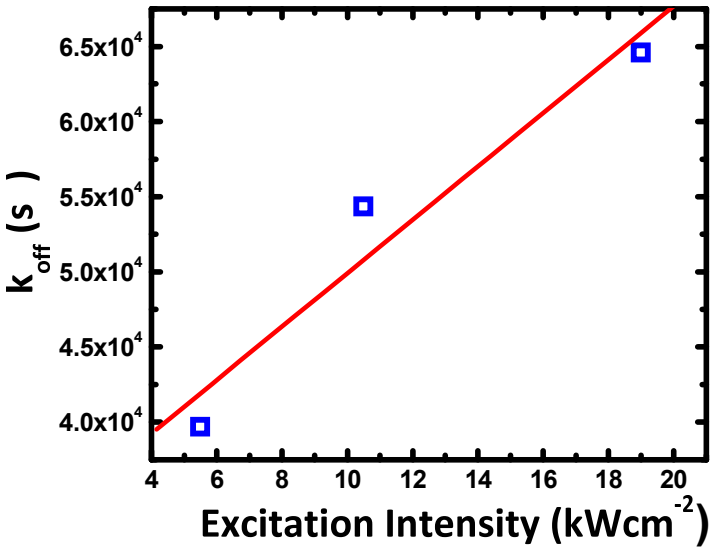

Figure 4.10. The measured off rates (inverse of off-time) for the Ag660 emitter at various excitation intensities in the fluorescence correlation spectroscopy experiment. Calculation of the off times were done by measurement of the decay time and amplitude of the autocorrelation function, as described in the text. The intensity dependence of the decay rate indicates that photoinduced depopulation is occuring as well, with the value at the y-intercept reflecting the natural decay rate. The slop of the line was used to measure the action cross section of this photoabsorption.

off-times were observed for Ag nanodots immobilized in a PVA film,[24] which may result from the reduction of recombination channels due to the more restricted conformational flexibility of the DNA when embedded in a film. The rate of charge transfer (k_{CT}) can also be calculated using the single molecule autocorrelation times measured with FCS. The value is given by the following,[128]

$$k_{CT} = \frac{F_{DS}}{\tau_{AC}}\left(1 + \frac{k_{30}}{k_{01}}\right) \tag{4.9}$$

in which k_{01} is the ground-state excitation rate, calculated from the excitation intensity (I_{ex}) and ground-state absorption cross section (σ_{GS}) by $k_{01} = \sigma_{GS}\gamma_{ex}I_{ex}$. The non-radiative decay rate (k_{30}) was used in place of the normally-used radiative rate, because according the proposed model, population of the long-lived CT state competes with non-radiative decay (3-0) rather than fluorescence. According to the calculation, the charge transfer rate constant measured for the Ag660 emitter was $3.36\times10^{10}\ s^{-1}$ based on an excitation rate of $2.21\times10^{7}\ s^{-1}$. The quantum yield of CT was then calculated based on the decay competition by $\phi_{CT} = k_{CT} / \ (k_{CT} + k_{30})$. The value obtained, 0.017, reflects the probability of transitioning from the initial CT state to the final CT state assuming that the 25% non-radiative decay is fast recombination from that state. The total calculated quantum yield therefore is 1.7% of 25% or ~0.4%. For all three near-IR emitters, quantum yields ranging between 0.2 to 0.6% were measured. As this quantum yield value reflects the overall probability of populating the microsecond states from initial excitation, it suggests that the vast majority of the initial CT population

Table 4.2. Femtosecond Transient Absorption Kinetics

	τ_{01}^{GS} (ps)	τ_{30}^{CT} (ps)	τ_{13}^{CT}(ps) rise	τ_{20}^{GS}(ps)	τ_{20}^{CT}(ps)
Ag660	0.13 ± 0.032	0.50 ±0.052	0.35 ±0.052	2140 ± 78	2100 ± 180
Ag680	0.14 ± 0.047	0.38 ± 0.013	0.21 ±0.043	1750 ± 25	1860 ± 100
Ag710	0.19 ± 0.020	0.34 ± 0.010	0.32 ±0.065	2240 ± 69	2320 ± 120

quickly recombines back to the ground state, as confirmed by the fs bleach recovery.

4.6 Charge Transfer Energetics

Photoinduced charge transfer requires the energy absorbed by the photon to facilitate electron transfer. Molecules in the ground state will typically not have enough energy to overcome the energetic barrier described by the oxidation and reduction potentials of the donor and acceptor, respectively. The Rehm-Weller equation can be used to calculate the driving force of PICT, given by,[119]

$$\Delta G = E_{D+/D} - E_{A/A-} - E_{GS} - \frac{e^2}{\varepsilon d} \qquad (4.10)$$

in which $E_{D+/D}$ is the reduction potential of the donor, $E_{A/A-}$ is the reduction potential of the acceptor, E_{GS} is the 0-0 ground-state absorption energy, and the last term is the Coulombic attraction energy experienced by the ion pair after charge transfer. The standard reduction potential of polycytosine (C_9) has been reported to be -1.6 V.[147] Henglein et al. has reported the standard reduction potentials of silver clusters as a function of size (n = 1, 2, 3, 5).[31] Specific assignments to clusters sizes have not been made, but taking the average excitation energy (2.2 eV), the driving forces are found to be 0.5 eV, -0.2 eV, and 0.3 eV, for n = 2, 3, and 5. It's clear without cluster assignments calculating accurate driving forces is difficult, due to the negative value observed for n=3, but

excitation energies are in the range for the most part to provide sufficient energy for charge transfer to occur.

The multiple charge recombination timescales observed suggest a variety of states and recombination mechanisms. Initial recombination (25%) occurs with high efficiency (95-97%) within several hundred femtoseconds, but a much longer-lived state must be occupied for the remaining population. The ratio of charge injection (k_{CT})and recombination (k_{40}) rate constants is approximately $6\times10^{8}s^{-1}$. The longer lived charge transfer state of ~1% of the population may be explained by the dynamics of the charged DNA. As charge transfer is exponentially distance-dependent, charge migration along the length of DNA could result in significantly depressed recombination rates.[148] The rate constant is proportional to the distance between donor and acceptor ($k_{CT} \propto \exp[-\beta(d-d_0)]$)[60] for which β is an orbital parameter term (which depends highly on the medium through which charge transfer occurs) that has been empirically estimated to be ≤ 0.5 for DNA.[149] Assuming that β is 0.5 and the distance of forward and reverse charge transfer is 2.7 Å (the hydrogen bond length of DNA base pairs) and ~40 Å (the length of 12-mer DNA, assuming no coiling or condensation[149]), the ratio of the rate constants is expected to be approximately 1.1×10^{8}. As no reliable structural data of the oligonucleotide-encapsulated silver nanodots exists, the charge transfer distances may vary, but the expected k_{CT}/k_{RCT} ratio is within the same order of magnitude as that measured by transient absorption. Additionally, the driving forces calculated in the preceding paragraphs suggest that although the forward photoinduced driving forces are quite small (ΔG ≤ 0.5 eV), the

reverse direction has a significantly larger driving force (ΔG ~1-2 eV). Large driving forces for recombination have often been attributed in a variety of systems to Marcus inverted region effects, resulting in significantly slower recombination rates compared to the initial charge separation.[150-153]

4.7 Optical Limiting

Optical limiting is an optical effect wherein the transmission of the sample becomes lower at a particular wavelength as a function of increasing light intensity. This effect has far reaching applications as light-protective materials, for which light at safe intensities is transmitted but blocked at levels potentially damaging to eyes.[154-158] Typically in the low energy regime the transmission is constant, and is strictly a function of concentration, the coefficient of absorption, and path length, according to Beer's law ($A = \varepsilon c l$).[44] For two level systems, saturation eventually sets in at higher energies, causing the transmission to increase because of induced transparency. Saturation may be achieved either due to the finite absorption cross section of the transition or the radiation rate from the excited state, depending whether irradiation is continuous or pulsed. For 3 or 4 level systems however, in which there is either an excited-state absorption or transition to another, longer-lived excited state from which absorption occurs, the introduction of pathways to depopulate the ground-state transition facilitate the tuning of the overall transmission as a function light intensity. The photophysical mechanism by which optical limiting occurs is

generally referred to as reverse saturable absorption, which as the name indicates, is predicated on the reverse saturation of the ground-state transition. For a 4 level system in which the initial excited state decays to a triplet state with quantum yield ϕ_{ISC}, which can subsequently be excited with cross section σ_{CT}, the necessary reverse saturable absorption (RSA) necessary for optimal limiting can be described the expression,[155]

$$\phi_{ISC}\sigma_{CT} \Big/ \sigma_{GS} > 1 \qquad (4.11)$$

assuming that the rise time of the "triplet" state is faster than the laser pulse width. Another important parameter in the efficacy of a particular RSA system as an optical limiter is the time scale on which the excited-state transitions occur. Applications can range from femtosecond-pulsed to continuous-wave limiting, and so materials whose excited-states can remain populated on particular times scales will be useful for limiting at those times.[159]

The strong, broad transient absorption of the silver nanocluster charge-transfer state, whose maximum (650 nm) is at an energy shifted from the ground-state absorption of most of the emitters. For the Ag660 species, the excited-state cross section has a maximum of $5.8\times10^{-16} cm^2$, while the ground-state transition peaks at $1.3\times10^{-15} cm^2$. Beyond approximately 645 nm, however, the magnitude of the excited-state cross section exceeds that of the ground-state. It is in this red to near-IR region for which the optical limiting potential of these materials is targeted. Moreover, because of the fast appearance of the excited-state absorption (~350 fs), high quantum yield of remaining in the excited-state (~80%), and ~3.0 ns radiative decay time, it is proposed that this material would

make a potentially useful picosecond optical limiter. In Figure 4.11, the RSA ratio in equation 4.10 is shown as a function of wavelength. Additionally, an ideal optical limiter exhibits the limiting effect in a beam fluence range above the saturation fluence (F_s) of the ground-state absorption. F_s is defined as the saturation energy per unit area ($F_s = h\nu/\sigma_{GS}$).[156] Therefore minimization of F_s is desired, requiring higher ground-state absorption cross sections, while keeping the ratio of the excited-state and ground-state cross sections high enough for reverse saturable absorption. The carbon compound C_{60} has been shown to possess highly desirable, broadband limiting properties,[154, 155] and thus it is useful to compare some numbers between this system and the silver clusters. While C_{60} has an RSA ratio of approximately 3.1 and a saturation fluence of 0.27 Jcm^{-2},[156] Ag660 shows a maximum RSA ratio of ~140 and a saturation fluence of ~0.15 Jcm^{-2} at 760nm.

Thus far, however, only an initial experiment was carried out, for the limiting of ~7ns pulses from an amplified 10 Hz Nd:YAG laser. This is not an ideal time range due to the significant repopulation of the ground-state from radiative relaxation. In fact, at 7ns it is estimated from femtosecond transient absorption spectra that approximately 96% of the population has decayed. This yields a reverse saturable absorption value of 2.36. Similar calculations for the Ag680 and Ag710 emitters at the same wavelength (730nm), yieled parameter values of 1.06 and 0.201 were found, respectively, indicating all but the Ag710 is expected to show optical limiting behavior. Figure 4.12 shows the optical limiting plot of the three emitters, with the transmission (calibrated by the initial value,

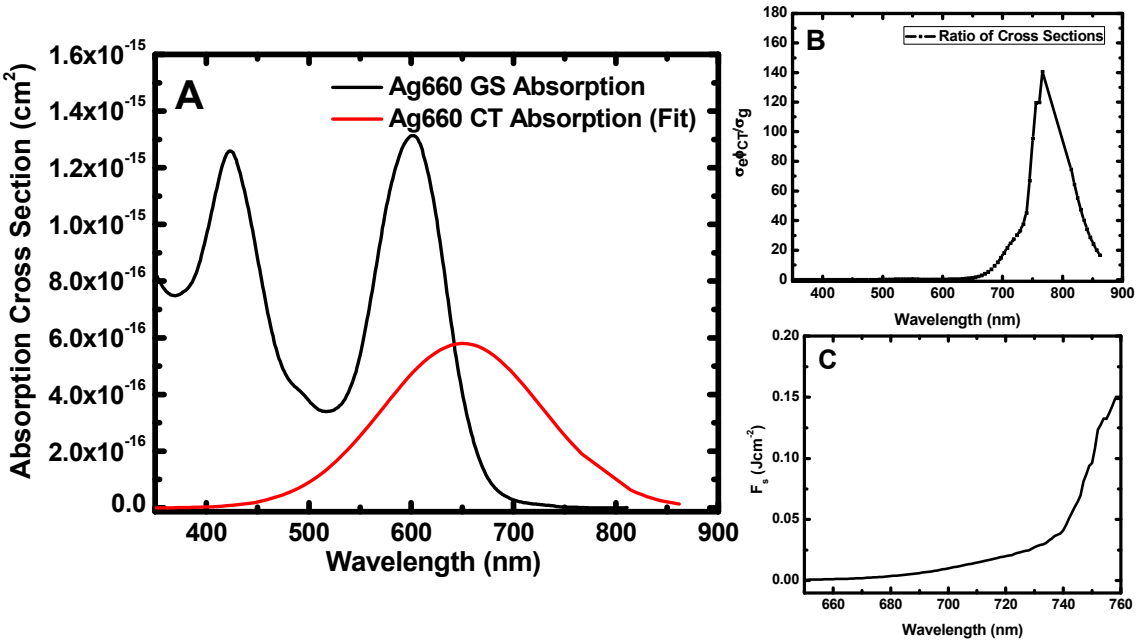

Figure 4.11. (A) The absorption cross section spectra of the Ag660 ground-state and excited-state levels. The ground-state spectrum show was produced by a UV-vis spectrometer calibrated to the measured peak absorption cross section. The excited-state spectrum, assigned to the charge-transfer state of the sample, is a fit of the data produced by nanosecond transient absorption. (B) The reverse-saturation absorption ratio, which is produced by the ratio of the absorption cross sections multiplied by the measured charge-transfer quantum yield (80%) in the picosecond time region. (C) The saturation fluence of the ground-state ($h\nu / \sigma_{GS}$). This is the saturation energy per area of the ground-state transition.

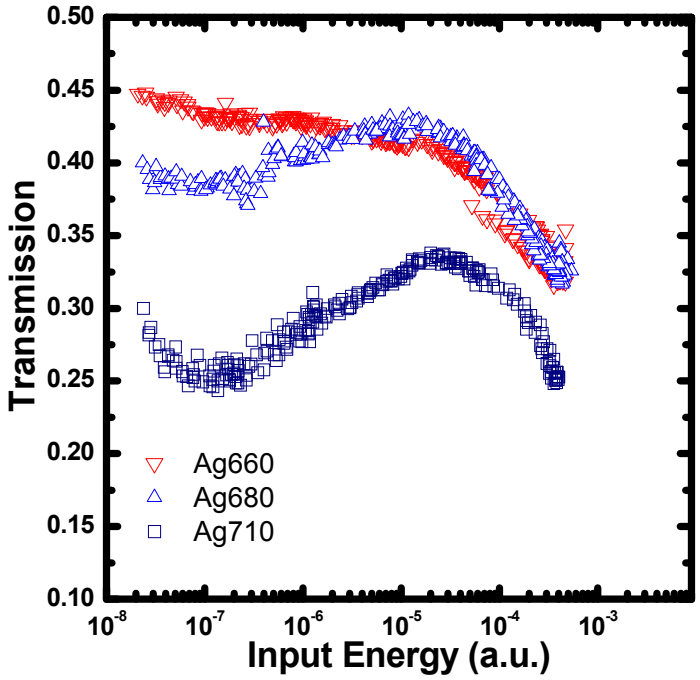

Figure 4.12 Nanosecond optical limiting effect of the Ag660, Ag680, and Ag710 species from a ~7 nanosecond, 10 Hz laser at 730nm. The Ag680 and Ag710 species exhibited an unusual increase in transition in the mid-energy levels before displaying the limiting effect at higher energies. Fluorescence emission is believed to be responsible for this behavior, while for the Ag660 species, whose emission is further shifted from the limiting wavelength, more typical behavior is observed of constant transmission and lower energies.

measured by steady-state absorption from a spectrometer) shown as a function of input pulse energy. The attenuation of the pulse was referenced to its initial energy, and used to calculate the attenuation due to the sample. As can be seen, the Ag660 shows the greatest change in transmission (31%), while the Ag680 (22%) and the Ag710 (17%) show lower declines, but are marked by anomalous increases in transmission in the middle energy regions of the curve. This is most likely due to fluorescence and perhaps stimulated emission, which for 730nm should be most pronounced for the Ag710 species, as corroborated in the optical limiting. The Ag660 remains relatively flat in the linear region of the transmission curve, marked by a drop at higher energies. More detailed studies are needed, but good optical limiters are characterized by more than 100 fold decreases in transmission. The silver clusters here are significantly poorer than that, which may be due to sample degradation over time or to the repopulation of the emissive state due to transient absorption. Limiting occurs within the pulse width of the laser (7 ns), which is expected to be sufficient time for repopulation to occur, thus additionally countering the reverse saturation effect.

Despite the non-ideal time range chosen for this experiment, limiting was still observable, as predicted by the RSA ratios. Future studies will make note that in the picosecond and several hundred femtosecond range the excited-state populations are maximized and therefore are ideally suited for limiting behavior.

4.6 Conclusion

In this chapter the complex excited-state photophysics of oligonucleotide-encapsulated silver nanoclusters have been introduced and explored. Approximately 15-30% of the excited-state population radiatively decays to the ground-state, with about a 3 ns lifetime. About 20% of the population, however, has been shown to undergo rapid charge separation as the rather polarizable silver electron is donated to the surrounding DNA. Cytosine is the most likely binding site for the cluster, and previously reported absorption spectra of anionic cytosine are strikingly similar to the transient absorption spectra of nearly all the fluorescent cluster species. Further evidence of this model comes from the approximately 10% photoejection quantum yield observed for silver clusters of ten atoms or less in solution,[136] a number similar to the 20% yield determined by transient absorption in the present study. Back electron transfer, however, seems to occur on significantly longer times scales, with rates of approximately $10^5 s^{-1}$, about 8 orders of magnitude slower than the $10^{13} s^{-1}$ charge separation time scales. The unusually slow process may be a result of the large driving force for recombination, pushing the rates into the Marcus inverted region, resulting in the larger activation energy for return. Additionally, trap sites within the DNA may contribute to the observed rates as well.

The absorption cross sections of the excited states have been shown to be quite large, allowing photoinduced recombination back into the emissive manifold with a secondary laser tuned to the excited-state resonance. The use of two lasers gives greater control over the average emission rates of the molecule, as the microsecond states are quickly and efficiently depopulated by

that second laser, enabling optical modulation and greater discrimination from noise and fluorescent background in imaging applications. The large cross sections make feasible the use of the low intensity excitation necessary for biological systems.

The microsecond blinking dynamics observed on the single molecule level have been intimately linked to the charge-transfer state probed in the bulk transient absorption spectra. A good understanding of the mechanism behind the blinking dynamics is now available, which is crucial for future efforts to further control the emission properties of these remarkably bright and stable fluorophores.

Without better structural information, however, interpretations of the transient experiments are limited. It is expected that the recently improved synthesis procedure that has enabled preparation of high concentration samples will unlock previously unfeasible structural characterization methods. Their utility as fluorescent probes has been extensively demonstrated, and future improvements as well as theoretical modeling will unquestionably require more precise structural knowledge. Many unanswered questions remain. For example, the sizes of the individual clusters themselves and their relationship with the emission energies are not known. The nature of the interaction between the silver cluster and encapsulating DNA is only beginning to be answered. These answers will help solve the more complex problems of how charge separation occurs and to what extent does the charge exist in the DNA. More diversified applications may in fact be opened up as a result of addressing this

question. For example, photovoltaic materials are currently being sought which can efficiently transfer photon energy to drive charge separation. Knowing the nature of the separated charge in this system will allow future research to more accurately assess their efficacy as photovoltaic materials.

CHAPTER V
DENDRIMER-ENCAPSULATED SILVER CLUSTERS

5.1 Introduction

5.1.1 Fluorescence

Because dendrimer-encapsulated silver clusters can only be formed by photoinduced reduction in low yields on a surface, these species were studied by single-molecule fluorescence analysis. As with oligonucleotide species, multiple emissive species can be produced with fluorescence peaks spanning the visible region. But without an easy way to facilitate the selective synthesis of a singly-emissive species, all of them are produced in a distribution. The preparation is carried out such that individual molecules are sufficiently separated, so they can be individually analyzed. Despite these difficulties, their remarkable optical properties, such as bright, photostable emission by one-photon and two-photon excitation along with the observation of hyper-Rayleigh scattering from single molecules have warranted the understanding and analysis undertaken in this work.

The emission properties of the clusters have been well-characterized in previous reports, indicating strong, stable emission from individual molecules.[25, 26] Mass spectrometry data indicate that the clusters, just as for oligonucleotide-encapsulated clusters, range in size from 2 to 6 atoms. There are several notable differences in the photophysics of the dendrimer-encapsulated clusters

as compared to them, however. First, the different emissive species all appear to have common or closely-spaced excitation spectra, peaking at around 470 nm. The emission maxima are 533 nm, 553 nm, 589 nm, 611 nm, and 648 nm.[26] The Stokes shift, therefore, ranges from 1400cm^{-1} to 5800cm^{-1}, increasing significantly as the emission tends towards lower energies. The oligonucleotide-encapsulated clusters, on the other hand, have relatively similar Stokes shifts even for clusters emitting the near-IR. Stokes shifts between ground-state absorption and fluorescence can arise by a variety of mechanisms. First, the shifts can come about by the vibrational relaxation from the initial excited state. Franck-Condon overlap between the ground and excited electronic states are typically larger for higher vibrational levels in the excited state. Therefore upon excitation, these vibrational modes quickly dissipate energy (10^{-13}-10^{-12} s) before emissive relaxation to the ground state.[119] Additionally, initial electronic excitation can leave the molecule in an even higher electronic state from which it then relaxes to the emissive electronic state by Kasha's rule. This usually occurs on the 10^{-12} s scale in the process known as internal conversion. Vibrational relaxation is on the order of 1500 cm^{-1}, however, and the dendrimer-encapsulated silver clusters exhibit a significantly higher shift, especially for the lower energy emitters. Internal conversion may then be more likely, with energy level spacing a function of cluster size and geometry. Another mechanism that has been proposed is the excited-state coupling to a dissociative state. In this scenario, upon excitation, the cluster undergoes a pre-dissociative nuclear relaxation. Matrix caging, however, prevents complete dissociation, and instead

results in radiative relaxation to the ground state at much lower energies. In the end, though, no clear evidence exists to resolve the excited-state dynamics.

The fluorescent clusters exhibit all the indicators of single molecule behavior, clearly emitting in a dipole radiation pattern with antibunched photon emission. The clusters additionally have the fluorescence intermittency dynamics characterized by many single molecules. Unlike most organic dyes and oligonucleotide-encapsulated clusters, however, the dynamics occur continuously on broad time scales covering the microsecond to the hundreds of milliseconds scale. Oligonucleotide clusters, on the other hand, show exponential time trace autocorrelations with dynamics on the 10 microsecond scale, attributed to charge transfer. Multiple levels of emission are also observed, with no clear emission levels, but instead are characterized by sharp, intense spikes. It is believed that dynamics in the interaction with the encapsulating dendrimer or in the conformation of the cluster itself are linked these seemingly chaotic blinking dynamics.

The strong emission is coupled with a fast radiative lifetime, measured to be 20-40 ps. This is two orders of magnitude faster than the oligonucleotide clusters, indicating that the oscillator strength for this radiative transition is extremely large. This value can be estimated from the excitation spectra of the silver clusters (no absorption data is available), and the estimated absorption cross section (10^{-14} cm^2), which equals $2.6 \times 10^6 M^{-1} cm^{-1}$. Using a similar analysis as that described in section 3.1, the oscillator strength takes on a value of 44.3. This is remarkably large, and is consistent with the faster radiative lifetime

(although only one order of magnitude larger than the oligonucleotide-encapsulated clusters). The high transition strength may result from any number of mechanisms, including its size and geometry, relative coupling to the encapsulating agent, or oxidation state.

5.1.2 Surface-enhanced Raman Scattering

Raman scattering is an inelastic scattering process in which the scattered photon differs in energy from the incident photon by the vibrational energies of the molecule. Energy is transferred from the photon to the molecular vibrational modes. The Raman scattering cross sections are typically too small (~10^{-29} cm^2) for sensitive molecular identification and detection use. For comparison typical absorption cross sections range from 10^{-19} to 10^{-17} cm^2, approximately 10 orders of magnitude higher. The discovery of an effect called surface-enhanced Raman scattering (SERS) in 1973 by Fleischmann and coworkers,[160, 161] however, closed the gap in cross sections. Dyes adsorbed on the surface of 50-100 nm silver nanoparticles have enhanced Raman cross sections up to 10^9 times in bulk. The enhancement mechanism, although still not definitively agreed upon, consists of a combination of increased local electric field intensity, due to the extremely high oscillator strength of the plasmon, and a charge transfer effect between the adsorbed dye and the particle. On the single particle level, enhancements of up to 10^{15} have been observed for adsorbed rhodamine 6G dyes.[162]

Recently, reports have shown that SERS also occurs for the dendrimer-encapsulated and peptide-encapsulated fluorescent silver clusters.[163, 164] In each

case the partial Raman spectra of the encapsulating agent is observed for single clusters at similar strengths to that measured for large particles. For small clusters, the plasmon enhancement factor is expected to play a significantly smaller role in the overall SERS effect. Instead, a mechanism based on resonance enhancement with the strong radiative transition is believed to occur. The high oscillator strength (~44) of the silver clusters (calculated based on the method described in Chapter 3) certainly lends credence to this model, as there is ample transition strength to be transferred to the vibrational transitions of the surrounding dendrimer.

5.2 Two-photon Excited Fluorescence

As with oligonucleotide clusters, the dendrimer clusters exhibit a strong, easily observable TPE fluorescence. At least five spectrally distinct species have been identified, as shown in Figure 5.1. Comparison to OPE data shows that the emission peaks coincide well, except in TPE a new emitter was identified, peaking at 505 nm. The others peak at 532, 560, 588, 607, and 646 nm. It is likely that this emitter can also be excited by OPE, but due to the 475 nm excitation wavelength typically used and the long pass emission filters, this wavelength region is not accessible. Each species possesses a reproducible spectrum; that is, the emission spectra do not continuously peak throughout the range, but rather take on the discrete spectra shown. Just as in the oligonucleotide-encapsulated silver clusters, these species are believed to be the

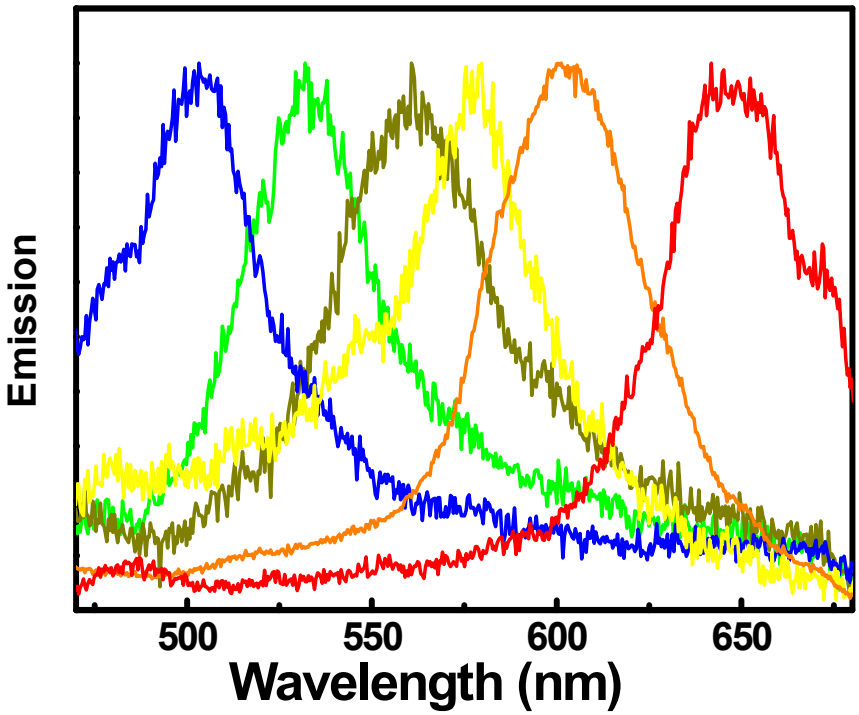

Figure 5.1 Superimposed emission spectra of several species showing emission wavelengths spanning the visible region. Each spectrum was taken individually by irradiating an individual emitting species on a glass surface with 855 nm, femtosecond Ti-sapphire pulses, and collecting emission at higher energy through a monochromator and CCD device. Spectra were integrated for 5 seconds.

result of size and geometry distributions. Mass spectrometry data have confirmed that the solution containing these emissive species also contain silver clusters from 1-6 atoms, although, as before, specific assignments could not be made.[25] The two-photon action cross section was measured for the particles by comparing with single CdSe/ZnS quantum dots, whose TPA cross sections have been reported elsewhere (Figure 5.2).[67] Because concentrations of the silver clusters could not be measured, single spots were compared, assuming that in each case the spots corresponded to single molecules. Comparing the relative fluorescence, the cross section has a measured maximum at 720 nm, with a value of $1.3\times10^{6} GM$. This action cross section is approximately two orders of magnitude larger than oligonucleotide-encapsulated silver clusters.

The radiative lifetimes for individual species were measured using time-correlated single photon counting. As can be seen in Figure 5.3, while the lifetime of OPE emission, though quite fast, produced a decay slightly broader (deconvoluted and fitted to ~40 ps) than the instrument response function (IRF = 31 ps), TPE emission decays were, however, indistinguishably limited by the IRF. Radiative relaxation is expected to have a lifetime comparable to that of OPE at the same emission wavelengths. There is a bi-exponential decay observed in OPE, for which the IRF-limited component in was assigned to SERS while the longer component was attributed to fluorescence. All emissive species yielded identical results. This suggests that either the rate-limiting step is not the residence of the radiative state but rather one of the higher excited states, or that the TPE emission is quenched by a non-radiative pathway inaccessible by OPE.

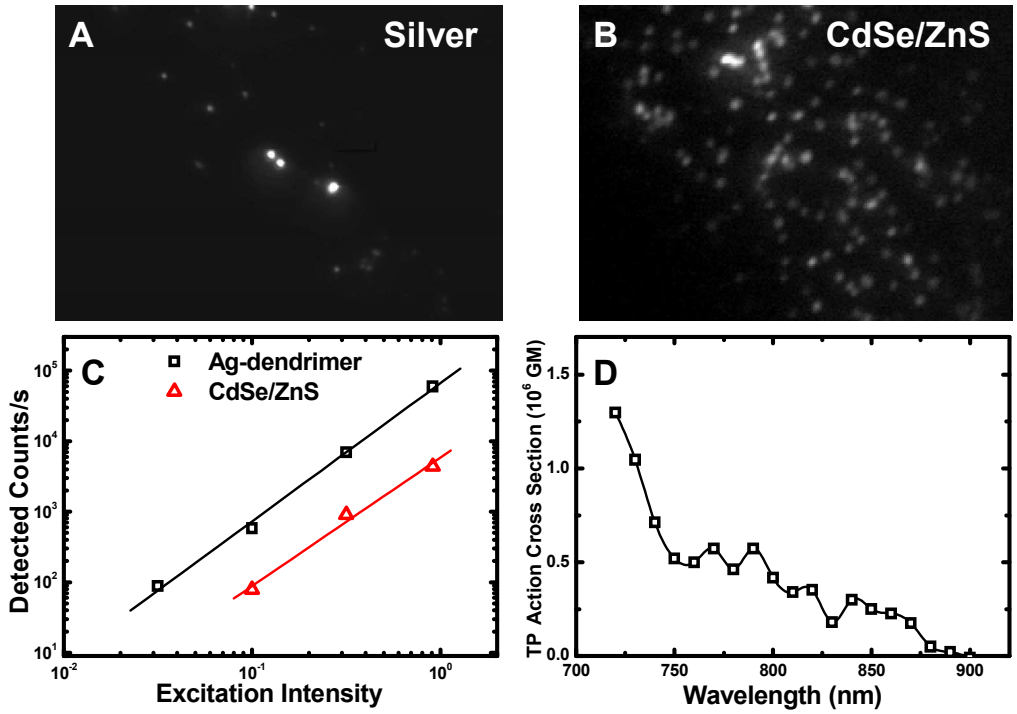

Figure 5.2 Images of TPE for (A) isolated silver clusters and (B) CdSe/ZnS quantum dots, both irridiated with 810 nm, femtosecond Ti-sapphire pulses. The two-photon excited fluorescence was compared for the two systems, averaged over several hundred molecules, and plotted as a function of excitation dependence. The excitation spectra, showing the calculated TP action cross section.

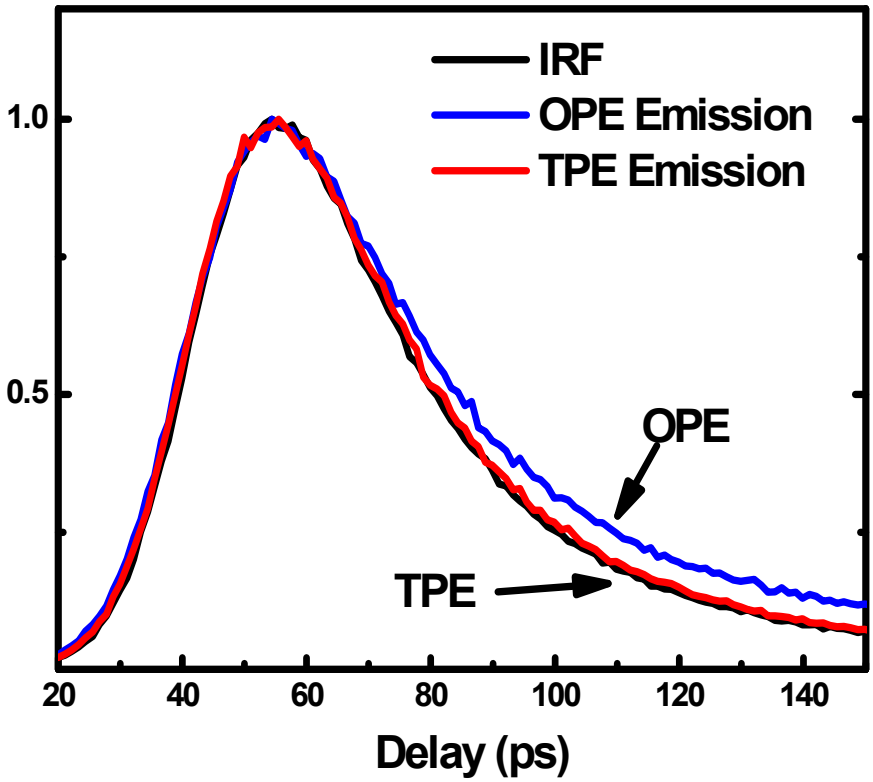

Figure 5.3 Radiative lifetime of the dendrimer-encapsulated silver clusters, with both one-photon excitation (425 nm) and two-photon excitation (850 nm). The emission was recorded at 650 nm (fluorescence) and 425 nm (hyper-Rayleigh scattering, not shown). The IRF (31 ps) was identical to both emission peaks using two-photon excitation, indicating that the process is significantly faster than this. The one-photon emission, on the other hand, showed a slightly slower decay was fit to ~40 ps.

Considering that the observed radiative lifetime is on roughly on the time scale of electronic relaxation and molecular dissociation processes, it is not unexpected that those processes would be rate-limiting. As absorption-based quantum yield measurements are not possible for these single clusters species, the quenching mechanism could not be directly verified. Instead, emission intensity from OPE versus TPE was compared for single clusters as a function of excitation intensity. With pulsed excitation in which the time between pulses is significantly longer than the radiative lifetime, increasing the peak intensity should correspond to an increase in excitation rate until saturation due to the limit of absorption is reached. Comparing the relative emission intensities at saturation should give a rough, relative quantum yield, given that the concentration is known. Moreover, for single molecule excitation this should provide a way in which absolute quantum yield can be measured, as the metric for a perfect quantum yield is set by the laser repetition rate, assuming no other processes yield emission or no long-lived dark state is populated. The average OPE and TPE emission rates for a single species (for ~100 molecules) was measured to be about 102 kHz and 89 kHz, respectively. Accounting for an approximate 1% collection efficiency, the total emission rates would be 10.2 MHz and 8.9 MHz, respectively. The estimated quantum yields based on this would be 12.2% and 10.6%. Ignoring blinking dynamics, these numbers would suggest that excited-state quenching is not a significant mechanism for two-photon excitation.

5.3 Hyper-Rayleigh Scattering

5.3.1 Spectra

In addition to the single-molecule OPE and TPE fluorescence, the photo-activated silver clusters are able to non-linearly scatter light. HRS, as with Raman scattering, is typically too weak to detect over background on the single-molecule level, with only a few reports indicating detection on the single particle scale for semiconductor quantum dots[165] and silver, gold, and copper nanoparticles of greater than 10nm.[166]

A sharp peak at double the excitation energy appears for all of the emissive species, shown in Figure 5.4. In the inset, the averaged spectrum of 36 molecules is plotted along with that of the laser doubled by a commercial BBO crystal. The overlap of spectra, along with the quadratic excitation dependence, suggests the peak is due solely to HRS. Upon tuning of the excitation wavelength, the broad emission peak remains at the same energy while the HRS peak shifts, as expected. Because this scattering effect has been observed with large silver particles, attributed, as in SERS, to the plasmon oscillator strength enhancement, it was necessary to independently confirm that HRS in this case results from fluorescent, several atom clusters with sub-nanometer sizes.

Several steps were taken to discriminate emissive and HRS-active clusters from those of larger, plasmon-sustaining nanoparticles, for which HRS has been previously reported. Figure 5.5 shows two images of the same sample area, one

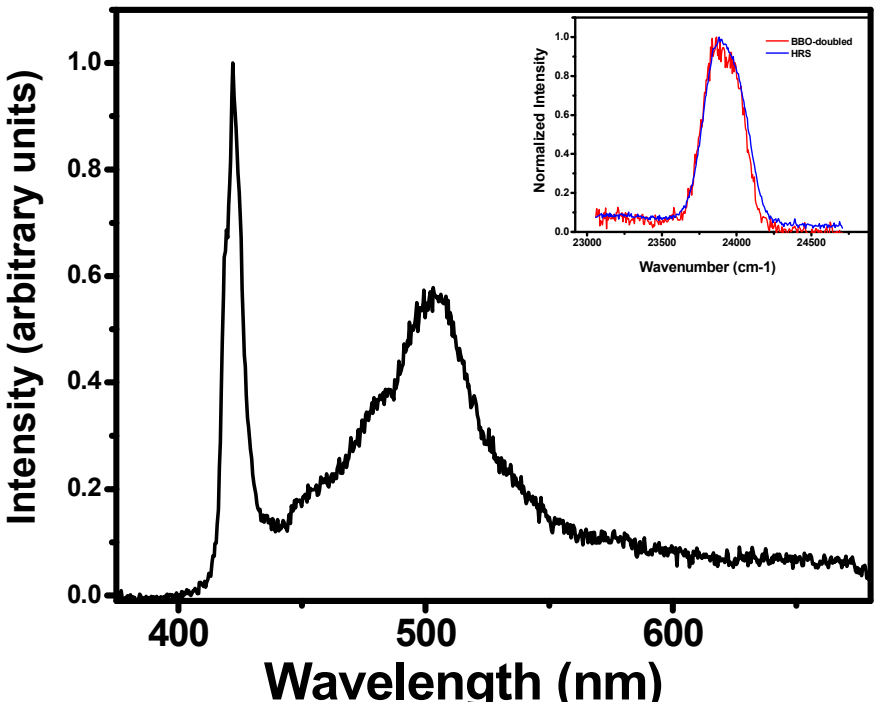

Figure 5.4 Emission spectra from TPE of a single species showing an emission peak at 504 nm and a hyper-Rayleigh scattering peak at double the excitation energy (422nm) Inset shows the averaged HRS peak of 36 molecules compared with the BBO frequency-doubled laser spectrum

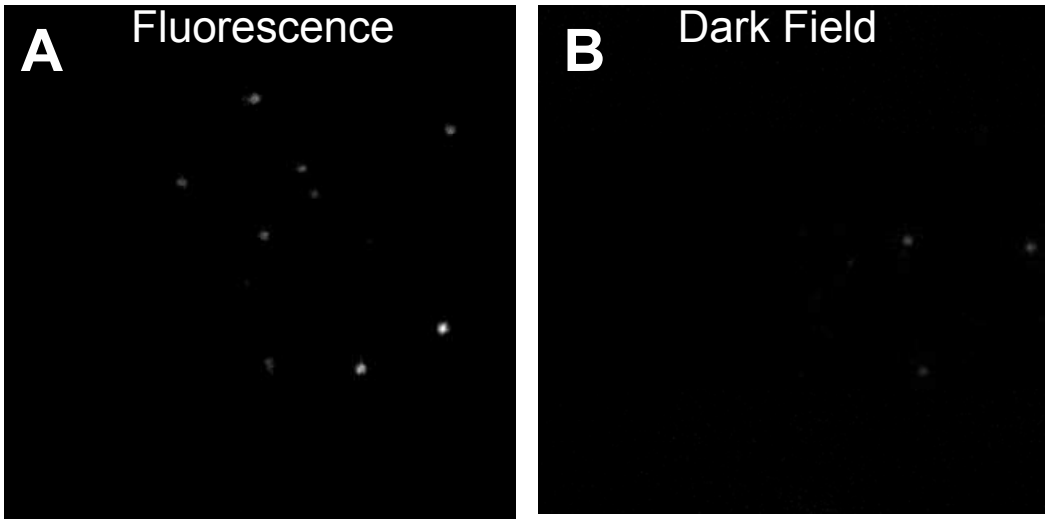

Figure 5.5 (A) TPE emission image of dendrimer-encapsulated silver clusters irradiated with an 855nm, femtosecond Ti-sapphire pulsed laser. A 750 nm short-pass filter was placed in the emission path to block out the laser, but retain any other higher energy emission. (B) An identical field of view of the dark-field scattering image. The images demonstrate that emissive species can be smaller than the 1.4 nm diameter limit of dark-field detection.

dark-field scattering image and the other showing emission upon excitation with $855nm$ light. The spots correspond to individual clusters, and although some scattering spots are present in the dark-field image, they are not correlated with the emissive spots. A spectrum of one of these species reveals the TPE fluorescence along with the HRS peak. These molecules are shown to be true single photon emitters, further demonstrating that the observed emission and HRS arise from a single cluster.

This behavior can be measured by using a well-known measure of single-photon emission, the antibunching of emission. Using the pulsed femtosecond Ti-sapphire laser, an individual spot was excited and its luminescence and scattering were collected. The HRS and fluorescence signals were separated by a dichroic and emission filters, and each signal was sent to be collected by an APD. Before reaching the APD, the fluorescence signal was split into two and collected separately, so that an autocorrelation could be performed. The time traces were recorded, as seen in Figure 5.6. In the long time scale time trace, the similarity in the HRS and fluorescence signals can be seen, with the vast majority of the intense spikes correlated between the two. A baseline emission count rate for this particular molecule is measured to be approximately $6\times10^{4} counts/s^{-1}$, with spikes reaching peaks of $2\times10^{5} counts/s^{-1}$. The signal shown in the figure is only the split signal and hence does not reflect the total count rates. The autocorrelation function was generated within one of these spikes for the two fluorescence time traces, and an example is shown in the figure. As the period of the laser pulses was 11.9 ns, pulses in the

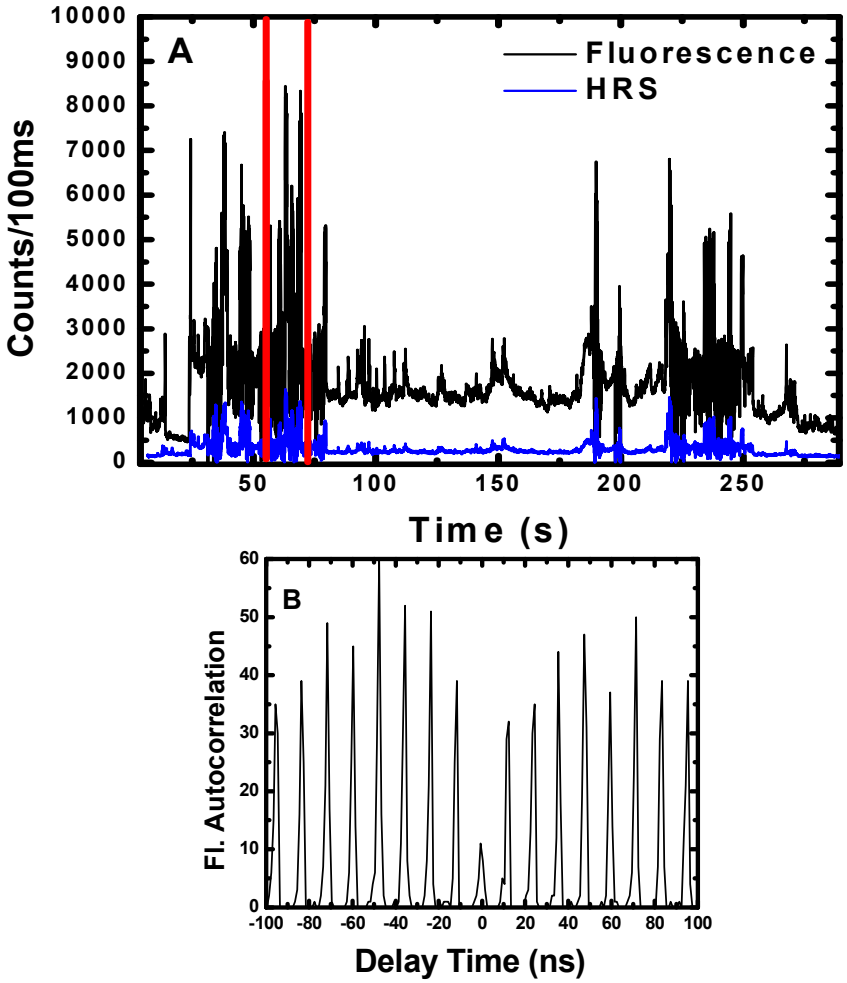

Figure 5.6 (A) Time trace of single silver cluster species as recorded by an APD, comparing the emission outputs for fluorescence (500-600nm) and hyper-Rayleigh scattering (425 nm) from two-photon excitation at 84 MHz. The time trace shows strong, sharp peaks which are correlated between the fluorescence and scattering signals. (B) The autocorrelation function of a small portion of the time trace (indicated by the vertical, red lines), at short time delays, is shown for the autocorrelation of one of the large spikes in the fluorescence signal. An antibunching signal is observed for this small portion, but is not present in the majority of the time trace autocorrelation.

autocorrelation can be seen reflecting that time difference. The feature of interest, however, is the depressed peak at zero time delay, which results from the low probability of two photons arriving simultaneously at the two detectors for a single molecule. Ideally for a true single molecule with no background, no autocorrelation intensity should be seen at zero delay time. The area of the peak in Figure 5.6b at zero delay is 31% of the average area of the 20 surrounding peaks. The expected dip of this peak as a function of the number of independent single-photon emitters scales with n^{-1}, and so a dip greater than 50% is undeniably a single emitter. This feature, however, only appears for a small percentage of these spikes within one time trace. For most of them, the peak at zero time delay is indistinguishable with the other peaks. This unusual behavior might be explained by the dynamics of the cluster within its dendrimer environment, or by the presence of closely-spaced emitters, wherein a single emitter may show extremely bright emission at a given time, accounting for the spikes in the time trace. Additionally, the presence of an antibunching peak suggests that the TPE lifetime is in between the pulse width of the laser ($\sim 200\,fs$) and the IRF ($\sim 30\,ps$). If the lifetime were faster than the pulse width, the probability of observing two photon events in one pulse would be finite.

5.3.2 Incoherent versus Coherent scattering

Like most optical effects on the nanometer scale, the strength of second harmonic scattering as well as its mechanism is highly size dependent. Theoretical models developed for second harmonic generation on the scale

between 5 and 100 nm, e.g. Heinz and coworkers,[51, 78] rely on coherent scattering approaches in which a fixed sphere of a given dielectric produces a second harmonic signal despite its inversion symmetry. This is accomplished by breaking the dipole approximation and considering higher multipole contributions, most notably the quadrupole moment. There is also an electric dipole contribution that arises from the nonlocal retardation of the light beam as it passes through the sample, which can also give the second harmonic signal. Scattering by quadrupole polarization relies on the resonance enhancement of the quadrupole plasmon peak with the incident radiation frequency, and results in coherent, second harmonic generation. The total scattered power in this model is both a function of particle size (R^6 dependence) and incident frequency (ω^6), which is then further enhanced resonantly by the plasmon frequency (either dipole or quadrupole). Additionally, the model predicts a radiation pattern that reflects the mechanism, producing either a 2-lobed pattern (dipole) or a 4-lobed pattern (quadrupole). The measurement of this pattern can be accomplished either by rotating the polarization of the incident beam and measuring the SHG power at a fixed angle, or by changing the angle at which the SHG is recorded.

The model has been verified experimentally by various groups, including Hupp and coworkers who, using R = 16 nm silver nanoparticles, measured the excitation spectra of the SHG signal as a function of collection geometry. For a forward geometry in which SHG is collected along the plane normal to the wavevector, both the quadrupole and dipole mechanisms are present. For the 90 degree geometry, in which SHG is collected along the plane normal to the

electric field vector, only the dipole mechanism is detected. The former geometry showed two resonance peaks in the excitation spectrum, while the latter showed only one peak, corresponding to only the dipole.

As the particle approaches atomic length scales, however, the model begins to break down, and quantum size and surface effects must be incorporated. For example, in CdSe semiconductor quantum dots the optical response per CdSe pair decreases with size until approximately 3 nm, at which point the response begins to climb with an R^{-6} dependence down to 1 nm (the limit of the experimental data). As they are working away from bandgap energy resonances, they invoked fluctuation dynamics of the surface, which broke inversion symmetry, and quantum confinement of the oscillator strength as the major mechanisms causing the larger HRS responses.

Lue and coworkers have developed a theoretical model for free electron spheres at R<10nm, for which a similarly large increase in expected SHG signal is expected as the particle size decreases.[82] In their model, they attribute the enhancement, which has been experimentally verified by Aktsipetrov and coworkers,[167] as resulting from the quadrupole susceptibility, which was calculated to have an R^{-1} dependence on particle size. Though no specific resonance conditions were considered, total enhancement factors of up to 120 were predicted for 1 nm particles over 100 nm particles.

Two competing size regimes, therefore, produce seemingly opposite trends in the size dependence of the SHG of small polarizable particles. The small sizes of the fluorescent silver clusters suggest that they should be

considered in the quantum size-effect regime, as modeled by Lue and coworkers.

5.3.3 Resonance Enhancement

The observation of hyper-Rayleigh scattering at the single molecule level and its time correlation to the fluctuations of TPE fluorescence suggest that the HRS is also resonantly enhanced. For two-photon processes, resonant enhancement can transpire by two possible mechanisms. Resonance from the S_0-S_1 transition or the S_0-S_2 transition can occur. Looking closely at the excitation spectra in Figure 5.7 for TPE-fluorescence and HRS, it appears that some overlap is evident between the two transitions. It is unclear, however, where the excitation peak for TPE fluorescence is, as the limited range prevented excitation at lower wavelengths. The OPE peak for silver cluster emission occurs at 475 nm, which is significantly blue-shifted from the TPE peak (< 375 nm, doubled in energy), suggesting that a different state is accessed.

The excitation polarization dependence of the HRS intensity was employed to discriminate a dipole from a quadrupole transition, the latter exhibiting a typical 4-lobed pattern in the emission polar plot. Studies of variously-sized Ag NPs have shown that as the particle size becomes larger (> 40 nm), the quadrupole mechanism begins to dominate, as evidenced by the shifting polarization dependence from a 2-lobed to a 4-lobed pattern.[81] Additionally, due to the differing selection rules, each mechanism has a unique resonance condition, observable by two excitation peaks in the HRS signal.[80]

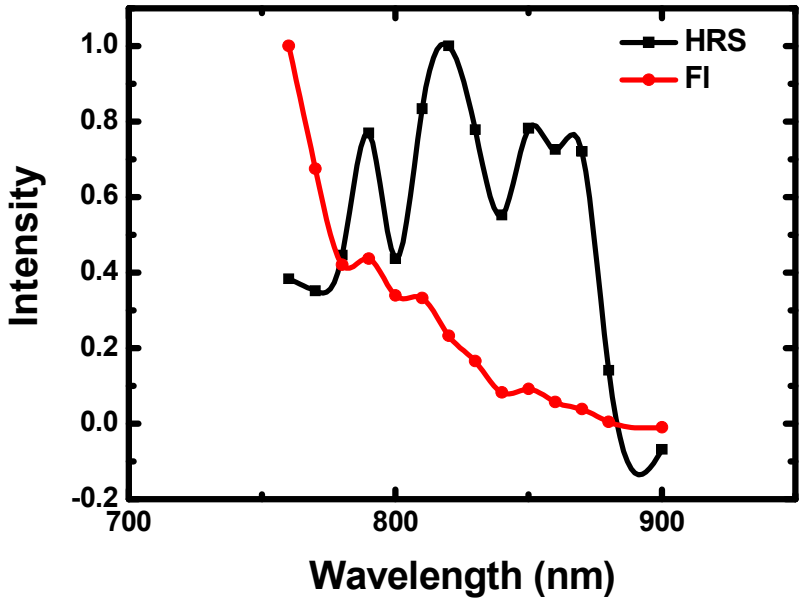

Figure 5.7 Excitation spectra for fluorescence and hyper-Rayleigh scattering from dendrimer-encapsulated clusters, measured by a femtosecond Ti-sapphire laser. The intensity at each excitation wavelength was time-averaged for ~100 molecules as imaged by a CCD camera. Each curve is normalized to unity.

For the smaller clusters studied here, the model predicts that only the dipole mechanism should be observable. Two “sizes” of particles were used in this experiment. The first, labeled as nanoclusters were those particles that were transparent in dark-field scattering. The second were particles that were prepared by the same method as the clusters, but were allowed to photoreduce for longer periods of time, thus forming larger particles that were visible by dark-field microscopy. Presumably the large size is actually a wide distribution of particle sizes, all of which are larger than 1.6 nm. Comparing the two species for HRS strength, a histogram of approximately 100 species was constructed, and is shown in Figure 5.8. The nanoparticles had a mean detected count rate of 2.1×10^{5}, while the clusters had a mean of $4.4\times10^{4} counts s^{-1}$ 4.4x10^{4} counts/s. The intensity distribution for the “large” particles, however, was much broader and in fact overlapped (at the low intensity side) with the much more narrowly distributed clusters. Considering that competing size scaling factors are at play, it is ambiguous as how the cluster HRS intensities relate to the particle HRS intensities. More specific studies with known and narrowly distributed cluster sizes are necessary to make conclusive arguments.

Figure 5.9 shows a comparison of the excitation polarization dependence, using linearly polarized light, between the nanoparticles and nanoclusters, with respect to recorded HRS. The data is shown on a polar plot, and the cluster shows a dependence resembling the dipole transition mechanism. The nanoparticle, on the other hand, shows a dependence resembling a more

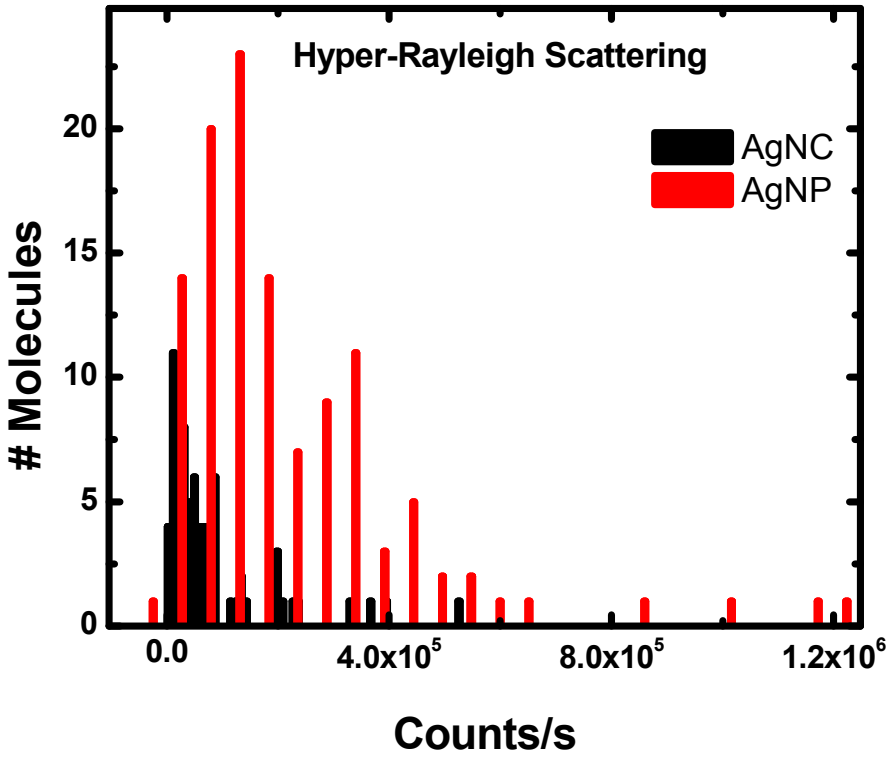

Figure 5.8 Average intensity distribution of the hyper-Rayleigh scattering for fluorescent clusters exhibiting no dark-field scattering versus those that do exhibit dark-field scattering. The counts were measured by a CCD camera and a histogram was generated for series of molecules.

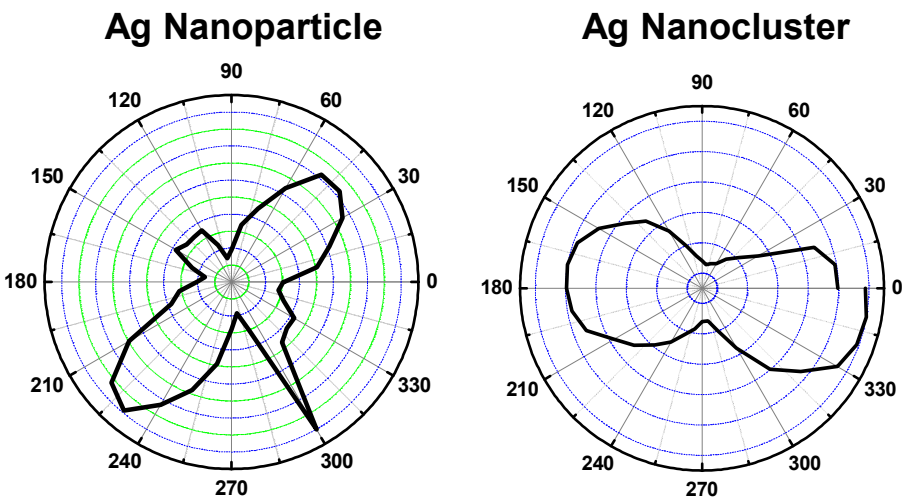

Figure 5.9 Example of the inearly-polarized excitation polarization dependence of the hyper-Rayleigh scattering signal at 850 nm, for nanoparticles, which are bigger than 1.4 nm diameter, and nanoclusters, which are smaller than the 1.4 nm limit of dark-field microscopy. Though this example exhibits quadrupolar and dipolar patterns for the nanoparticle and nanocluster, respectively, the majority of the species did not exhibit clear patterns, most likely attributed to aggregation of multiple emitters.

quadrupolar transition, which is consistent with the size-dependence of the dipole/quadrupole in silver nanoparticles as reported by Brevet and coworkers. These are both examples, however, of isolated cases, as the majority of nanoparticle samples exhibit dipolar behavior (~90%). In many cases there was no clear pattern, which perhaps could indicate aggregated particles. Without knowing more about the sizes of the clusters, however, conclusions are limited.

5.4 Time-gated Fluorescence Lifetime Imaging

Time-gated microscopy has been widely utilized to discriminate the signal of long-lived lanthanide emission from the endogenous fluorophores responsible for biological auto-fluorescence.[168-170] The short-time auto-fluorescence (~1-5 ns) can be rejected, retaining only the emission of the target lanthanide complex (typically >1 ms). For example, if two emitters with lifetimes of 1 ns and 1 μs, normalized for equal steady-state emission, are recorded by time-gated imaging, then at fast times (<6.9 ns) the faster-decaying emitter dominates the emission, but after that the slow emitter has higher emission at any particular point in time.

If the initial time region is excluded, the slow emitter will be selectively imaged. Europium and terbium ions are commonly used for this purpose, While such emitters increase the bulk signal-to-background ratio, their low emission rates preclude observation of low copy number proteins or single molecules. Additionally fast-time rejection requires collecting images for longer time frames and thus can limit use in high-resolution dynamic applications. But

because few emitters have characteristic decay times significantly faster than a few nanoseconds, this has been the only practical way. The relatively fast lifetimes of silver clusters (20-60 ps), however, enables the use of time-gated fluorescence imaging to capture only the short time component.

To demonstrate its effectiveness, a proof-of-principle experiment was designed in which an artificial background was introduced over dendrimer-encapsulated silver clusters on a glass surface, shown in Figure 5.10. With no additional background, cluster emission can be clearly seen for a densely distributed set of clusters. The emission lifetime is limited by the ~200 ns instrument response function. A 1 M solution of rhodamine 6G (R6G) was then added to the cover slip, which collected for steady-state emission, clearly dominated the image. Upon time-gating and collecting images in 100 ns steps, however, the first few images immediately after the excitation pulse clearly show the silver emission visible within the background, while for later images for which the silver emission has decayed the R6G emission again dominates. Taking the ratio of the pixel counts containing silver to those containing just rhodamine, a signal-to-background enhancement factor can be calculated, which is shown to be 17.4 in this experiment. The enhancement is in line with the theoretically predicted value of ~20, determined by the ratio of R6G lifetime to the IRF.

The auto-fluorescence of cells and extracellular matrices originates from a variety of weakly-absorbing fluorophores. The major endogenous fluorophores are prydinic and flavin co-factors, which are prominent in energy-producing mitochondrial compartments and lysosomes. In tissue imaging, collagen gives

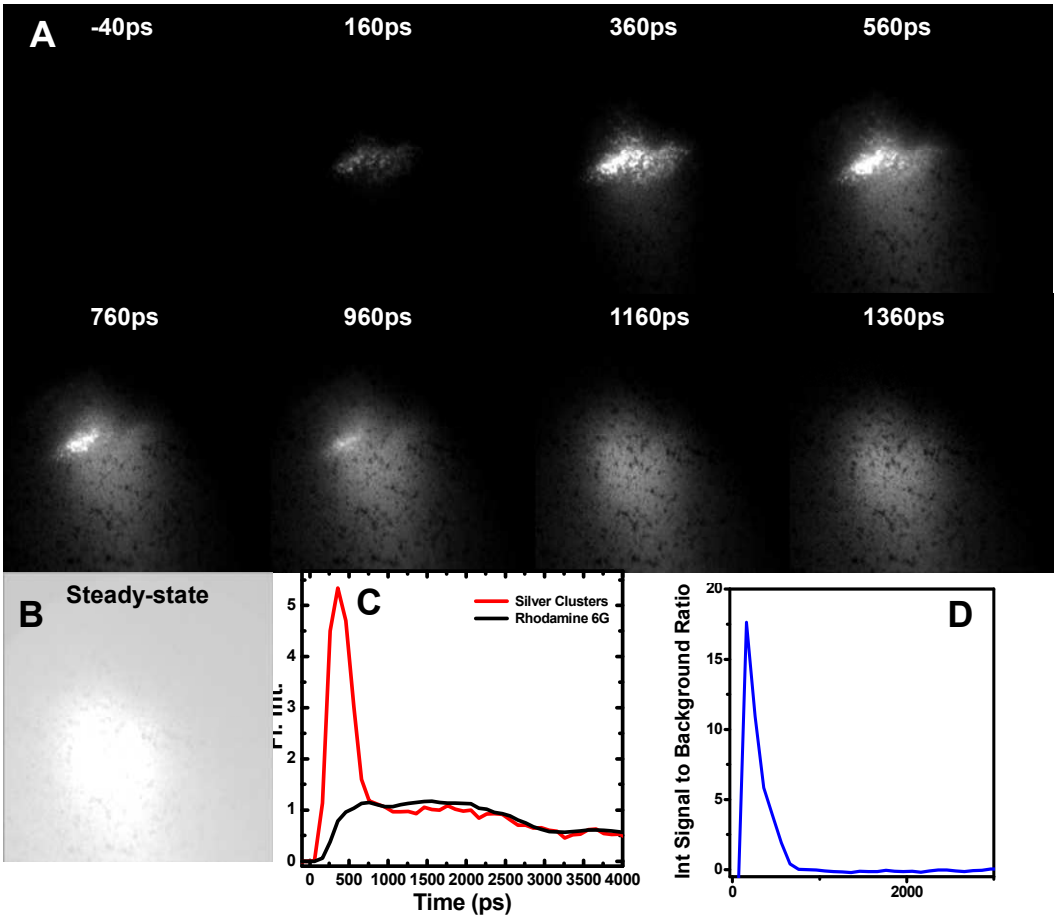

Figure 5.10 (A) Picosecond-gated microscopy glass surface loaded with dendrimer-encapsulated silver nanoclusters, emitting throughout the visible, and co-loaded with 1mM rhodamine 6G. The bright areas in the middle (peaking at 360 ps) correspond to silver emission, while the larger area (shown at 1360 ps) corresponds to the rhodamine 6G. The specified time indicates the delay time imaged relative to the excitation pulse. (B) Steady-state image taken for all gate times (C) Relative fluorescence intensities (averaged per pixel) of the area corresponding to silver cluster and rhodamine 6G and that of only rhodamine 6G. (D) The ratio of the two curves in (C), indicating the enhanced signal-to-background as a function of time delay.

off high quantum yield emission and has a high scattering cross section, resulting in a significant background, which becomes increasingly problematic at higher penetration depths. The mean lifetimes of auto-fluorescent individual NIH 3T3 cells were measured using the FLIM setup, and found to have several components varying between 1 and 3 ns for 468nm pulsed diode excitation. This allows for 5-15 times signal-to-background enhancements.

As the technique has been shown to perform sufficiently using a controlled background addition, cluster-stained fixed cells were tested next. Silver nanoparticle-based staining has been frequently used by pathologists to detect nucleolus organizing regions within cells and thus partially reveal nucleolus location. The specific staining is due in part to the known argophyllic nature of nucleolin, a 700 amino acid protein found in the nucleoli. The nanoparticles were formed inside the cell upon silver nitrate (>5.8 M, 60 °C) staining due to agglomeration of the silver ions. Instead of the relatively harsh staining conditions used, using much lower (20 mM) $AgNO_3$ concentrations yields fluorescent silver nanoclusters in the nucleolus of NIH 3T3 fibroblast cells, photoactivated at ambient temperatures.

The fluorescent properties of the nucleolin-mediated silver clusters are similar to the other photoactivated, dendrimer- and peptide-encapsulated clusters, with very bright, photostable emission and short picosecond lifetimes. Broadband emission (500-700 nm) is observed, likely due to multiple emissive species of the 2-7 atom clusters distributed throughout the cell. The nucleolus

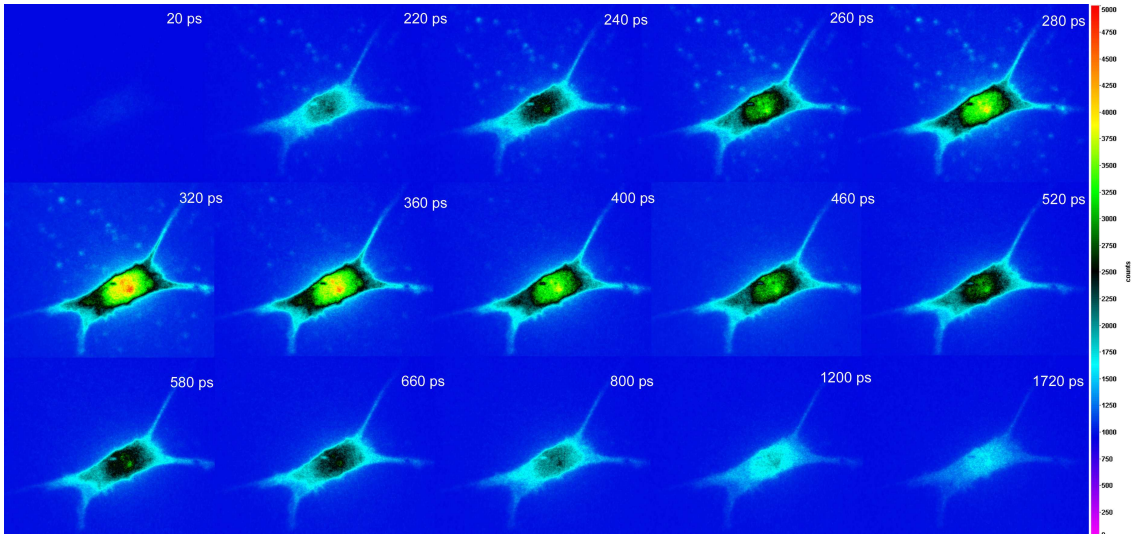

Figure 5.11 Picosecond-gated microscopy of cells stained with silver nitrate. The variation in emission intensity of cell images is in line with the fluorescence lifetime decay of the silver clusters in cells, with one component 220 ps (33%) and another 1760 ps (67%). The time-resolved imaging of cells will afford another window for monitoring cellular behaviors to avoid the fluorescence from co-loaded dyes or autofluorescence.

emission, as seen in figure 5.10, has twice the emission intensity of the cytoplasm, confirming selective nucleolus staining.

Time-gated images were then taken of a cell exposed to a frequency-doubled, 425nm Ti-sapphire laser. Each image was taken in 20 ps steps, with a 1 s integration time. The formaldehyde-fixed cells were loaded with 100 mM $AgNO_3$ for 20 hrs. Shown in Figure 5.11, the bright spots within the nucleoli are attributed to silver emission in the 320 ps image, while virtually pure cell auto-fluorescence is observed in the 1720 ps image. Taking a lifetime trace of the pixels containing fluorescent silver, a bi-exponential lifetime curve is observed, showing a fast component (220 ps, 33%) and a slow component (1760 ps, 67%). Though the fast component comprises only on third of the total emission amplitude, frames captured at fast times clearly show prominent emission. The emission is stable despite continuous illumination of the sample (>30 min) at 1 Wcm^{-2}, further supporting the stability of silver cluster emission inside cellular environments.

5.5 Conclusion

As with the oligonucleotide-encapsulated silver clusters, the dendrimer-protected species produced by photoreduction on glass surfaces exhibit superior brightness and photostable emission. It has been shown here that they additionally possess the ability to non-linearly scatter light by hyper-Rayleigh scattering. This signal can even be detected on the single molecule scale along

with its TPE fluorescence. The large radiative rates, coupled with large absorption cross sections, result in superior oscillator strengths that can be utilized in discriminating imaging techniques such as gated fluorescence lifetime imaging. Despite this, the difficulties in synthesis prevent the more complete characterization of their rich photophysics. The chaotic behavior of the single particles is believed to be the result of the vast distribution of size and environment that is most likely sampled by the clusters.

The explanation of the large hyper-Rayleigh scattering signal, though not resolved, is believed to tie in with the theory explaining the nonlinear scattering from larger, plasmon-sustaining metal particles. A better transition of the observed properties with size is needed for proper explanation, requiring more precise control over the size-selected synthesis of these materials.

Additionally, the relationship between the materials discussed in this chapter and the oligonucleotide-encapsulated clusters discussed in the previous chapters may account for the disparity in optical properties observed. Size and symmetry issues are critical for shaping the electronic energy levels and transition strengths among them. Nevertheless, it has been shown in this work that few-atom silver clusters are capable of remarkably strong transition strengths, resulting in easily observable nonlinear effects down to the single molecule scale.

CONCLUSIONS AND FUTURE OUTLOOK

Fluorescence imaging has been increasingly relied upon as the method of choice for many biological and medical applications. As demands for more sensitive and higher resolution imaging are ever-increasing, it is critical that photostable, and robust fluorophores capable of delivering high emission rates are available. Fluorescent silver nanoclusters offer an attractive compromise between the photostability and brightness of quantum dots and the compact versatility of organic chromophores. They have been shown to be superior in many roles, including as single molecule fluorophores and bulk multiphoton biological staining agents. The two-photon absorption cross sections are several orders of magnitude larger than commercially-available dyes, and they have demonstrated superior photostability under high intensity irradiation.

Despite this, the fundamental photophysical mechanisms underlying emission from few-atom silver clusters are not largely understood. Their optical and electronic properties are highly size-dependent, in part evidenced by the near-quenching of radiative decay from silver particles only several times larger than the ones under investigation here. Complicating the system even further is the encapsulating groups used to stabilize the clusters in solution. Oligonucleotide-encapsulated clusters have been shown here to exhibit long-lived photoinduced charge transfer states, in which the DNA acts as the charge acceptor. These states appear as “dark” states in single molecule studies, responsible for their fluorescence intermittency. The discovery of this state and

the transient absorption spectroscopy used to spectrally map it has allowed the use of photoswitching techniques to enhance the signal-to-background ratios of high-background environments, such as those found in cellular and tissue systems. The high two-photon absorption cross sections as well as the long-lived photoinduced charge-transfer state have been examined and characterized in this work, and both have been identified as important properties for the development of the next-generation biological fluorophores. The fundamental studies presented are only the beginning to more precisely controlling and finely tuning the desired properties of biological molecular reporters. These materials will become increasingly important as more advanced medical technology will demand high-resolution imaging to diagnose diseases and unravel the complexities of cellular traffic.

REFERENCES

1. Shine, K. Science the Endless Frontier: Learning from the Past, Designing for the Future, Arizona State University, Center for Science, Policy, and Outcomes: Arizona State University, 1995.

2. Feynman, R. P. In *There's Plenty of Room at the Bottom*, American Physical Society, Calfornia Institute of Technology: 1959.

3. Faraday, M. The Bakerian Lecture: Experimental Relations of Gold (and Other Metals) to Light *Philosophical Transactions of the Royal Society of London* [Online], 1857, p. 145-181.

4. Mie, G., Articles on the optical characteristics of turbid tubes, especially colloidal metal solutions. *Ann. Phys.-Berlin* **1908,** *25* (3), 377-445.

5. Zhang, S. G., Fabrication of novel biomaterials through molecular self-assembly. *Nat. Biotechnol.* **2003,** *21* (10), 1171-1178.

6. Cui, D. X.; Gao, H. J., Advance and prospect of bionanomaterials. *Biotechnol. Prog.* **2003,** *19* (3), 683-692.

7. Tirrell, M.; Kokkoli, E.; Biesalski, M., The role of surface science in bioengineered materials. *Surf. Sci.* **2002,** *500* (1-3), 61-83.

8. Zharov, V. P.; Mercer, K. E.; Galitovskaya, E. N.; Smeltzer, M. S., Photothermal nanotherapeutics and nanodiagnostics for selective killing of bacteria targeted with gold nanoparticles. *Biophys. J.* **2006,** *90* (2), 619-627.

9. Kim, J.; Park, S.; Lee, J. E.; Jin, S. M.; Lee, J. H.; Lee, I. S.; Yang, I.; Kim, J. S.; Kim, S. K.; Cho, M. H.; Hyeon, T., Designed fabrication of multifunctional magnetic gold nanoshells and their application to magnetic resonance imaging and photothermal therapy. *Angew. Chem.-Int. Edit.* **2006,** *45* (46), 7754-7758.

10. Wieder, M. E.; Hone, D. C.; Cook, M. J.; Handsley, M. M.; Gavrilovic, J.; Russell, D. A., Intracellular photodynamic therapy with photosensitizer-nanoparticle conjugates: cancer therapy using a 'Trojan horse'. *Photochem. Photobiol. Sci.* **2006,** *5* (8), 727-734.

11. Huang, X. H.; El-Sayed, I. H.; Qian, W.; El-Sayed, M. A., Cancer cell imaging and photothermal therapy in the near-infrared region by using gold nanorods. *J. Am. Chem. Soc.* **2006,** *128* (6), 2115-2120.

12. Yang, P. H.; Sun, X. S.; Chiu, J. F.; Sun, H. Z.; He, Q. Y., Transferrin-mediated gold nanoparticle cellular uptake. *Bioconjugate Chem.* **2005,** *16* (3), 494-496.

13. Yu, J.; Choi, S.; Dickson, R. M., Shuttle-based fluorogenic Silver Cluster Biolabels. *Angew. Chem. Int. Ed.* **2008,** *In Press*.

14. Kreibig, U.; Vollmer, M., *Optical Properties of Metal Clusters*. Springer: New York, 1995.

15. Drude, P., On the electron theory of metals. *Ann. Phys.-Berlin* **1900,** *1* (3), 566-613.

16. Ashcroft, N. W.; Mermin, N. D., *Solid State Physics*. Holt: New York, 1976.

17. Johnston, R. L., *Atomic and Molecular Clusters*. Taylor & Francis: London, 2002.

18. Fedrigo, S.; Harbich, W.; Buttet, J., Optical-response of Ag2, Ag3, Au2, and Au3 in argon matrices. *J. Chem. Phys.* **1993,** *99* (8), 5712-5717.

19. Rabin, I.; Schulze, W.; Ertl, G.; Felix, C.; Sieber, C.; Harbich, W.; Buttet, J., Absorption and fluorescence spectra of Ar-matrix-isolated Ag-3 clusters. *Chem. Phys. Lett.* **2000,** *320* (1-2), 59-64.

20. Patel, S. A.; Richards, C. I.; Hsiang, J. C.; Dickson, R. M., Water-soluble Ag nanoclusters exhibit strong two-photon-induced fluorescence. *J. Am. Chem. Soc.* **2008,** *130* (35), 11602-+.

21. Peyser, L. A.; Vinson, A. E.; Bartko, A. P.; Dickson, R. M., Photoactivated fluorescence from individual silver nanoclusters. *Science* **2001,** *291* (5501), 103-106.

22. Richards, C. I.; S., C.; Hsiang, J.-C.; Antoku, Y.; Vosch, T.; Bongiorno, A.; Tzeng, Y.-L.; Dickson, R. M., Oligonucelotide-Stabilized Ag Nanocluster Fluorophores. *J. Am. Chem. Soc.* **2008**.

23. Ritchie, C. M.; Johnsen, K. R.; Kiser, J. R.; Antoku, Y.; Dickson, R. M.; Petty, J. T., Ag nanocluster formation using a cytosine oligonucleotide template. *J. Phys. Chem. C* **2007,** *111* (1), 175-181.

24. Vosch, T.; Antoku, Y.; Hsiang, J. C.; Richards, C. I.; Gonzalez, J. I.; Dickson, R. M., Strongly emissive individual DNA-encapsulated Ag nanoclusters as single-molecule fluorophores. *Proc. Natl. Acad. Sci. U. S. A.* **2007,** *104* (31), 12616-12621.

25. Zheng, J.; Dickson, R. M., Individual water-soluble dendrimer-encapsulated silver nanodot fluorescence. *J. Am. Chem. Soc.* **2002,** *124* (47), 13982-13983.

26. Zheng, J.; Nicovich, P. R.; Dickson, R. M., Highly fluorescent noble-metal quantum dots. *Annu. Rev. Phys. Chem.* **2007,** *58*, 409-431.

27. Martin, T. P., Shells of atoms. *Phys. Rep.-Rev. Sec. Phys. Lett.* **1996,** *273* (4), 199-241.

28. Rao, C. N. R.; Kulkarni, G. U.; Thomas, P. J.; Edwards, P. P., Metal nanoparticles and their assemblies. *Chem. Soc. Rev.* **2000,** *29* (1), 27-35.

29. Kubo, R., Electronic properties of metallic fine particles. 1. *J. Phys. Soc. Jpn.* **1962,** *17* (6), 975-&.

30. Turro, N. J., *Modern Molecular Photochemistry*. University Science Books: Sausalito, CA, 1991.

31. Henglein, A.; Mulvaney, P.; Linnert, T., Chemistry of silver aggregates in aqueous-solution-nonmetallic oligomers and metallic particles. *Electrochim. Acta* **1991,** *36* (11-12), 1735-1741.

32. Mulvaney, P.; Henglein, A., Formation of unstabilized oligomeric silver clusters during the reduction of Ag ions in aqueous-solution. *Chem. Phys. Lett.* **1990,** *168* (3-4), 391-394.

33. Hild, U.; Dietrich, G.; Kruckeberg, S.; Lindinger, M.; Lutzenkirchen, K.; Schweikhard, L.; Walther, C.; Ziegler, J., Time-resolved photofragmentation of stored silver clusters Ag-n(+) (n=8-21). *Phys. Rev. A* **1998,** *57* (4), 2786-2793.

34. Schooss, D.; Gilb, S.; Kaller, J.; Kappes, M. M.; Furche, F.; Kohn, A.; May, K.; Ahlrichs, R., Photodissociation spectroscopy of Ag-4(+)(N-2)(m), m=0-4. *J. Chem. Phys.* **2000,** *113* (13), 5361-5371.

35. Mitchell, S. A.; Farrell, J.; Kenneywallace, G. A.; Ozin, G. A., Optical-emission and absorption studies of silver atoms in rare-gas matrices at 12K - silver atom cryophotoaggregation. *J. Am. Chem. Soc.* **1980,** *102* (26), 7702-7709.

36. Rabin, I.; Schulze, W.; Ertl, G., Light emission during the agglomeration of silver clusters in noble gas matrices. *J. Chem. Phys.* **1998,** *108* (12), 5137-5142.

37. Chen, W.; Joly, A. G.; Roark, J., Photostimulated luminescence and dynamics of AgI and Ag nanoclusters in zeolites. *Phys. Rev. B* **2002,** *65* (24), 8.

38. De Cremer, G.; Antoku, Y.; Roeffaers, M. B. J.; Sliwa, M.; Van Noyen, J.; Smout, S.; Hofkens, J.; De Vos, D. E.; Sels, B. F.; Vosch, T., Photoactivation of silver-exchanged zeolite A. *Angew. Chem.-Int. Edit.* **2008,** *47* (15), 2813-2816.

39. Fedrigo, S.; Harbich, W.; Buttet, J., Collective dipole oscillations in small silver clusters embedded in rare-gas matrices. *Phys. Rev. B* **1993,** *47* (16), 10706-10715.

40. Fedrigo, S.; Harbich, W.; Buttet, J. In *Media effects on the optical-absorption spectra of silver clusters embedded in rare-gas matrices*, World Scientific Publ Co Pte Ltd: 1992; pp 3767-3771.

41. Centonze, V. E.; White, J. G., Multiphoton excitation provides optical sections from deeper within scattering specimens than confocal imaging. *Biophys. J.* **1998,** *75* (4), 2015-2024.

42. Xu, C.; Zipfel, W. R.; Shear, J. B.; Williams, R. M.; Webb, W. W., Multiphoton Fluorescence Excitation: New Spectral Windows for Biological Nonlinear Microscopy. *Proc. Natl. Acad. Sci. USA* **1996,** *93*.

43. Zipfel, W. R.; Williams, R. M.; Webb, W. W., Nonlinear Magic: Multiphoton Microscopy in the Biosciences. *Nature Biotech.* **2003,** *21* (11).

44. Harris, D. C.; Bertolucci, M. D., *Symmetry and Spectroscopy*. Oxford University Press, Inc.: New York, 1978.

45. Boyd, R. W., *Nonlinear Optics*. Elsevier Science: New York, 2003.

46. Woodbury, E. J.; Ng, W. K., Ruby laser operation in the near IR. *Proceedings of the Institute of Radio Engineers* **1962,** *50* (11), 2367-&.

47. Boyd, G. D.; Ashkin, A.; Dziedzic, J. M.; Kleinman, D. A., Second-harmonic generation of light with double refraction. *Physical Review* **1965,** *137* (4A), 1305-&.

48. Kelley, P. L., Second harmonic generation in solids. *J. Phys. Chem. Solids* **1963,** *24* (9), 1113-&.

49. Shoji, I.; Kondo, T.; Kitamoto, A.; Shirane, M.; Ito, R., Absolute scale of second-order nonlinear-optical coefficients. *J. Opt. Soc. Am. B-Opt. Phys.* **1997,** *14* (9), 2268-2294.

50. Scandolo, S.; Bassani, F., Miller's rule and the static limit for 2nd-harmonic generation. *Phys. Rev. B* **1995,** *51* (11), 6928-6931.

51. Dadap, J. I.; Shan, J.; Heinz, T. F., Theory of optical second-harmonic generation from a sphere of centrosymmetric material: small-particle limit. *J. Opt. Soc. Am. B-Opt. Phys.* **2004,** *21* (7), 1328-1347.

52. Feynman, R. P., *The Feynman Lecture on Physics*. Addison Wesley Longman: 1970; Vol. 2.

53. Lukomska, J.; Gryczynski, I.; Malicka, J.; Makowiec, S.; Lakowicz, J. R.; Gryczynski, Z., Two-Photon Induced Fluorescence of Cy5-DNA in Buffer Solution and on Silver Island Films. *Biochem. Biophys. Res. Commun.* **2005,** *328*, 78-84.

54. Xu, C.; Webb, W. W., Measurement of Two-Photon Excitation Cross Sections of Molecular Fluorophores with Data from 690 to 1050nm. *J. Opt. Soc. Am. B* **1996,** *13* (3).

55. Zheng, S. J.; Beverina, L.; Barlow, S.; Zojer, E.; Fu, J.; Padilha, L. A.; Fink, C.; Kwon, O.; Yi, Y. P.; Shuai, Z. G.; Van Stryland, E. W.; Hagan, D. J.; Bredas, J. L.; Marder, S. R., High two-photon cross-sections in bis(diarylaminostyryl) chromophores with electron-rich heterocycle and bis(heterocycle)vinylene bridges. *Chem. Commun.* **2007,** (13), 1372-1374.

56. Albota, M.; Beljonne, D.; Bredas, J. L.; Ehrlich, J. E.; Fu, J. Y.; Heikal, A. A.; Hess, S. E.; Kogej, T.; Levin, M. D.; Marder, S. R.; McCord-Maughon, D.; Perry, J. W.; Rockel, H.; Rumi, M.; Subramaniam, C.; Webb, W. W.; Wu, X. L.; Xu, C., Design of organic molecules with large two-photon absorption cross sections. *Science* **1998,** *281* (5383), 1653-1656.

57. Chung, S. J.; Zheng, S. J.; Odani, T.; Beverina, L.; Fu, J.; Padilha, L. A.; Biesso, A.; Hales, J. M.; Zhan, X. W.; Schmidt, K.; Ye, A. J.; Zojer, E.; Barlow, S.; Hagan, D. J.; Van Stryland, E. W.; Yi, Y. P.; Shuai, Z. G.; Pagani, G. A.; Bredas,

J. L.; Perry, J. W.; Marder, S. R., Extended squaraine dyes with large two-photon absorption cross-sections. *J. Am. Chem. Soc.* **2006,** *128* (45), 14444-14445.

58. Pond, S. J. K.; Rumi, M.; Levin, M. D.; Parker, T. C.; Beljonne, D.; Day, M. W.; Bredas, J. L.; Marder, S. R.; Perry, J. W., One- and two-photon spectroscopy of donor-acceptor-donor distyrylbenzene derivatives: Effect of cyano substitution and distortion from planarity. *J. Phys. Chem. A* **2002,** *106* (47), 11470-11480.

59. Rumi, M.; Ehrlich, J. E.; Heikal, A. A.; Perry, J. W.; Barlow, S.; Hu, Z. Y.; McCord-Maughon, D.; Parker, T. C.; Rockel, H.; Thayumanavan, S.; Marder, S. R.; Beljonne, D.; Bredas, J. L., Structure-property relationships for two-photon absorbing chromophores: Bis-donor diphenylpolyene and bis(styryl)benzene derivatives. *J. Am. Chem. Soc.* **2000,** *122* (39), 9500-9510.

60. Barbara, P. F.; Meyer, T. J.; Ratner, M. A., Contemporary issues in electron transfer research. *J. Phys. Chem.* **1996,** *100* (31), 13148-13168.

61. Wang, D.; Zhou, G. Y.; Ren, Y.; Xu, X. G.; Cheng, X. F.; Shao, Z. S.; Jiang, M. H., One- and two-photon absorption induced emission in HMASPS doped polymer. *Chem. Phys. Lett.* **2002,** *354* (5-6), 423-427.

62. Wu, C. F.; Szymanski, C.; Cain, Z.; McNeill, J., Conjugated polymer dots for multiphoton fluorescence imaging. *J. Am. Chem. Soc.* **2007,** *129* (43), 12904-+.

63. Yip, W. T.; Hu, D. H.; Yu, J.; Vanden Bout, D. A.; Barbara, P. F., Classifying the photophysical dynamics of single- and multiple-chromophoric molecules by single molecule spectroscopy. *J. Phys. Chem. A* **1998,** *102* (39), 7564-7575.

64. Blanton, S. A.; Dehestani, A.; Lin, P. C.; Guyotsionnest, P., Photoluminescence of single semiconductor nanocrystallites by 2-photon excitation microscopy *Chem. Phys. Lett.* **1994,** *229* (3), 317-322.

65. Dayal, S.; Burda, C., Semiconductor Quantum Dots as Two-Photon Sensitizers. *J. Am. Chem. Soc.* **2008,** *130*, 2890-2891.

66. van Oijen, A. M.; Verberk, R.; Durand, Y.; Schmidt, J.; van Lingen, J. N. J.; Bol, A. A.; Meijerink, A., Continuous-wave two-photon excitation of individual CdS nanocrystallites. *Applied Physics Letters* **2001,** *79* (6), 830-832.

67. Larson, D. R.; Zipfel, W. R.; Williams, R. M.; Clark, S. W.; Bruchez, M. P.; Wise, F. W.; Webb, W. W., Water-Soluble Quantum Dots for Multiphoton Fluorescence Imaging in Vivo. *Science* **2003,** *300*.

68. Clays, K.; Persoons, A., Hyper-Rayleigh scattering in solution. *Phys. Rev. Lett.* **1991,** *66* (23), 2980-2983.

69. Clays, K.; Persoons, A., Hyper-Rayleigh scattering in solution. *Rev. Sci. Instrum.* **1992,** *63* (6), 3285-3289.

70. Stadler, S.; Dietrich, R.; Bourhill, G.; Brauchle, C.; Pawlik, A.; Grahn, W., First hyperpolarizability measurements via hyper-Rayleigh scattering at 1500 nm. *Chem. Phys. Lett.* **1995,** *247* (3), 271-276.

71. Verbiest, T.; Clays, K.; Samyn, C.; Wolff, J.; Reinhoudt, D.; Persoons, A., Investigations of the hyperpolarizability in organic-molecules from dipolar to octopolar systems. *J. Am. Chem. Soc.* **1994,** *116* (20), 9320-9323.

72. Xu, C.; Shear, J. R.; Webb, W. W., Hyper-Rayleigh and hyper-Raman scattering background of liquid water in two-photon excited fluorescence detection. *Anal. Chem.* **1997,** *69* (7), 1285-1287.

73. Persoons, A.; Clays, K.; Kauranen, M.; Hendrickx, E.; Put, E.; Bijnens, W. In *Characterization of nonlinear-optical properties by hyper-scattering techniques* Elsevier Science Sa Lausanne: 1994; pp 31-38.

74. E.C. Hao, G. C. S., R.C. Johnson, and J.T. Hupp, Hyper-Rayleigh scattering from silver nanoparticles. *J. Chem. Phys.* **2002,** *117* (13), 5963-5966.

75. Johnson, R. C.; Li, J. T.; Hupp, J. T.; Schatz, G. C., Hyper-Rayleigh scattering studies of silver, copper, and platinum nanoparticle suspensions. *Chem. Phys. Lett.* **2002,** *356* (5-6), 534-540.

76. Kim, Y. J.; Johnson, R. C.; Li, J. G.; Hupp, J. T.; Schatz, G. C., Synthesis, linear extinction, and preliminary resonant hyper-Rayleigh scattering studies of gold-core/silver-shell nanoparticles: comparisons of theory and experiment. *Chem. Phys. Lett.* **2002,** *352* (5-6), 421-428.

77. Vance, F. W.; Lemon, B. I.; Hupp, J. T., Enormous hyper-Rayleigh scattering from nanocrystalline gold particle suspensions. *J. Phys. Chem. B* **1998,** *102* (50), 10091-10093.

78. Dadap, J. I.; Shan, J.; Eisenthal, K. B.; Heinz, T. F., Second-harmonic Rayleigh scattering from a sphere of centrosymmetric material. *Phys. Rev. Lett.* **1999,** *83* (20), 4045-4048.

79. Shan, J.; Dadap, J. I.; Stiopkin, I.; Reider, G. A.; Heinz, T. F., Experimental study of optical second-harmonic scattering from spherical nanoparticles. *Phys. Rev. A* **2006,** *73* (2), 4.

80. J. Nappa, I. R.-A., E. Benichou, C. Jonin, and P.F. Brevet, Wavelength Dependence of the Retardation Effects in Silver Nanoparticles Followed by Polarization Resolved Hyper Rayleigh Scattering. *Chem. Phys. Lett.* **2005,** *415*, 246-250.

81. I. Russier-Antoine, E. B., G. Bachelier, C. Jonin, and P.F. Brevet Multipolar Contributions of the Second Harmonic Generation from Silver and Gold Nanoparticles. *J. Phys. Chem. C* **2007,** *111*, 9044-9048.

82. Lo, K. Y.; Lue, J. T., Quantum-size effect on optical 2nd-harmonic generation in small metallic particles. *Phys. Rev. B* **1995,** *51* (4), 2467-2472.

83. Petty, J. T.; Zheng, J.; Hud, N. V.; Dickson, R. M., DNA-templated Ag nanocluster formation. *J. Am. Chem. Soc.* **2004,** *126* (16), 5207-5212.

84. Antoku, Y. Fluorescent Polycytosine-encapsulated Silver Nanoclusters. Georgia Institute of Technology, Atlanta, 2007.

85. Voet, D.; Voet, J. G.; Pratt, C. W., *Fundamentals of Biochemistry*. Second Edition ed.; John Wiley & Sons, Inc.: New York, 2002.

86. Hall, D. B.; Holmlin, R. E.; Barton, J. K., Oxidative DNA damage through long-range electron transfer. *Nature* **1996,** *382* (6593), 731-735.

87. Dandliker, P. J.; Holmlin, R. E.; Barton, J. K., Oxidative thymine dimer repair in the DNA helix. *Science* **1997,** *275* (5305), 1465-1468.

88. Li, X.; Bowen, K. H.; Haranczyk, M.; Bachorz, R. A.; Mazurkiewicz, K.; Rak, J.; Gutowski, M., Photoelectron spectroscopy of adiabatically bound valence anions of rare tautomers of the nucleic acid bases. *J. Chem. Phys.* **2007,** *127* (17), 6.

89. Stokes, S. T.; Li, X.; Grubisic, A.; Ko, Y. J.; Bowen, K. H., Intrinsic electrophilic properties of nucleosides: Photoelectron spectroscopy of their parent anions. *J. Chem. Phys.* **2007,** *127* (8), 6.

90. Schiedt, J.; Weinkauf, R.; Neumark, D. M.; Schlag, E. W., Anion spectroscopy of uracil, thymine and the amino-oxo and amino-hydroxy tautomers of cytosine and their water clusters. *Chem. Phys.* **1998,** *239* (1-3), 511-524.

91. Jordan, K. D.; Wang, F., Theory of dipole-bound anions. *Annu. Rev. Phys. Chem.* **2003,** *54*, 367-396.

92. Svozil, D.; Jungwirth, P.; Havlas, Z., Electron binding to nucleic acid bases. Experimental and theoretical studies. A review. *Collect. Czech. Chem. Commun.* **2004,** *69* (7), 1395-1428.

93. Trifonov, A.; Buchvarov, I.; Wagenknecht, H. A.; Fiebig, T., Real-time observation of hydrogen bond-assisted electron transfer to a DNA base. *Chem. Phys. Lett.* **2005,** *409* (4-6), 277-280.

94. Roat-Malone, R. M., *Bioinorganic Chemistry*. Wiley-IEEE: 2002.

95. Marzilli, L. G.; Kistenmacher, T. J.; Eichhorn, G. L., *Structural Principles of Metal Ion-Nucleotide and Metal Ion-Nucleic Acid Interactions*. John Wiley & Sons, Inc.: New York, 1980.

96. Marzilli, L. G.; Kistenmacher, T. J.; Rossi, M., Extension of role of O(2) of cytosine residues in binding of metal-ions - Synthesis and structure of an unusual polymeric silver(I) complex of 1-methylcytosine. *J. Am. Chem. Soc.* **1977,** *99* (8), 2797-2798.

97. Ratte, H. T., Bioaccumulation and toxicity of silver compounds: A review. *Environ. Toxicol. Chem.* **1999,** *18* (1), 89-108.

98. Morgan, I. J.; Henry, R. P.; Wood, C. M., The mechanism of acute silver nitrate toxicity in freshwater rainbow trout (Oncorhynchus mykiss) is inhibition of gill Na+ and Cl- transport. *Aquat. Toxicol.* **1997,** *38* (1-3), 145-163.

99. Humphreys, S. D. M.; Routledge, P. A., The toxicology of silver nitrate. *Adverse Drug React. Toxicol. Rev.* **1998,** *17* (2-3), 115-143.

100. Hidalgo, E.; Bartolome, R.; Barroso, C.; Moreno, A.; Dominguez, C., Silver nitrate: Antimicrobial activity related to cytotoxicity in cultured human fibroblasts. *Skin Pharmacol. Appl. Skin Physiol.* **1998,** *11* (3), 140-151.

101. Hussain, S.; Anner, R. M.; Anner, B. M., Cysteine protects Na,K-ATPase and isolated human-lymphocytes from silver toxicity. *Biochem. Biophys. Res. Commun.* **1992,** *189* (3), 1444-1449.

102. Lansdown, A. B. G., Critical observations on the neurotoxicity of silver. *Crit. Rev. Toxicol.* **2007,** *37* (3), 237-250.

103. Wang, Y.; Gong, X. G. In *First-principles study of neutral and charged silver clusters*, Springer: 2005; pp 19-22.

104. Wilchek, M.; Bayer, E. A., Avidin biotin technology 10 years on- has it lived up to its expectations. *Trends Biochem.Sci.* **1989,** *14* (10), 408-412.

105. Liu, W.; Howarth, M.; Greytak, A. B.; Zheng, Y.; Nocera, D. G.; Ting, A. Y.; Bawendi, M. G., Compact biocompatible quantum dots functionalized for cellular imaging. *J. Am. Chem. Soc.* **2008,** *130* (4), 1274-1284.

106. Breinbauer, R.; Kohn, M., Azide-alkyne coupling: A powerful reaction for bioconjugate chemistry. *Chembiochem* **2003,** *4* (11), 1147-1149.

107. Agrawal, S.; Christodoulou, C.; Gait, M. J., Efficient methods for attaching nonradioactive labels to the 5' ends of synthetic oligodeoxyribonucleotides. *Nucleic Acids Res.* **1986,** *14* (15), 6227-6245.

108. Reisfeld, A.; Rothenberg, J. M.; Bayer, E. A.; Wilchek, M., Nonradioactive hybridization probes prepared by the reaction of biotin hydrazide with DNA. *Biochem. Biophys. Res. Commun.* **1987,** *142* (2), 519-526.

109. Proudnikov, D.; Mirzabekov, A., Chemical methods of DNA and RNA fluorescent labeling. *Nucleic Acids Res.* **1996,** *24* (22), 4535-4542.

110. Michalet, X.; Pinaud, F. F.; Bentolila, L. A.; Tsay, J. M.; Doose, S.; Li, J. J.; Sundaresan, G.; Wu, A. M.; Gambhir, S. S.; Weiss, S., Quantum dots for live cells, in vivo imaging, and diagnostics. *Science* **2005,** *307* (5709), 538-544.

111. Michalet, X.; Pinaud, F.; Lacoste, T. D.; Dahan, M.; Bruchez, M. P.; Alivisatos, A. P.; Weiss, S. In *Properties of fluorescent semiconductor nanocrystals and their application to biological labeling*, Wiley-V C H Verlag Gmbh: 2001; pp 261-276.

112. Derfus, A. M.; Chan, W. C. W.; Bhatia, S. N., Probing the cytotoxicity of semiconductor quantum dots. *Nano Lett.* **2004,** *4* (1), 11-18.

113. Kirchner, C.; Liedl, T.; Kudera, S.; Pellegrino, T.; Javier, A. M.; Gaub, H. E.; Stolzle, S.; Fertig, N.; Parak, W. J., Cytotoxicity of colloidal CdSe and CdSe/ZnS nanoparticles. *Nano Lett.* **2005,** *5* (2), 331-338.

114. Groc, L.; Heine, M.; Cognet, L.; Brickley, K.; Stephenson, F. A.; Lounis, B.; Choquet, D., Differential activity-dependent regulation of the lateral mobilities of AMPA and NMDA receptors. *Nat. Neurosci.* **2004,** *7* (7), 695-696.

115. Idrobo, J. C.; Ogut, S.; Jellinek, J., Size dependence of the static polarizabilities and absorption spectra of Ag-n (n=2-8) clusters. *Phys. Rev. B* **2005,** *72* (8), 8.

116. Richards, C., unpublished results.

117. *Kodak Laser Dyes*.
Laboratory and Research Products Division, Eastman Kodak Co.
: , 1987.

118. Vogel, A. I.; Tatchell, A. R.; Furnis, B. S.; Hannaford, A. J.; Smith, P. W. G., *Vogel's Textbook of Practical Organic Chemistry*. 5th ed.; Prentice Hall: 1996.

119. Lakowicz, J. R., *Principles of Fluorescence Spectroscopy*. 3rd ed.; Springer: 2006.

120. Albota, M. A.; Xu, C.; Webb, W. W., Two-Photon Fluorescence Excitation Cross Sections of Biomolecular Probes from 690 to 960nm. *Appl. Opt.* **1998,** *37* (31).

121. Kuzyk, M. G., Fundamental limits on two-photon absorption cross sections. *J. Chem. Phys.* **2003,** *119* (16), 8327-8334.

122. Orr, B. J.; Ward, J. F., Perturbation theory of non-linear optical polarization of an isolated system. *Mol. Phys.* **1971,** *20* (3), 513-&.

123. Moreno, J. P.; Kuzyk, M. G., Fundamental limits of the dispersion of the two-photon absorption cross section. *J. Chem. Phys.* **2005,** *123* (19), 13.

124. Benesch, J.; Askendal, A.; Tengvall, P., The determination of thickness and surface mass density of mesothick immunoprecipitate layers by null ellipsometry and protein (125)iodine labeling. *J. Colloid Interface Sci.* **2002,** *249* (1), 84-90.

125. Tiggesbaumker, J.; Koller, L.; Lutz, H. O.; Meiwesbroer, K. H., Giant-resonances in silver-cluster photofragmentation. *Chem. Phys. Lett.* **1992,** *190* (1-2), 42-47.

126. Deheer, W. A., The physics of simple metal-clusters- experimental aspects and simple-models. *Rev. Mod. Phys.* **1993,** *65* (3), 611-676.

127. Widengren, J.; Mets, U.; Rigler, R., Fluorescence correlation spectroscopy of triplet-states in solution- a theoretical and experimental study. *J. Phys. Chem.* **1995,** *99* (36), 13368-13379.

128. Ringemann, C.; Schonle, A.; Giske, A.; von Middendorff, C.; Hell, S. W.; Eggeling, C., Enhancing fluorescence brightness: Effect of reverse intersystem crossing studied by fluorescence fluctuation spectroscopy. *ChemPhysChem* **2008,** *9* (4), 612-624.

129. Rigler, R.; Mets, U.; Widengren, J.; Kask, P., Fluorescence correlation spectroscopy with high count rate and low-background - analysis of translational diffusion. *Eur. Biophys. J. Biophys. Lett.* **1993,** *22* (3), 169-175.

130. Edward, J. T., Molecular volumes and stokes-einstein equation. *J. Chem. Educ.* **1970,** *47* (4), 261-&.

131. Magde, D.; Elson, E. L.; Webb, W. W., Fluorescence correlation spectroscopy .2. Experimental realization. *Biopolymers* **1974,** *13* (1), 29-61.

132. Bartko, A. P.; Dickson, R. M., Three-dimensional orientations of polymer-bound single molecules. *J. Phys. Chem. B* **1999,** *103* (16), 3053-3056.

133. Dickson, R. M.; Norris, D. J.; Moerner, W. E., Simultaneous imaging of individual molecules aligned both parallel and perpendicular to the optic axis. *Phys. Rev. Lett.* **1998,** *81* (24), 5322-5325.

134. Basche, T.; Moerner, W. E.; Orrit, M.; Talon, H., Photon antibunching in the fluorescence of a single dye molecule trapped in a solid. *Phys. Rev. Lett.* **1992,** *69* (10), 1516-1519.

135. Henglein, A.; Mulvaney, P.; Linnert, T., Chemistry of Agn aggregates in aqueous-solution-nonmetallic oligomeric clusters and metallic particles. *Faraday Discuss.* **1991**, 31-44.

136. Linnert, T.; Mulvaney, P.; Henglein, A.; Weller, H., Long-lived nonmetallic silver clusters in aqueous-solution- preparation and photolysis. *J. Am. Chem. Soc.* **1990,** *112* (12), 4657-4664.

137. Mulvaney, P.; Linnert, T.; Henglein, A., Surface-chemistry of colloidal silver in aqueous-solution - observations on chemisorption and reactivity. *J. Phys. Chem.* **1991,** *95* (20), 7843-7846.

138. Tauber, M. J.; Mathies, R. A., Fluorescence and resonance Raman spectra of the aqueous solvated electron. *J. Phys. Chem. A* **2001,** *105* (49), 10952-10960.

139. Widengren, J.; Schwille, P., Characterization of photoinduced isomerization and back-isomerization of the cyanine dye Cy5 by fluorescence correlation spectroscopy. *J. Phys. Chem. A* **2000,** *104* (27), 6416-6428.

140. Verberk, R.; van Oijen, A. M.; Orrit, M., Simple model for the power-law blinking of single semiconductor nanocrystals. *Phys. Rev. B* **2002,** *66* (23), 4.

141. Bates, M.; Blosser, T. R.; Zhuang, X. W., Short-range spectroscopic ruler based on a single-molecule optical switch. *Phys. Rev. Lett.* **2005,** *94* (10), 4.

142. Heilemann, M.; Margeat, E.; Kasper, R.; Sauer, M.; Tinnefeld, P., Carbocyanine dyes as efficient reversible single-molecule optical switch. *J. Am. Chem. Soc.* **2005,** *127* (11), 3801-3806.

143. Sugiyama, H.; Saito, I., Theoretical studies of GC-specific photocleavage of DNA via electron transfer: Significant lowering of ionization potential and 5'-localization of HOMO of stacked GG bases in B-form DNA. *J. Am. Chem. Soc.* **1996,** *118* (30), 7063-7068.

144. Carmichael, I.; Hug, G. L., Triplet-triplet Absorption Spectra of Organic Molecules in Condensed Phases. *J. Phys. Chem. Ref. Data* **1986,** *15* (1), 1-250.

145. Eggeling, C.; Widengren, J.; Rigler, R.; Seidel, C. A. M., Photobleaching of fluorescent dyes under conditions used for single-molecule detection: Evidence of two-step photolysis. *Anal. Chem.* **1998,** *70* (13), 2651-2659.

146. Widengren, J.; Mets, U.; Rigler, R., FLUORESCENCE CORRELATION SPECTROSCOPY OF TRIPLET-STATES IN SOLUTION - A THEORETICAL AND EXPERIMENTAL-STUDY. *J. Phys. Chem.* **1995,** *99* (36), 13368-13379.

147. Trnkova, L.; Jelen, F.; Postbieglova, I., Application of elimination voltammetry to the resolution of adenine and cytosine signals in oligonucleotides. I. Homooligodeoxynucleotides dA(9) and dC(9). *Electroanalysis* **2003,** *15* (19), 1529-1535.

148. Zahavy, E.; Fox, M. A., Photophysical quenching mediated by guanine groups in pyrenyl-N-alkylbutanoamide end-labeled oligonucleotides. *J. Phys. Chem. B* **1999,** *103* (43), 9321-9327.

149. Murphy, C. J.; Arkin, M. R.; Jenkins, Y.; Ghatlia, N. D.; Bossmann, S. H.; Turro, N. J.; Barton, J. K., Long-range photoinduced electron-transfer through a DNA helix. *Science* **1993,** *262* (5136), 1025-1029.

150. Chen, P. Y.; Duesing, R.; Graff, D. K.; Meyer, T. J., Intramolecular electron-transfer in the inverted region. *J. Phys. Chem.* **1991,** *95* (15), 5850-5858.

151. Ohkubo, K.; Kotani, H.; Shao, J. G.; Ou, Z. P.; Kadish, K. M.; Li, G. L.; Pandey, R. K.; Fujitsuka, M.; Ito, O.; Imahori, H.; Fukuzumi, S., Production of an ultra-long-lived charge-separated state in a zinc chlorin-C-60 dyad by one-step photoinduced electron transfer. *Angew. Chem.-Int. Edit.* **2004,** *43* (7), 853-856.

152. Liang, N.; Miller, J. R.; Closs, G. L., Temperature-independent long-range elecgtron-transfer reactions in the Marcus inverted region. *J. Am. Chem. Soc.* **1990,** *112* (13), 5353-5354.

153. Suppan, P., The Marcus inverted region. *Top. Curr. Chem.* **1992,** *163*, 95-130.

154. Tutt, L. W.; Kost, A., Optical limiting performance of C-60 and C-70 solutions. *Nature* **1992,** *356* (6366), 225-226.

155. Tutt, L. W.; Boggess, T. F., A review of optical limiting mechanisms and devices using organics, fullerenes, semiconductors and other materials. *Prog. Quantum Electron.* **1993,** *17* (4), 299-338.

156. Perry, J. W.; Mansour, K.; Lee, I. Y. S.; Wu, X. L.; Bedworth, P. V.; Chen, C. T.; Ng, D.; Marder, S. R.; Miles, P.; Wada, T.; Tian, M.; Sasabe, H., Organic optical limiter with a strong nonlinear absorptive response. *Science* **1996,** *273* (5281), 1533-1536.

157. Hernandez, F. E.; Yang, S.; Van Stryland, E. W.; Hagan, D. J., High-dynamic-range cascaded-focus optical limiter. *Opt. Lett.* **2000,** *25* (16), 1180-1182.

158. Sun, X.; Xiong, Y. N.; Chen, P.; Lin, J. Y.; Ji, W.; Lim, J. H.; Yang, S. S.; Hagan, D. J.; Van Stryland, E. W., Investigation of an optical limiting mechanism in multiwalled carbon nanotubes. *Appl. Optics* **2000,** *39* (12), 1998-2001.

159. Lepkowicz, R.; Kobyakov, A.; Hagan, D. J.; Van Stryland, E. W., Picosecond optical limiting in reverse saturable absorbers: a theoretical and experimental study. *J. Opt. Soc. Am. B-Opt. Phys.* **2002,** *19* (1), 94-101.

160. Fleischm.M; Hendra, P. J.; McQuilla.Aj, Raman-spectra of pyridine adsorbed at a silver electrode. *Chem. Phys. Lett.* **1974,** *26* (2), 163-166.

161. Fleischm.M; Hendra, P. J.; McQuilla.Aj, Raman-spectra from electrode surfaces. *J. Chem. Soc.-Chem. Commun.* **1973,** (3), 80-81.

162. Kneipp, K.; Wang, Y.; Kneipp, H.; Perelman, L. T.; Itzkan, I.; Dasari, R.; Feld, M. S., Single molecule detection using surface-enhanced Raman scattering (SERS). *Phys. Rev. Lett.* **1997,** *78* (9), 1667-1670.

163. Peyser-Capadona, L.; Zheng, J.; Gonzalez, J. I.; Lee, T. H.; Patel, S. A.; Dickson, R. M., Nanoparticle-free single molecule anti-stokes Raman spectroscopy. *Phys. Rev. Lett.* **2005,** *94* (5), 4.

164. Capadona, L. Photoactivated Fluorescence of Small Silver Nanoclustes and their Relation to Raman Spectroscopy. Georgia Institute of Technology, Atlanta, 2004.

165. Jacobsohn, M.; Banin, U., Size dependence of second harmonic generation in CdSe nanocrystal quantum dots. *J. Phys. Chem. B* **2000,** *104* (1), 1-5.

166. Jin, R. C.; Jureller, J. E.; Kim, H. Y.; Scherer, N. F., Correlating second harmonic optical responses of single Ag nanoparticles with morphology. *J. Am. Chem. Soc.* **2005,** *127* (36), 12482-12483.

167. Aktsipetrov, O. A.; Elyutin, P. V.; Nikulin, A. A.; Ostrovskaya, E. A., Size effects in optical 2nd-harmonic generation by metallic nanocrystals and semiconductor quantum dots- the role of quantum chaotic dynamics. *Phys. Rev. B* **1995,** *51* (24), 17591-17599.

168. Beeby, A.; Botchway, S. W.; Clarkson, I. M.; Faulkner, S.; Parker, A. W.; Parker, D.; Williams, J. A. G., Luminescence imaging microscopy and lifetime mapping using kinetically stable lanthanide(III) complexes. *J. Photochem. Photobiol. B-Biol.* **2000,** *57* (2-3), 83-89.

169. Connally, R.; Veal, D.; Piper, J., Flash lamp-excited time-resolved fluorescence microscope suppresses autofluorescence in water concentrates to deliver an 11-fold increase in signal-to-noise ratio. *J. Biomed. Opt.* **2004,** *9* (4), 725-734.

170. Bunzli, J. C. G., Benefiting from the unique properties of lanthanide ions. *Accounts Chem. Res.* **2006,** *39* (1), 53-61.